ABSTRACT

Title of Dissertation: EXCITED DYONIC STATES OF MONOPOLES AND ASTRONOMICAL BOUNDS ON AN AXION-PHOTON-DARK PHOTON INTERACTION

Clayton Ristow
Doctor of Philosophy, 2024

Dissertation Directed by: Associate Professor Anson Hook
Department of Physics

The study of beyond the standard model physics can largely be broken into two categories: theoretical and phenomenological. In the former, we study theories in depth to better understand their implications while in the latter, we hold models of our physical world to scrutiny against experimental evidence. Both are crucial to understanding physics beyond the standard model. To reflect this dichotomy, this thesis is broken into two acts, one covering theoretic research and the other discussing progress made on the phenomenological front.

Chapter 2, comprising the entirety of Act 1 of this thesis, concerns the theory of magnetic monopoles. In the mid-1970's t'Hooft and Polyakov discovered magnetic monopoles exist as generic solutions in spontaneously broken gauge theories. Since then much progress has been made in understanding these monopoles, most notably by Callan who argued that the fermion vacuum is non-trivial around the core of the magnetic monopole. These non-trivial vacuua can be interpreted as bound states of fermions with fractional fermion number. In this work, we explicitly compute these fermion bound states in an $SU(2)$ gauge theory coupled to N_f fermions. We demonstrate there are two unique ways to grant mass to the fermions in the $SU(2)$ theory which, after symmetry breaking, give the same $U_{EM}(1)$ theory of fermions. Despite this low energy equivalence, we show that the two theories exhibit very different physics at low energy

scales around a magnetic monopole. We show that there may exist stable excited dyonic states with differing charges and energies between the two theories. We find the ground states can also differ in energy and charge between the two theories. We demonstrate the monopole can inherit a mass correction and charge distribution that depends on the topological θ angle even if one of the fermions is massless. This effect is present in one of the theories and is completely absent in the other. Finally, we discuss the implications of these effects on the $SU(5)$ GUT monopole.

Act two, comprising of chapters 3 and 4, focuses on the phenomoenological side of beyond the standard model physics. In these chapters, we consider two highly motivated beyond the standard model particles, the axion, ϕ, and the dark photon A_D which are coupled to the standard model photon via a coupling $\phi F \tilde{F}_D$. In some models, this coupling can provide the leading order coupling between our sector and the dark sector containing the axion and dark photon.

In chapter 2, we demonstrate the effect this coupling has on the Cosmic Microwave Background (CMB) in the scenario where either the axion or the dark photon constitutes dark matter. Depending on which we choose to be dark matter, we show that this interaction leads to the conversion of the CMB photons into the other dark sector particle, leading to a distortion in the CMB spectrum. We present the details of these unique distortion signatures and the resulting constraints on the $\phi F \tilde{F}_D$ coupling. In particular, we find that for a wide range of masses, the constraints from this effect are stronger than on the more widely studied axion-photon-photon coupling. We also demonstrate that CMB distortions of this type can a exhibit unique, non-thermal frequency profile which could be detected by future experiments.

In chapter 3, we consider the astrophysical effects of the $\phi F \tilde{F}_D$ coupling, in particular, its effect on supernova cooling rates. We show that the bound on this interaction due to supernova cooling exhibits two unusual features. If there is a large mass difference between the axion and dark photon, we show both production and scattering become suppressed and the bounds from bulk (volume) emission and trapped (area) emission both weaken exponentially. We show that these bounds do not intersect leading to a larger area of excluded parameter space than may have otherwise been expected. The other unusual feature occurs because the longitudinal modes

of light dark photons couple more weakly than their transverse modes. As a consequence, the longitudinal modes can still cause excessive cooling even if the transverse modes are trapped. Thus, the supernova constraints for massive dark photons look like two independent supernova bounds super-imposed on top of each other. We also briefly consider the effect of this interaction on white dwarf cooling and Big Bang Nucleosynthesis.

EXCITED DYONIC STATES OF MONOPOLES AND ASTRONOMICAL BOUNDS ON AN AXION-PHOTON-DARK PHOTON INTERACTION

by

Clayton James Ristow

Dissertation submitted to the Faculty of the Graduate School of the
University of Maryland, College Park in partial fulfillment
of the requirements for the degree of
Doctor of Philosophy
2024

Dissertation Committee:

Associate Professor Anson Hook, Chair/Advisor
Professor Zackaria Chacko
Professor Kaustubh Agashe
Professor Thomas Cohen
Professor Richard Wentworth, Dean's Representative

© Copyright by
Clayton Ristow
2024

Preface

My decision to pursue a PhD in physics came from pure intentions; to learn more physics. Specifically, I wanted to learn as much as I could about the fundamental laws of our universe and what possible undiscovered laws could be uncovered in the future.

The thesis that follows serves as a testament to my success in this endeavor. It is the culmination of five years of research into the field of theoretical particle physics. The landscape of particle physics is vast, and as such, I made it a point to pick brand new topics for each new project to absorb as much of the field as possible.

This thesis is a sampling of the most personally significant of these projects. Presented in reverse chronological order, they capture my growth from physics student to physicist. Chapter 4 documents my first foray in world of particle physics, Chapter 3 displays growth and confidence in my abilities, and Chapter 2 shows my most recent and challenging work to date. Completing these projects and compiling my thoughts and results into this thesis is the proudest achievement of my career thus far.

As such I would like to thank you, the reader, for taking the time to visit my thesis. Whether you read through all 169 pages (a square number!) or are passing through to reference an equation, you have taken the time to view this snapshot of my life, for which I am grateful. So please read on and as I did, enjoy.

Clayton Ristow,

College Park, July, 2024

Dedication

To my younger self who wanted to learn physics to figure out “how particles work”.

Now we know.

Acknowledgments

There is no doubt I would not have been able to complete this work without the assistance of many people along the way. First and foremost, I would like to thank my advisor and committee chair, Professor Anson Hook. Your seemingly endless depth of knowledge ensured none of my questions went unanswered and your enthusiasm for the field kept me inspired throughout my time as your student. I'd like to thank the rest of the committee who were generous to provide their time and expertise in reviewing this thesis. I would also like to thank the National Science Foundation and the Maryland Center for Fundamental Physics for their support of this work.

I would also like to thank those I have collaborated with over the past five years, without whom none of the work I've completed would have been possible: Dawid Brzeminski, Dr. Saurav Das, Dr. Junwu Huang, and Professor Gustavo Marques-Tavares. An additional thanks goes out to the many physicists I have had the pleasure of meeting and absorbing knowledge from, particularly those who had a direct and tangible impact on this work such as Professor Ken Van Tilburg, Dr. Asimina Arvanitaki, and Professor Raman Sundrum.

Finally, I would like to thank my family. Thank you to my mother, Julie, for always encouraging me to do my best and instilling me with confidence. Thank you to my father, Randy, for being a source of inspiration and nurturing me as a young mathematician. And thank you to Megan for supporting me in every possible way for the past five years. I couldn't have done it without you all.

Table of Contents

Chapter 1: Introduction

As one of the most well-tested scientific theories, the Standard Model of particle physics currently provides the most accurate description of our universe. While it has withstood many precision tests and been successfully applied at scales ranging from cosmological to the subatomic, there are areas where the Standard Model fails to give a sufficient description of reality. These failures of the Standard Model are key indicators of directions in which to search for new theories of physics beyond the standard model (BSM). Research in BSM physics can largely be broken into two categories: theoretic and phenomenological. Theoretic, in this context, encompasses all research in which a specific model is taken and studied in detail outside of its real-world applicability while phenomenology deals explicitly with holding existing theories to scrutiny against experimental data. Both are equally important areas of study and historically interplay with one another. For example, research into the theory of General Relativity led to the prediction of gravitational waves, which now constitute a large sector of phenomenological research. Conversely, phenomenological research into the nature of dark matter has led theorists to devise and study many models for its particle constituency. Due to the equal importance of these two lines of research, this thesis is divided into two acts with Act 1 focusing on research in theory and Act 2 focusing on phenomenology.

Act 1, consisting of Chapter 2, concerns research into the theory of magnetic monopoles.

Magnetic Monopoles have been an intriguing prospect for physics ever since the discovery of Maxwell's equations. Most undergraduate physics students would be able to appreciate how symmetric Maxwell's Equations become after the addition of magnetic charges and currents.

$$\begin{aligned} \boldsymbol{\nabla} \cdot \boldsymbol{E} &= \rho_e & & & \boldsymbol{\nabla} \cdot \boldsymbol{E} &= \rho_e \\ \boldsymbol{\nabla} \cdot \boldsymbol{B} &= 0 & \longmapsto & & \boldsymbol{\nabla} \cdot \boldsymbol{B} &= \rho_m \\ \partial_t \boldsymbol{E} - \boldsymbol{\nabla} \times \boldsymbol{B} &= -J_e & & & \partial_t \boldsymbol{E} - \boldsymbol{\nabla} \times \boldsymbol{B} &= -J_e \\ \partial_t \boldsymbol{B} + \boldsymbol{\nabla} \times \boldsymbol{E} &= 0 & & & \partial_t \boldsymbol{B} + \boldsymbol{\nabla} \times \boldsymbol{E} &= -J_m \end{aligned} \tag{1.1}$$

However, symmetric beauty alone is not enough to suggest a theory represents physical reality. This changed when, in 1931, Dirac proved that the existence of magnetic monopoles implied charge quantization [1]. A simple calculation shows that a monopole with magnetic charge g and an electric monopole of charge e in the same universe have angular momentum stored in their combined electric and magnetic fields equal to

$$\boldsymbol{L} = \frac{eg}{4\pi} \hat{\boldsymbol{r}} \tag{1.2}$$

where $\hat{\boldsymbol{r}}$ is a unit vector pointing from the electric to the magnetic charge. Quantum mechanics dictates that angular momentum in all forms comes in integer multiples of $1/2$ (In this thesis, we work in natural units where $\hbar = c = 1$). This immediately implies all allowable charges in the same universe as a magnetic monopole have quantized charges coming in integer multiples of $e_{min} = \frac{2\pi}{g}$.

While Dirac provided the first bit of theoretical motivation to consider magnetic monopoles,

it wasn't until it was found by 't Hooftand Polyakov that monopoles exist naturally as stable soliton states in many spontaneously broken gauge theories [2,3]. The so-called 't Hooft-Polyakov monopole was found to be a rich area for theoretical research. These monopoles bring with them an infinite landscape of electrically and magnetically charged objects, called dyons, with electric charges Q_E and magnetic charges Q_M that are integer multiples of the fundamental of the fundamental electric and magnetic charges e and $2\pi/e$ respectively. Witten discovered that adding a topological theta term $\sim \theta F\tilde{F}$ to the Lagrangian lowers the electric charge of all dyons to a nonintegral value of $Q_E - \theta/2\pi$. This phenomoenon has come to be known as the Witten effect [4]. Originally, these dyonic excitations were found by quantizing the charge rotator degree of freedom of the 't Hooft-Polyakov monopole but dyons are often colloquially interpreted as charged W bosons bound to the monopole [1].

The story of monopoles becomes even richer when one considers adding fermions into the mix. Fermions, via the chiral anomaly, can carry the topological charge, $-\theta/2\pi$, from the Witten effect and it is energetically favorable to excite the light, charged fermions as opposed to the charge rotator/W boson [5, 6]. This suggests that in the presence of light fermions, the electric charge of Dyons is carried by the fermion field and the Dyon can be interpreted as a bound state of fermions around the monopole with fractional fermion number. These fermion bound states have a binding energy of order the mass of the fermions and radii of order inverse the fermion masses. As we will demonstrate in Chapter 2, the structure of these bound states will depend heavily on the UV theory from which the monopole derive. This is just one manifestation of the Callan-Rubakov effect [5, 7–10], which is the statement that the low energy physics around

[1]The interpretation of the dyon as a bound state of the monopole and a W boson is not precise, as the dyon carries one more topological charge than the monopole. For example, if one added a charged scalar lighter than the W to the theory, the dyon does not decay despite the fact that the W boson would decay.

a magnetic monopole can depend heavily on the high energy physics underlying the monopole. The Callan-Rubakov Effect continues to be an active area of research to this day [11,12] to which this chapter contributes.

Chapter 2 is dedicated to studying these fermionic bound states in $SU(2)$ gauge theory with N_f fermions. In section 2.1 we will present the Ultraviolet (UV) theory and show that there are two types of mass terms with which to give mass to the fermions. These two types of mass terms break the $SU(N_f)$ flavor symmetry into either an $SO(N_f)$ or a $Sp(N_f)$ flavor symmetry. In section 2.2, we consider both of these theories of fermions in a 't Hooftmonopole background and show that $J = 0$ subspace of states reduces the theory to a 1+1D theory of fermions on the half plane and that the $SO(N_f)$ and $Sp(N_f)$ theories are identical up to boundary conditions. We then employ bosonization techniques in section 2.3 to write this as a theory of N_f scalar fields in 1+1D. We use this bosonized theory to compute the aforementioned bound states. In section 2.4, we use a $N_f = 1$ toy model to familiarize ourselves and the reader with this bosonized model before moving on to a detailed analysis of both theories for $N_f = 2$ in section 2.5. In section 2.6 we examine $N_f \geq 4$ theories. We highlight unique phenomena such as the dependence of the mass and the charge density distribution of the fermion bound state on the θ angle even if one of the fermions is massless. Finally, we comment on the implications this research has for monopoles in the standard model under grand unification in section 2.7.

Act 2 of this thesis, consisting of Chapters 3 and 4, focuses on the phenomenology of a dark sector consisting of a scalar particle ϕ, called an axion, and a vector particle, A^μ_D, called the dark photon which couple to the standard model photon via a coupling of the form

$$\mathcal{L} \supset \frac{\phi}{2f_a} F^D_{\mu\nu} \tilde{F}^{\mu\nu} \quad \text{where} \quad \tilde{F}^{\mu\nu} = \frac{1}{2}\epsilon^{\mu\nu\alpha\beta} F_{\alpha\beta} \, . \tag{1.3}$$

Where $F(F_D)$ is the photon (dark photon) field strength tensor. Generically, in models with axions and dark photons, one expects interactions of the form $\phi F\tilde{F}$ and kinetic mixing between the photon and dark photon ($\epsilon F F_D$) to be present and just as, if not more relevant than the coupling given in Eq. 1.3. However, if one demands that there is a dark charge conjugation symmetry C_D under which the axion and dark photon are odd, these other couplings are absent, or at the very least if there is a small breaking of the symmetry, highly suppressed. In appendix B.1, we present a simple model that exhibits such a symmetry and show that the coupling given in Eq. 1.3 is the leading one. This coupling has been studied in a variety of scenarios [13–24]. Additional motivation for studying this coupling comes from dark photon dark matter. Dark photons are a compelling dark matter candidate and so production mechanisms for it are interesting. Above a keV, dark photon dark matter can be produced thermally, either through freeze-out or freeze-in. As it becomes lighter than keV, one needs to consider non-thermal production mechanisms [25–30]. Dark photon production from axions using the coupling in Eq. 1.3 is one of the few ways to realize dark photon dark matter lighter than a μeV [31]

In the grand scheme of modern BSM physics, the axion and dark photon are two of the most motivated candidates for physics beyond the standard model. Extra dimensional theories, such as string theory, typically predict a plethora of light scalars and vectors [32–35]. Already the pioneering work on extra dimensional models by Kaluza and Klein proposed that the electromagnetic gauge symmetry, and thus the photon, could be a consequence of extra-dimensions [36, 37]. Even without such motivations coming from extra dimensional constructions, both the axion and dark photon are highly motivated candidates for ultralight bosonic dark matter [38–43], and, in addition, the axion provides an elegant solution to the strong CP problem [44–47]. There are many instances of dark matter consisting of ultralight dark photons produced non-

thermally [25–30]. One such method for non-thermal production of dark photons is from axions via the coupling in Eq. 1.3 [31], providing extra motivation to carefully consider this interaction.

In Chapter 3, we investigate how this coupling affects the Cosmic Microwave Background (CMB) when either the axion or the dark photon is dark matter. In the early universe, before redshifts of $z \sim 1100$, the universe was hot and dense enough that photons, electrons, and protons were all in thermal equilibrium. Once the universe cooled to redshift $z = 1100$, effectively all electrons were bound to nuclei forming neutral atoms, making the universe transparent to photons, in an era called recombination. As the number of free electrons decreased with the lowering temperature, the mean free path of photons λ_γ increased. Around the time of recombination ($z \approx 1100$), $\lambda_\gamma \sim H$ and the photons transitioned from being trapped in the electron-baryon plasma to being free streaming. Afterward, these photons could propagate freely until being detected by CMB experiments. Due to the early thermal equilibrium of these photons, their power spectrum follows that of a blackbody. In the early 1990's, the Cosmic Background Explorer (COBE) [48] satellite equipped with Far Infrared Absolute Spectrophotometer (FIRAS) performed the most accurate measurement of the CMB monopole power spectrum. They found it matched a blackbody with a temperature 2.7255 K to agree to about 1 part in 1,000 to 10,000 [49], making the CMB monopole power spectrum one of the most precisely measured cosmological observables. Any phenomena that would distort this spectrum are then highly constrained by COBE-FIRAS. Constraints on kinetic mixing [50] and dark matter interactions [51–56] from the COBE-FIRAS data have been placed using these spectral distortions[2].

The interaction given in Eq 1.3 can cause CMB spectral distortions. In the presence of an axion dark matter background, this interaction allows photons to be converted into dark

[2]Constrains on interactions can also be placed using CMB anisotropies as was done for kinetic mixing in [57]

photons. Likewise, in a dark photon dark matter background, it allows photons to be converted to axions (see Ref. [22] for an early study of this effect in the resonant regime). These dark sector particles are invisible to us and thus the effect of Eq. 1.3 in both cases is to remove photons from the CMB spectrum. This removal of photons naturally distorts the observed CMB spectrum. In section 3.1, we will show how the time at which these photons are removed gives rise to different types of distortions and argue that the size of these distortions depends on the probability of removing a photon from the spectrum. In section 3.2, we will compute this probability from the interaction in Eq. 1.3 and in section 3.3 use it to compute the various types of distortions. In section 3.4 we place constraints on the coupling $1/f_a$ by comparing these distortions to the COBE-FIRAS data and briefly comment on the possible shapes of the distortions.

In chapter 4, we explore astrophysical constraints on this coupling. In the late 1980's, the detection of neutrinos from the supernova SN1987A [58–60] confirmed the theoretical picture that the proto-neutron stars formed during core collapse supernova cool via neutrino emission. BSM particles could, in theory, accelerate this cooling rate by providing an extra channel through which the supernova can lose energy. Bounds on new physics can be placed by demanding that any novel cooling mechanism is subdominant to neutrino cooling [61–63]. Weakly coupled particles can escape the core without interacting once they are produced, which results in a constraint on the emission of these particles in the bulk. For larger couplings, the BSM particles become trapped and the cooling is carried out by particles emitted at the last scattering surface, resulting in a blackbody-like emission of BSM particles. The trapping regime leads to an upper bound on the couplings that can be constrained by cooling while bulk emission leads to a lower bound. Generically, the lower bound curve from bulk emission and the upper bound curve from surface emission in the mass vs coupling plane intersect at large masses, leading to a closed

region that can be excluded by cooling considerations.

Since SN1987A, cooling arguments have been used to constrain axions [64–67], CP even scalars [68], dark photons [69–71], dark sectors [72–74], sterile neutrinos [75], extra dimensions [76], and supersymmetry [77]. In the process of deriving these bounds, it was slowly realized that many important effects and features were not initially properly accounted for. For example, finite density effects drastically changed the qualitative features of supernovae bounds [78, 79]. We will continue this trend by pointing out two new features present in supernova bounds.

We study the supernovae cooling constraint on the axion-photon-dark-photon coupling in Eq. 1.3, and show that this model leads to two new qualitative features in supernovae that can play a role in non-minimal scenarios where there are more than one new degrees of freedom. The first feature we discuss is that different polarizations of particles can have different interaction strengths, and thus their production, and in particular their trapping, needs to be treated separately rather than averaged over[3]. For example, the longitudinal mode couples more weakly than the transverse mode and therefore receives its own cooling and trapping constraints. The second feature arises when the new particles must be pair produced and the two species have different masses. For fixed coupling, as the mass of one particle becomes larger, their joint production is suppressed because the threshold energy for pair production is increased. However, because the same interaction vertex appears in scattering processes, the scattering of the lighter particle becomes suppressed as well, as it does not have enough energy to up-scatter into the heavier particle. As a result, both production and scattering become suppressed so that the associated bounds both become weaker exponentially, and the trapping limit and bulk emission limit curves

[3]The fact that the production rate of transverse and longitudinal modes have to be treated separately has long been recognized by many previous references. Here we are emphasizing the importance of treating distinct polarizations differently in the trapping regime as well.

do not intersect.

In section 4.1, we review how core-collapse supernovae can be used to place constraints on new physics and derive the cooling constraints on our model. In section 4.2, we derive the trapping constraints. We discuss in detail the longitudinal mode of the dark photon and its constraints in section 4.3. Additional non-supernova astrophysical constraints are discussed in section 4.4.

Chapter 2: Stable Dyonic States of Magnetic Monopoles

2.1 UV and IR Theories

We begin our discussion of exited monopole states by first describing the theories of interest in both the Ultraviolet (UV) and Infrared (IR) regimes. In the UV, we are interested in $SU(2)$ gauge theories coupled to N_f fundamentally charged left-handed Weyl fermions, χ and an adjoint scalar Φ the Lagrangian for which is shown in Eq. 2.1.

$$\mathcal{L} = -\frac{1}{4}F^a_{\mu\nu}F_a^{\mu\nu} + \frac{\theta e^2}{32\pi^2}F^a_{\mu\nu}\tilde{F}_a^{\mu\nu} + i\chi^\dagger\bar{\sigma}^\mu D_\mu\chi + \frac{1}{2}D_\mu\Phi D^\mu\Phi - V(|\Phi|) \tag{2.1}$$

We will show that in the UV we can include Yukawa/mass terms for the fermions that break the $SU(N_f)$ flavor symmetry into either $SO(N_f)$ or $Sp(N_f)$. We then show that the two theories are identical in the IR and examine the $N_f = 2$ case more concretely.

2.1.1 UV Theories

We start with an $SU(2)$ gauge theory of N_f left-handed Weyl fermions represented by the multiplet χ and a scalar Higgs Φ in the adjoint representation. This theory enjoys a $SU(N_f)$ flavor symmetry. The Higgs field Φ has a potential $V(|\Phi|)$ which is responsible for breaking the $SU(2)$ gauge symmetry into a $U(1)_{EM}$ electromagnetic symmetry. From here we can give mass

	$SU(2)_{Gauge}$	$SU(N_f)$
χ	$\square$	$\square$
Φ	adj.	0

Table 2.1: The charges in our UV Theory.

to the fermions through two types of mass terms. The first type of mass term is of the form

$$-\delta\mathcal{L}_{SO(N_f)} = \frac{iy}{2}\Phi_b^a\epsilon_{bc}\chi_i^a\chi_i^c + h.c. \tag{2.2}$$

where i is the flavor index and a, b, c are the gauge indices. These mass terms break the $SU(N_f)$ flavor symmetry down to an $SO(N_f)$ flavor symmetry. After symmetry breaking, this mass term can be written in the form of a Dirac mass term as,

$$-\delta\mathcal{L}_{SO(N_f)} = m\bar{\psi}_i\psi_i, \quad \text{where} \quad \psi_i = \begin{pmatrix} \chi_{i,+} \\ -\sigma_2\chi_{i,-}^* \end{pmatrix} \tag{2.3}$$

where $\chi_{i,\pm}$ are the $SU(2)$ isospin eigenstates of χ. Eventually, we will wish to allow one of the masses to be different from the others. We can do this by allowing different flavors to have different Yukawa couplings ($y \to y_i$). IN the case where one of the masses is changed, this further breaks the flavor symmetry down to $SO(N_f - 1)$.

The second type of mass term can be written by breaking the $\chi's$ into two families; $\chi_{A,i}$ and $\chi_{B,i}$ where $i = 1, 2, ..., N_f/2$. Note that N_f is required to be even by the Witten anomaly [80]. We then write

$$-\delta\mathcal{L}_{Sp(N_f)} = m\epsilon_{ab}\chi_{A,i}^a\chi_{B,i}^b + h.c. \tag{2.4}$$

where, a and c are gauge indices. A mass term of this form breaks the $SU(N_f)$ flavor symmetry

down to $Sp(N_f)$. After symmetry breaking, this mass term can also be written as the sum of Dirac mass terms

$$-\delta\mathcal{L}_{Sp(N_f)} = m\bar{\psi}_{b,i}\psi_{b,i} + m\bar{\psi}_{\ell,i}\psi_{\ell,i} \tag{2.5}$$

if we define

$$\psi_{b,i} = \begin{pmatrix} \chi_{A,i,+} \\ i\sigma_2\chi^*_{B,i,-} \end{pmatrix} \quad \text{and} \quad \psi_{\ell,i} = \begin{pmatrix} \chi_{B,i,+} \\ -i\sigma_2\chi^*_{A,i,-} \end{pmatrix}. \tag{2.6}$$

We can allow for different masses by including an additional term in the mass term as follows,

$$-\delta\mathcal{L}_{Sp(N_f)} = \chi^a_{A,i}\chi^c_{B,i}(m\delta_{ab} + y\Phi_{ab})\epsilon_{bc} + h.c. \tag{2.7}$$

Which will give $\psi_{b,i}$ and $\psi_{\ell,i}$ masses of $m + yv$ and $m - yv$ respectively. If we include this in one of the mass pairs, the flavor symmetry is broken down to $U(1) \times Sp(N_f - 2)$.

It is worth noting that one could also consider a combination of these two mass term types for different flavors resulting in a flavor symmetry of $SO(N_f - n) \times Sp(n)$. We will not discuss this prospect further but it is easy to see from the following sections how to generalize our analysis to these types of theories.

2.1.2 IR Theory

From Eq. 2.2- 2.4 we see that the IR theory for both types of mass terms ends up the same: QED with N_f positively charged, equal mass fermions. The Lagrangian for both has the form

$$\mathcal{L} = i\bar{\psi}_i\not{\partial}\psi_i + m\bar{\psi}_i\psi_i + A_\mu j^\mu_{EM} + (\text{Pure Gauge}) \quad \text{where} \quad j^\mu_{EM} = \bar{\psi}_i\bar{\gamma}^\mu\psi_i. \tag{2.8}$$

Naively, in the IR, one would be led to believe that this theory has a full $SU(N_f)$ flavor symmetry. However, the above analysis shows that, if one is to embed this theory into an $SU(2)$ gauge theory in the UV, this $SU(N_f)$ flavor symmetry must be broken (except for the unique case of $N_f = 2$ where $Sp(2) \cong SU(2)$).

2.2 Fermions around a Monopole

To compute the dyonic bound states of fermions around a monopole, we will need a framework in which to study and compute the fermion fields. In this section, we will describe the process of computing fermion fields in a 't Hooft-Polyakov monopole background. We follow the a standard procedure [5,8] by first reducing the full 1+3D theory of fermions to a 1+1D theory of fermions by considering only the total angular momentum $\boldsymbol{J} = 0$ mode of the fermions which interacts with the monopoles core. Then we make use of a duality between fermions and bosons in 1+1D theories to rewrite our theory of N_f fermions as a theory of N_f scalars through a process called bosonization. These scalar fields are then used to compute the fermion states in subsequent sections

2.2.1 Gauge Sector and the Monopole Background

The 't Hooft-Polyakov background is described by the following background gauge field, A^a_μ, and scalar field, Φ^a.

$$A^a_0 = \frac{i}{e}U(\lambda)\partial_0 U^\dagger(\lambda) = \dot{\lambda}(t,r)\hat{r}_a\tau_a/2 \quad A^a_i = \epsilon_{\mu ab}\hat{r}^b\frac{A(r)}{er} \quad \Phi_a = v\hat{r}^a Q(r) \tag{2.9}$$

where a, b are gauge indices, i is a spatial index, $\hat{r}$ is a unit radial vector, e is the gauge coupling, and $A(r) = Q(r) = 1$ for $r > r_M$ and $A(r) = Q(r) = 0$ for $r < r_M$, where r_M is the radius of the monopole core and $U(\lambda) = \exp(-ie\lambda(t,r)\hat{r}_a\tau_a/2)$ where τ_a are the generators of the $SU(2)$ gauge group. One can show that this field yields electric and magnetic fields

$$B_a^i = \frac{\hat{r}_a\hat{r}_i}{er^2} \quad E_a^i = \hat{r}_a\hat{r}_i\dot{\lambda}'(t,r) \tag{2.10}$$

where it is understood that the primes are derivatives with respect to r and the dots are derivatives with respect to time. $\dot{\lambda}'(r,t)$ describes a radial electric field degree of freedom around the monopole. Let us plug this background gauge field into the pure gauge sector of our Lagrangian found in 2.1.

$$L_{Gauge} = \int_0^\infty dr(4\pi r^2)\left(\frac{1}{2}(E_{a,i}^2 - B_{a,i}^2) + \frac{\theta e^2}{8\pi^2}E_{a,i}B_{a,i}\right) \tag{2.11}$$

We will only keep the terms that contain λ as it is the only remaining degree of freedom in the gauge sector.

$$L_{Gauge} = \int_0^\infty dr 2\pi r^2\dot{\lambda}'^2 + \frac{\theta e}{2\pi}\dot{\lambda}' \tag{2.12}$$

2.2.2 $J = 0$ Fermion Modes

This background gauge field is rotationally symmetric as long as spatial rotations about some axis by an angle θ must be compensated by a gauge rotation by $-\theta$ about that same axis in gauge space. This breaks rotational symmetry and gauge symmetry into its diagonal subgroup (crossed with the electromagnetic $U(1)$ group) where one transforms both the gauge and rotational degrees of freedom equally and opposite. This implies that the unitary operator

$U(\theta_a) = \exp(-iJ^a\theta^a)$, defined as

$$e^{-i\boldsymbol{J}\cdot\boldsymbol{\theta}} = e^{-i(\boldsymbol{L}+\boldsymbol{S})\cdot\theta}e^{i\frac{\boldsymbol{\tau}}{2}\cdot(-\theta)} = e^{-i(\boldsymbol{L}+\boldsymbol{\sigma}/2+\boldsymbol{\tau}/2)\cdot\theta} \tag{2.13}$$

where $\boldsymbol{\tau}$ and $\boldsymbol{\sigma}$ are both Pauli matrices acting on gauge and spin indices respectively, leaves the Lagrangian invariant. We can therefore interpret $\boldsymbol{J}$ as the total angular momentum operator on fermions. We are interested in fermions states that interact with the monopole core and thus have $\boldsymbol{J} = 0$. One can find the most general form of the $\boldsymbol{J} = 0$ state is a superposition of two states

$$\chi_{J=0} = g(r,t)\chi_{J=0;L=0} + p(r,t)\chi_{J=0;L=1} = \frac{g(r,t) + p(r,t)(\hat{\boldsymbol{r}}\cdot\boldsymbol{\sigma})}{\sqrt{4\pi r^2}}|\boldsymbol{\tau}+\boldsymbol{\sigma}=0\rangle \tag{2.14}$$

where $|\boldsymbol{\tau}+\boldsymbol{\sigma}=0\rangle$ is the spin-isospin singlet state which can be thought of as 2×2 matrix $i\sigma^2_{a\alpha}$ with mixed gauge and spin indices. In appendix A.1 we derive the following identities for any χ in the $\boldsymbol{J}=0$ mode.

$$i\chi^\dagger\bar{\sigma}^\mu\partial_\mu\chi = \frac{i}{4\pi r^2}\left(\bar{\xi}\bar{\gamma}^\mu\partial_\mu\xi - \frac{1}{r}\bar{\xi}\bar{\gamma}^5\xi\right) \tag{2.15}$$

$$j^0 \equiv \chi^\dagger\bar{\sigma}^0\chi = \frac{1}{4\pi r^2}\bar{\xi}\bar{\gamma}^0\xi \tag{2.16}$$

$$j^r \equiv \hat{r}_i\chi^\dagger\bar{\sigma}^i\chi = \frac{1}{4\pi r^2}\bar{\xi}\bar{\gamma}^1\xi$$

$$j^0_{EM} \equiv \chi^\dagger(\hat{\boldsymbol{r}}\cdot\boldsymbol{\tau})\bar{\sigma}^0\chi = \frac{1}{4\pi r^2}\bar{\xi}\bar{\gamma}^1\xi \tag{2.17}$$

$$j^r_{EM} \equiv \hat{r}_i\chi^\dagger(\hat{\boldsymbol{r}}\cdot\boldsymbol{\tau})\bar{\sigma}^i\chi = \frac{1}{4\pi r^2}\bar{\xi}\bar{\gamma}^0\xi$$

$$e\chi^\dagger\bar{\sigma}^i\frac{\tau^a}{2}\chi A^a_i = \frac{i}{4\pi r^2}\frac{A(r)}{r}\bar{\xi}\bar{\gamma}^5\xi \tag{2.18}$$

where ξ and $\bar{\gamma}^\mu$ are 1+1D fermions and 1+1D gamma matrices respectively defined as

$$\xi = \frac{1}{\sqrt{2}} \begin{pmatrix} g - p \\ -i(g + p) \end{pmatrix} \qquad \bar{\gamma}^0 = \sigma_2 \quad \bar{\gamma}^1 = i\sigma_1 \quad \bar{\gamma}^5 = \sigma_3. \tag{2.19}$$

This reduces the fermion sector of the 1+3D Lagrangian to a 1+1D Lagrangian

$$L_{\text{Fermion}} = \int d^3\boldsymbol{r}\ i\chi_i^\dagger \bar{\sigma}^\mu D_\mu \chi_i = \int_0^\infty dr\ i\bar{\xi}_i \bar{\gamma}^\mu \partial_\mu \xi_i + \frac{e}{2}\dot{\lambda}(r,t)\bar{\xi}_i\bar{\gamma}^1\bar{\xi}_i + i\frac{A(r)-1}{r}\bar{\xi}_i\bar{\gamma}^5\xi_i. \tag{2.20}$$

In appendix A we show that the last term in this Lagrangian imposes the boundary condition $p(r = r_M) = 0$ where r_M is the mass of the monopole if the solution is to be well-behaved and finite. Physically, this reflects p corresponding to the $\boldsymbol{L} = 1$ portion of the $\boldsymbol{J} = 0$ mode and so is pushed away from the core once rotational symmetry and gauge symmetry become decoupled at $r = r_M$. With this boundary condition established, since we are interested in the fermion state outside of the core, we can set $A(r) = 1$ and remove this term from the Lagrangian.

Next, we insert the $\boldsymbol{J} = 0$ modes into the two types of mass terms. To start we can insert Eq. 2.14 into Eq. 2.2 and 2.4. We find

$$-4\pi r^2 \delta\mathcal{L}_{SO(N_f)} = 4\pi r^2 im\chi_{i,+}\chi_{i,-} + h.c. = -im\frac{(g_i + p_i)(g_i - p_i)}{2} + h.c. \tag{2.21}$$

$$\begin{aligned} -4\pi r^2 \delta\mathcal{L}_{Sp(N_f)} &= 4\pi r^2 m(\chi_{A,i,+}\chi_{B,i,-} - \chi_{B,i,+}\chi_{A,i,-}) \\ &= -m\left(\frac{(g_{B,i} + p_{B,i})(g_{A,i} - p_{A,i})}{2} - \frac{(g_{A,i} + p_{A,i})(g_{B,i} - p_{B,i})}{2}\right). \end{aligned} \tag{2.22}$$

Neither of these looks much like a mass term for our 1+1D fermions. To rectify this, we can redefine our ξ's in both theories so that the above expressions better map onto mass terms for our

1+1D fermions. Noting that in our basis of 1+1D gamma matrices,

$$L_{mass} = -\int_0^\infty dr m\bar{\xi}_i\xi_i = -m\int_0^\infty dr\left(i\xi_-^*\xi_+ + h.c.\right) \quad \text{where} \quad \xi = \begin{pmatrix}\xi_+ \\ \\ \xi_-\end{pmatrix}, \tag{2.23}$$

we can see that if we redefine ξ for the $SO(N_f)$ type mass terms as

$$\xi_i = \frac{1}{\sqrt{2}}\begin{pmatrix} g_i - p_i \\ \\ -(g_i^* + p_i^*)\end{pmatrix} \tag{2.24}$$

and define $\xi_{\ell,i}$ and $\xi_{b,i}$ for the $Sp(N_f)$ type mass terms as

$$\xi_{b,i} = \frac{1}{\sqrt{2}}\begin{pmatrix} g_{A,i} - p_{A,i} \\ \\ i(g_{B,i}^* + p_{B,i}^*)\end{pmatrix} \qquad \xi_{\ell,i} = \frac{1}{\sqrt{2}}\begin{pmatrix} g_{B,i} - p_{B,i} \\ \\ -i(g_{A,i}^* + p_{A,i}^*)\end{pmatrix}, \tag{2.25}$$

the mass terms in Eq 2.21 and 2.22 have the take the form $m\bar{\xi}\xi$ for the various 1+1D fermions. These redefinitions of the ξ's will naturally cause changes to the other terms in the Lagrangian in Eq. 2.20. However, it is not difficult to show that the kinetic terms are unchanged and the currents change as follows:

$$SO(N_f): \quad \bar{\xi}_i\gamma^0\xi_i \to \bar{\xi}_i\gamma^1\xi_i \quad \bar{\xi}_i\gamma^1\xi_i \to \bar{\xi}_i\gamma^0\xi_i \tag{2.26}$$

$$
\begin{aligned}
Sp(N_f): \quad & \bar{\xi}_{A,i}\gamma^0\xi_{A,i} + \bar{\xi}_{B,i}\gamma^0\xi_{B,i} \to \bar{\xi}_{b,i}\gamma^1\xi_{b,i} + \bar{\xi}_{\ell,i}\gamma^1\xi_{\ell,i} \\
& \bar{\xi}_{A,i}\gamma^1\xi_{A,i} + \bar{\xi}_{B,i}\gamma^1\xi_{B,i} \to \bar{\xi}_{b,i}\gamma^0\xi_{b,i} + \bar{\xi}_{\ell,i}\gamma^0\xi_{\ell,i} \\
& \bar{\xi}_{A,i}\gamma^0\xi_{A,i} - \bar{\xi}_{B,i}\gamma^0\xi_{B,i} \to \bar{\xi}_{b,i}\gamma^0\xi_{b,i} - \bar{\xi}_{\ell,i}\gamma^0\xi_{\ell,i} \\
& \bar{\xi}_{A,i}\gamma^1\xi_{B,i} - \bar{\xi}_{A,i}\gamma^1\xi_{B,i} \to \bar{\xi}_{b,i}\gamma^1\xi_{b,i} - \bar{\xi}_{\ell,i}\gamma^1\xi_{\ell,i}.
\end{aligned} \tag{2.27}
$$

This change in the ξ's also affects the boundary conditions at the monopole core. Directly from Eq. 2.24 and 2.25, we can see, the condition $p_i(r=0)=0$ implies that at $r=0$

$$
SO(N_f): \quad \xi_{i,+} = -\xi^*_{i,-} \tag{2.28}
$$

$$
Sp(N_f): \quad \xi_{\ell,i,+} = i\xi^*_{b,i,-} \quad \xi_{b,i,+} = -i\xi^*_{b,i,-} \tag{2.29}
$$

where ξ_+ and ξ_- are the upper and lower components of the spinors respectively. These conditions also imply boundary conditions on the fermion currents at $r=0$

$$
SO(N_f) \text{ Theory:} \quad \bar{\xi}_i\bar{\gamma}^0\xi_i = 0 \tag{2.30}
$$

$$
Sp(N_f) \text{ Theory:} \quad \bar{\xi}_{b,i}\bar{\gamma}^0\xi_{b,i} + \bar{\xi}_{\ell,i}\bar{\gamma}^0\xi_{\ell,i} = 0 \quad \bar{\xi}_{b,i}\bar{\gamma}^1\xi_{b,i} - \bar{\xi}_{\ell,i}\bar{\gamma}^1\xi_{\ell,i} = 0. \tag{2.31}
$$

The difference in boundary conditions between the two theories is a reflection of the difference in UV flavor symmetries. In fact, other than these boundary conditions, the two theories are identical and have Lagrangian

$$
L = \int_0^\infty dr\ \bar{\xi}_{\ell,i}(i\not{\partial} - m_{\ell,i})\xi_{\ell,i} + \bar{\xi}_{b,i}(i\not{\partial} - m_{b,i})\xi_{b,i} + \frac{e}{2}\dot{\lambda}(\bar{\xi}_{b,i}\gamma^0\xi_{b,i} + \bar{\xi}_{\ell,i}\gamma^0\xi_{\ell,i}) + \frac{\theta e}{2\pi}\dot{\lambda}' + 2\pi r^2\dot{\lambda}'^2. \tag{2.32}
$$

Note, we have now included the possibility that the different fermions have different masses as discussed in Section 2.1.

2.3 Bosonization

It has long been established that there is a duality between theories of bosons and fermions in 1+1D [81,82]. This equivalence was first realized by Colman and Mandelstam and has become a staple of field theory and condensed matter theory since. Callan used this equivalence to derive a bosonic theory for fermions around a monopole for the $Sp(N_f)$ theories with $N_f = 2$ [5, 8]. In this section, we generalize this process to include $SO(N_f)$ theories. Appendix A.3.1 provides a detailed derivation and proof of the bosonization. There we show that both theories of N_f fermions, ξ_i, are equivalent to a theory of N_f scalars ϕ_i in in 1+1D that obey a Lagrangian L=$\int_0^\infty dr\ \frac{1}{2}\partial_\mu\phi_i\partial^\mu\phi_i - m_i\frac{\mu_i e^{\gamma-F(r)}}{2\pi}(1- :\cos(2\sqrt{\pi}\phi_i(r,t)) :) + \frac{e\dot{\lambda}}{2\sqrt{\pi}}\partial_r\phi_i(r,t) + \frac{e\theta}{2\pi}\dot{\lambda}' + 2\pi r^2\dot{\lambda}'^2$ (2.32) where there is an implied sum over all flavors i, the colons indicate the normal ordering of the scalar operators, and μ_i is some yet-to-be-determined scale factor. For the $Sp(N_f)$ theories $F(r) = 0$ while for the $SO(N_f)$ theories, $F(r) = K_0(2\mu_i r)$ where K_0 is the zeroth modified Bessel function of the second kind. We also establish a correspondence between the fermion currents and derivatives of the scalar fields

$$j^i_\mu = \bar{\xi}_i\gamma^\mu\xi_i = \epsilon^{\mu\nu}\frac{\partial_\nu\phi_i}{\sqrt{\pi}} \tag{2.33}$$

where $\epsilon^{01} = 1$ and is the antisymmetric tensor in two dimensions. This equivalence is achieved by making the substitution

$$\xi_i(r,t) = Z^{1/2}(r) : \begin{pmatrix} e^{i\sqrt{\pi}\left(\phi(r,t) - \int_0^r dx \dot{\phi}(x,t)\right)} \\ e^{i\alpha} e^{-i\sqrt{\pi}\left(\phi(r,t) + \int_0^r dx \dot{\phi}(x,t)\right)} \end{pmatrix} : . \tag{2.34}$$

$Z(r)$ is an overall normalization factor that is unimportant outside of the computations in appendix A.3.1 and α is some overall phase. α, as well as the boundary conditions on the scalar fields, can be determined by applying Eq. 2.28 and 2.30 to Eq. 2.33 and 2.34. For the $SO(N_f)$ theories we find that $\alpha = \pi$ and the scalar fields obey boundary conditions

$$\partial_r \phi_i(r=0) = 0. \tag{2.35}$$

For the $Sp(N_f)$ theories we find that we may choose $\alpha = \pi$ and then we are left with the boundary conditions

$$\phi_{\ell,i}(r=0) - \phi_{b,i}(r=0) = 0 \text{ mod } 2\sqrt{\pi} \quad \partial_r \phi_{\ell,i}(r=0) + \partial_r \phi_{b,i}(r=0) = 0. \tag{2.36}$$

Before using these scalar theories to compute the bound states, it will be necessary and useful to make the following three simplifications to the Lagrangian,

1. We rescale our field $\phi \to \phi/2\sqrt{\pi}$ which makes the theory much simpler to analyze by removing the various $\sqrt{\pi}$ factors from the bosonization process

2. We integrate out the electric field by solving the equations of motion for the electric field

$\dot{\lambda}'$. This is done easily by integrating the third to last term in Eq. 2.45 by parts to find

$$\dot{\lambda}' = \frac{e}{4\pi r^2}\left(\sum_i \frac{\phi_i}{4\pi} - \frac{\theta}{2\pi}\right). \tag{2.37}$$

Note that this has a very physical interpretation that the electric charge enclosed in a radius r, $Q_{EM}(r)$, is given by the term in parenthesis in Eq. 2.37

3. Finally, we notice that far from the monopole core, the theory reduces to a set of uncoupled scalar satisfying the sine-Gordon equations. The sine-Gordon is known to have soliton solutions and it is these solutions that correspond to fermion states as was proven by Mandelstam [82]. We fix the scales μ_i by demanding that the solitons far from the monopole have energy m_i. More will be said about the soliton solution in Section 2.4.

After all of these simplifications, the Lagrangian for the theories becomes

$$L = \frac{1}{4\pi}\int_0^\infty dr\ \sum_i \left(\frac{1}{2}\partial_\mu\phi_i\partial^\mu\phi_i - \left(\frac{\pi m_i(r)}{2}\right)^2 (1- : \cos(\phi_i(r,t)) :)\right) - \frac{\alpha}{8\pi r^2}\left(\sum_i \phi_i - 2\theta\right)^2 \tag{2.38}$$

where $\alpha \equiv e^2/4\pi$ and the sums over i include all flavors of scalar with the conditions/definitions

$$Sp(N_f)\text{ Theories:}\quad \phi_{\ell,i}(r=0) - \phi_{b,i}(r=0) = 0 \quad \text{Mod } 4\pi \tag{2.39}$$

$$\partial_r\phi_{\ell,i}(r=0) + \partial_r\phi_{b,i}(r=0) = 0 \quad m_i(r) = m_i$$

$$SO(N_f)\text{ Theories:}\quad \partial_r\phi_i(r=0) = 0 \quad m_i(r) = m_i \exp\left(-K_0\left(\pi^2 e^{-\gamma} m_i r\right)/2\right). \tag{2.40}$$

Note that $m_i(r)$ approaches m_i for $m_i r \gg 1$ and $\pi m_i\sqrt{m_i r/2}$ for $m_i r \ll 1$ in the $SO(N_f)$ theories.

2.3.1 Solitons

Far from the monopole, the electromagnetic term is negligible and the equations of motion become a set of decoupled the sine-Gordon equations. The sine-Gordon equation famously admits solutions which run from 0 to 2π (or 2π to 0) called solitons(or antisolitons) which have the analytic form

$$\phi_{\text{soliton}}(r,t) = 4\arctan\left(\exp\left(\pi m\gamma(r-vt)/2\right)\right) \tag{2.41}$$

where $\gamma = (1-v^2)^{-1/2}$ is the Lorentz boost factor. A plot of this soliton solution is shown in figure 2.1. Solitons moving with velocity v have energy γm with a soliton at rest having energy m. These solitons, as hinted earlier, correspond to fermions in the original theory. Solitons will be

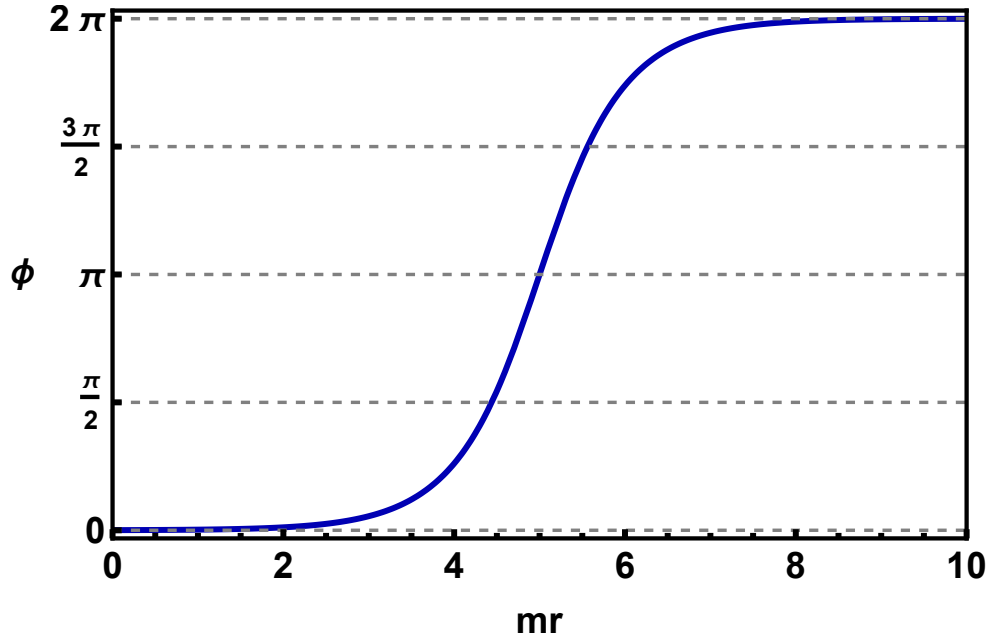

Figure 2.1: A plot of the soliton solution to the equations of motion in the decoupled limit. This soliton solution in the bosonized theory corresponds to a fermion in the original theory.

most important in our analysis of the stability of dyonic states. These dyonic states can transition between each other via the emission of solitons so the question of stability will come down to

whether or not, the difference in energy between these states is less than the energy of a soliton.

2.3.2 Currents in Bosonized Theories

From the current correspondence in Eq. 2.33 and the relations in Eq. 2.16-2.17, we know that derivatives of the ϕ's are related to currents of the original fermions. Using these equations and the definitions of the IR fermions in Eq. 2.3 and 2.5, one can find a direct relation between the current of the IR currents and derivatives of the bosonized scalar fields

$$4\pi r^2 \bar{j}_i^0 = \psi_i \gamma^\mu \psi_i = \epsilon^{\mu\nu} \frac{\partial_\nu \phi_i}{2\pi} \tag{2.42}$$

from which one can easily compute the total charge enclosed in a sphere of radius r, $Q_i(r)$ for any one of these currents as

$$Q_i(t,r) = \int_0^r dr' j_i^0(t,r') = \frac{\phi_i(r,t) - \phi_i(0,t)}{2\pi}. \tag{2.43}$$

In our subsequent discussions we will find it useful to describe solutions to the theory by expressing them in terms of $Q_i(r)$ rather than the fields $\phi_i(r)$ themselves, since $Q_i(r)$ is more directly physically meaningful. We will also adopt the notation $Q_i^{tot} \equiv Q_i(\infty)$ to describe the total charge in a particular field.

The currents, j_i^μ satisfy local conservation laws reflecting the fact that they correspond to, at the very least, accidental symmetries in the IR. However, many of these currents are not conserved in the UV theory. This fact can be realized by considering the boundary conditions at $r = 0$. For example, consider the electromagnetic current, $j_{EM}^\mu = \frac{1}{2}\sum_i j_i^\mu$, where the $1/2$ reflects

the fact that each fermion has charge $e/2$. The total electric charge is conserved by looking at $\dot{Q}_{EM}(t,\infty)$.

$$\dot{Q}_{EM}(t,\infty) = \sum_i \frac{\dot{\phi}_i(\infty,t) - \dot{\phi}_i(0,t)}{4\pi} \tag{2.44}$$

Notice as well that the electric charge $Q_{EM}(r)$ and the sum of all the charges $Q_i(R)$ in each field differ by a factor of $1/2$ since the fermions have charge $1/2$ in units of e. From the Lagrangian in Eq. 2.45 one can deduce that the only solutions with finite energy are those with $\phi_i(r = \infty) = 2\pi n_i$ where n_i is an integer and $\frac{1}{2}\sum_i \phi_i = \theta$. Thus, Eq. 2.44 reduces to $\dot{Q}_{EM}(t,\infty) = 0$ reflecting that electromagnetic charge is conserved in both the $SO(N_f)$ and $Sp(N_f)$ theories. Similarly, from the boundary conditions in Eq. 2.39 one can see that the $Sp(N_f)$ theory contains $N_f/2$ conserved $B-L$-type currents, $j^\mu_{b,i} - j^\mu_{\ell,i}$, whereas the $SO(N_f)$ does not contain any such currents.

2.4 $N_f = 1$ Toy model

Although much simpler mathematically, the bosonized theories derived in section 2.3 bear little resemblance to the original 1+3D theory of fermions. It will therefore be useful to briefly study the properties of a simplified version of our bosonized model with $N_f = 1$ to show how to relate results found in our computations from the bosonized theory to physical results in the original 1+3D theory. We will establish some analytic approximations for the bound states and their energies which will prove to be very useful when considering $N_f > 1$.

There are several ways to arrive at this $N_f = 1$ theory from a more realistic theory. The simplest way is to start with an $N_f = 2$ theory and decouple one of the two fermions. Another is to take any N_f and look for a solution where all of the bosonized scalar profiles are identical,

a solution that exists and is important for both $SO(N_f)$ and $Sp(N_f)$ flavor symmetries, albeit with slightly different α and θ in the $N_f = 1$ theory than in the original theory. Regardless, the Lagrangian for the $N_f = 1$ theory can be expressed

$$L = \frac{1}{4\pi}\int_0^\infty dr\ \frac{1}{2}\partial_\mu\phi\partial^\mu\phi - \left(\frac{\pi m}{2}\right)^2(1-\cos(\phi)) - \frac{\alpha}{8\pi r^2}(\phi-\theta)^2 \tag{2.45}$$

for which the time-independent equation of motion is

$$\partial_r^2\phi = \frac{\pi^2 m^2}{4}\sin\phi + \frac{\alpha}{4\pi r^2}(\phi-\theta). \tag{2.46}$$

The dyonic states we are after are defined to be solutions to this equation of motion of minimal energy. We apply the boundary condition $\partial_r\phi = 0$ at $r = 0$ for simplicity. As discussed at the end of section 2.3, demanding our solutions have finite energy requires $\phi(r=0) = \theta$ and $\phi(r=\infty) = 2\pi q$ where q is an integer. This seems to imply an infinite tower of dyonic states, which we denote $\mathcal{D}_q$, one for each choice of q with total electric charge $Q_{EM}^{tot} = q - \theta/2\pi$. However, it is easy to see that for states with $|Q_{EM}^{tot}| > 1$, the energy will be minimized by putting some number of solitons at $r = \infty$ which can hardly be considered a bound state. Thus in our $N_f = 1$ theory, there are only two potentially stable bound dyonic states for $0 < \theta < 2\pi$: $\mathcal{D}_0$ and $\mathcal{D}_1$. These states are sketched in figure 2.2 in terms of $Q(r)$ the total charge enclosed in a radius, r to reflect the physics more clearly, defined in Eq. 2.43. We can find useful analytic approximations to this solution in the $mr \ll 1$ and $mr \gg 1$ limits. For $mr \ll 1$, the mass term in Eq. 2.46 can be neglected and we naturally have the trivial solution $\phi = \theta$. However, as we will see, for theories with $N_f > 1$, ϕ is occasionally forced to take values other than this trivial

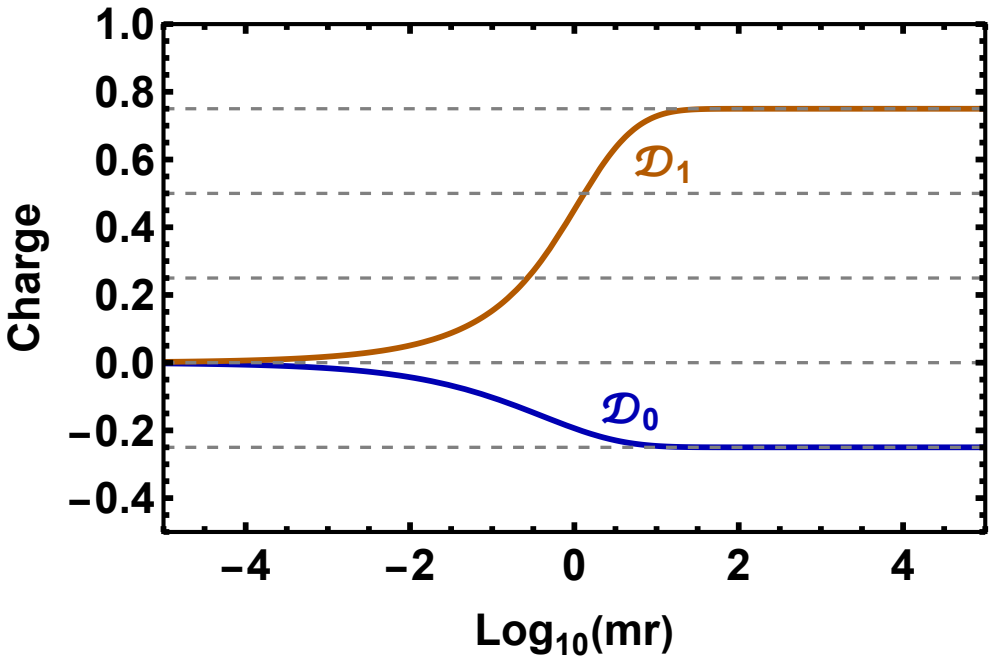

Figure 2.2: An example of the two potentially stable dyonic states in our $N_f = 1$ toy model for $\alpha = 0.1$ and $\theta = \pi/2$. These states are plotted in terms $Q(r) = \frac{\phi(r)-\phi(0)}{2\pi}$, the total charge enclosed in a radius r of the monopole core.

one in the $mr \ll 1$ regime so it will be important to consider other solutions. Say, for example, ϕ must satisfy $\phi(r = r_0) = \phi_0$. Then we can solve Eq. 2.46, neglecting the mass term to find

$$\phi = \theta + (\phi_0 - \theta)\left(\frac{r}{r_0}\right)^{-\beta} \quad \text{where} \quad \beta = \frac{1}{2}\left(\sqrt{1+\frac{\alpha}{\pi}} - 1\right) \approx \frac{\alpha}{4\pi} \tag{2.47}$$

and where we have taken the $\alpha \ll 1$ limit in the last step of both equations. We physically interpret this solution as ϕ attempting to minimize the electromagnetic energy by asymptotic toward θ with a power law decay to screen the residual charge. However, this power law can be extremely slow in the small α limit. As we will see in later sections, this screening effect can lead to very interesting phenomena. We may also consider the $mr \gg 1$ limit, where the gradient term can be neglected in Eq. 2.46 and the mass term can be balanced against the electromagnetic

term to find

$$\phi(r) = \begin{cases} \frac{\theta}{1+\frac{\pi}{\alpha}(\pi m r)^2} & \text{if} \quad n = 0 \\ 2\pi - \frac{2\pi-\theta}{1+\frac{\pi}{\alpha}(\pi m r)^2} & \text{if} \quad n = 1 \end{cases} . \tag{2.48}$$

To study the stability of the states in figure 2.2, consider what would happen if one increases θ. This raises the energy of the $\mathcal{D}_0$ dyon and lowers the energy of the $\mathcal{D}_1$ dyon. Eventually, at some critical $\theta = \theta_c$, it will become energetically favorable for the $\mathcal{D}_0$ dyon to decay into the $\mathcal{D}_1$ dyon through the emission of an antisoliton at $r = \infty$. Thus, for $\theta > \theta_c$ the $\mathcal{D}_0$ becomes unstable. θ_c can be found by solving

$$E_0(\theta_c) - E_1(\theta_c) - m = 0 \tag{2.49}$$

where $E_q(\theta)$ is the energy of the $\mathcal{D}_q$ dyon as a function of θ. Due to the symmetry of the solutions, a similar argument shows that $\mathcal{D}_1$ will become unstable to the emission of a soliton at $\theta = 2\pi - \theta_c$. For $2\pi - \theta_c < \theta < \theta_c$, both $\mathcal{D}_0$ and $\mathcal{D}_1$ will be stable. $E_q(\theta)$ can be computed from numerical solutions like those in figure 2.2, and θ_c in turn can be computed numerically from these energies. These numerical results are shown in the solid lines in figure 2.3. However, it will be useful to have an analytic approximation for E_n that can also be used to predict θ_c. To start, consider the Hamiltonian for the theory, given in Eq. 2.50. This Hamiltonian can be broken into two contributions, mechanical energy and electromagnetic energy, represented by the first two terms and the last term respectively.

$$H = \frac{1}{4\pi}\int_0^\infty dr\ \frac{1}{2}\phi'^2 + \frac{1}{2}(m\pi)^2 \sin^2\left(\frac{\phi}{2}\right) + \frac{\alpha}{8\pi r^2}(\phi - \theta)^2 \tag{2.50}$$

We can analytically approximate the mechanical energy by multiplying the Eq. 2.46 by ϕ',

neglecting the electromagnetic term, and integrating in from infinity, to find

$$(\phi')^2 = (m\pi)^2 \sin^2(\phi/2). \tag{2.51}$$

Using this and Eq. 2.51, one can integrate the mechanical portion of the Hamiltonian analytically to find

$$E_q^{mech}(\theta, m) = m \sin^2\left(\frac{\pi}{2} Q_{EM}^{tot}(q, \theta)\right). \tag{2.52}$$

The electromagnetic energy can be estimated by crudely approximating ϕ as step function with $\phi = \theta$ for $mr < 1$ and $\phi = 2\pi n$ for $mr > 1$. With this approximation the electromagnetic contribution to the energy is

$$E_q^{\mathrm{EM}}(\theta, \alpha, m) \approx \frac{\alpha}{2} m \left(\frac{Q_{EM}^{tot}(q, \theta)}{2}\right)^2. \tag{2.53}$$

Combining these two contributions to the energy gives an analytic approximation of the energy

$$E_q(\theta, \alpha, m) \approx m \left(\sin^2\left(\frac{\pi}{2} Q_{EM}^{tot}(q, \theta)\right) + \frac{\alpha}{2}\left(\frac{Q_{EM}^{tot}(q, \theta)}{2}\right)^2\right) \tag{2.54}$$

which, inserted into Eq. 2.49, gives the following analytic equation for θ_c

$$\cos^2\left(\frac{\theta_c}{4}\right) = \frac{\alpha}{8}\left(\frac{\theta_c}{\pi} - 1\right). \tag{2.55}$$

This equation highlights that it is the balancing of mechanical energy and electromagnetic energy

that determines the stability. If $\alpha = 0$, then $\theta_c = 2\pi$ and $\mathcal{D}_0$ is always stable. However, for nonzero α, $\mathcal{D}_0$ gets some electromagnetic energy that it can use to overcome the energy gap due to the mechanical energy. The larger the α the more electromagnetic energy it has and the smaller θ_c at which it can make the transition. The left-hand side is small if $\alpha \lesssim 1$ and we can justify expanding around $\theta_c \approx 2\pi$ to the lowest order to find the following analytic approximation for θ_c.

$$\theta_c = 2\pi - \frac{\alpha}{2\pi}\left(\sqrt{1 + \frac{4\pi^2}{\alpha}} - 1\right) \tag{2.56}$$

Figure 2.3 shows a comparison between the approximations for the energy and θ_c and the numerical results. While the two energy plots are quite well approximated, the analytic approximation to θ_c seems to be less accurate. This is due to the crude approximation of the electromagnetic energy being the leading effect in determining θ_c while it is a subleading effect on the total energy of any particular state.

2.5 $N_f = 2$

In this section, we perform a thorough analysis of the two theories for $N_f = 2$. In the IR, both theories consist of 4 left-handed Weyl fermions ℓ, b, ℓ^c and b^c with mass terms that couple ℓ to ℓ^c and b to b^c. The IR theory appears to contain an $SU(2)$ flavor symmetry which includes $U(1)_{B-L}$ as a subgroup. However, from the UV perspective, the theories are very different, as can be seen in table 2.2. Most significantly, $U(1)_{B-L}$ is only a good symmetry for the $Sp(2)$ theory and is anomalous in the $SO(2)$ theory in the UV. After bosonization, the Lagrangian for

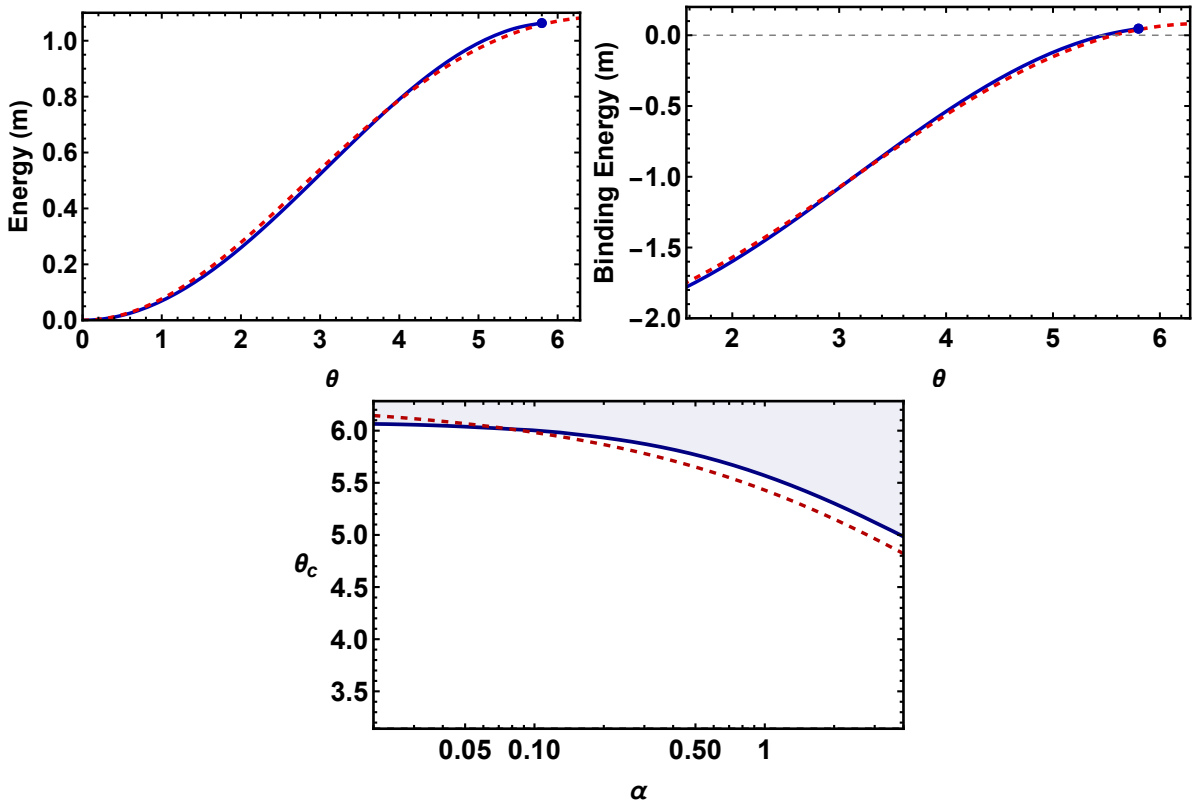

Figure 2.3: Various plots displaying the accuracy of the analytic approximations (dash red lines) in comparison to numerical simulation (blue). The first two plots show the energy $E_0(\theta, \alpha, m)$ and the binding energy $E_0(\theta, \alpha, m) - E_1(\theta, \alpha, m)$ taken for $\alpha = 0.6$. The blue numerical line ends at a certain θ when the system becomes classically unstable to decay. The bottom plot shows a plot of θ_c.

both theories is

$$L = \frac{1}{4\pi}\int_0^\infty dr\ \frac{1}{2}\left(\partial_\mu\phi_\ell\partial^\mu\phi_\ell + \partial_\mu\phi_b\partial^\mu\phi_b\right) - \left(\frac{\pi m_\ell(r)}{2}\right)^2\left(1-\cos(\phi_\ell)\right) \qquad (2.57)$$
$$- \left(\frac{\pi m_b(r)}{2}\right)^2\left(1-\cos(\phi_b)\right) - \frac{\alpha}{8\pi r^2}\left(\phi_\ell + \phi_b - 2\theta\right)^2$$

$SO(2)$ Flavor Symmetric

	$SU(2) \to U(1)_{EM}$	$U(1)_{B-L}$
$\begin{pmatrix} b \\ b^c \end{pmatrix}$	$\square \to \begin{pmatrix} \frac{1}{2} \\ -\frac{1}{2} \end{pmatrix}$	1
$\begin{pmatrix} \ell \\ \ell^c \end{pmatrix}$	$\square \to \begin{pmatrix} \frac{1}{2} \\ -\frac{1}{2} \end{pmatrix}$	-1

$Sp(2)$ Flavor Symmetric

	$SU(2) \to U(1)_{EM}$	$U(1)_{B-L}$
$\begin{pmatrix} b \\ \ell^c \end{pmatrix}$	$\square \to \begin{pmatrix} \frac{1}{2} \\ -\frac{1}{2} \end{pmatrix}$	1
$\begin{pmatrix} \ell \\ b^c \end{pmatrix}$	$\square \to \begin{pmatrix} \frac{1}{2} \\ -\frac{1}{2} \end{pmatrix}$	-1

Table 2.2: The charges on the fermions in the 2 theories. Note that in the $SO(2)$ theory, $B-L$ is an anomalous symmetry while in $Sp(2)$ it is a good symmetry

which gives the equations of motion

$$\begin{aligned} \partial_r^2 \phi_b &= \left(\frac{\pi m_b(r)}{2}\right)^2 \sin(\phi_b) + \frac{\alpha}{4\pi r^2}\left(\phi_b + \phi_\ell - 2\theta\right) \\ \partial_r^2 \phi_\ell &= \left(\frac{\pi m_\ell(r)}{2}\right)^2 \sin(\phi_\ell) + \frac{\alpha}{4\pi r^2}\left(\phi_b + \phi_\ell - 2\theta\right) \end{aligned} \tag{2.58}$$

where $m_{\ell,b}(r) = m_{\ell,b}$ for the $Sp(2)$ theory and

$$m_i(r) = m_i e^{-\frac{1}{2}K_0(\pi^2 e^{-\gamma} m_i r)} = m_i \begin{cases} 1 & \text{if} \quad m_i r \gg 1 \\ \\ \pi\sqrt{\frac{m_i r}{2}} & \text{if} \quad m_i r \ll 1 \end{cases} \tag{2.59}$$

for the $SO(2)$ theory. Note that both theories are symmetric under the exchange of the labels $b \longleftrightarrow \ell$, so we can always take $m_b \geq m_\ell$. The boundary conditions at $r = 0$ are

$$SO(2): \quad \partial_r \phi_\ell = \partial_r \phi_b = 0 \tag{2.60}$$

$$Sp(2): \quad \partial_r \phi_\ell = -\partial_r \phi_b \quad \phi_\ell = \phi_b. \tag{2.61}$$

Finite energy forces the boundary conditions $\phi_{b,\ell}(r = \infty) = 2\pi n_{b,\ell}$ and $\phi_b(0) + \phi_\ell(0) = 2\theta$. States that satisfy these boundary these conditions carry electromagnetic and $B - L$ charges

$$\begin{aligned} Q_{EM}^{tot} =& \frac{n_\ell + n_b}{2} - \frac{\theta}{2\pi} \\ Q_{B-L}^{tot} =& n_\ell - n_b - \frac{\phi_b(0) - \phi_\ell(0)}{2\pi}. \end{aligned} \tag{2.62}$$

The total charge in each field can be related to the total electric charge, Q_{EM}^{tot} (in units of e) and the total $B - L$ charge Q_{B-L}^{tot}

$$Q_b^{tot} = Q_{EM}^{tot} + \frac{Q_{B-L}^{tot}}{2} \quad Q_\ell^{tot} = Q_{EM} - \frac{Q_{B-L}^{tot}}{2}. \tag{2.63}$$

Now we come to a very important physical fact. The boundary condition $\phi_\ell = \phi_b$ in the $Sp(2)$ requires $B - L$ charge conservation at the boundary. This means the total charge stored in each field is fixed by the total electromagnetic charge and the $B - L$ charge of the dyon. In the $SO(2)$ theory $U(1)_{B-L}$ is not a good symmetry and so Q_{B-L}^{tot} is not fixed to take any particular value. Since they are free to take Q_{B-L}^{tot} to take any value, the dyon solutions in the $SO(2)$ theory can shift the portion of the electric charge stored in each field in order to minimize the energy. As we will see, this extra bit of freedom for the $SO(2)$ theory will have many physical consequences.

In analogy with our $N_f = 1$ case, one might expect to find one dyon state (stable or not) for every combination of n_ℓ and n_b. However, in the $SO(2)$ theory, many of these states are

equivalent. To see this, consider the following field redefinitions $S_\ell(n)$ and $S_b(n)$.

$$\begin{aligned} S_b(n)&: \quad \phi_\ell \to \phi_\ell \quad \phi_b \to \phi_b + 2\pi n \quad \theta \to \theta + \pi n \\ S_\ell(n)&: \quad \phi_\ell \to \phi_\ell + 2\pi n \quad \phi_b \to \phi_b \quad \theta \to \theta + \pi n \end{aligned} \tag{2.64}$$

The Lagrangian in Eq. 2.57 is invariant under both of these field redefinitions. The boundary conditions of $SO(2)$ respect both of these symmetries and thus these are valid field redefinitions in $SO(2)$. These can be used to equate dyon solutions in a theory with one value of θ to dyons in a theory with another value of θ. If one considers the redefinition $S_-(n) \equiv S_b(n)S_\ell(-n)$ one finds that it relates dyons in the same theory as this redefinition sends $\theta \to \theta$. One finds an equivalence between states $(n_b, n_\ell) \cong (n_b + 1, n_\ell - 1)$. This collapses the dyon states into a set of equivalence classes which may be indexed by a single quantum number $q = n_b + n_\ell$. Thus dyon solutions are uniquely determined by their electric charge $Q_{EM}^{tot} = q/2 - \theta/2\pi$. We label the dyon solutions in $SO(2)$ as $\mathcal{D}_q$ and the landscape of the states is shown in figure 2.4. Once this equivalence has been made, one can use either $S_\ell(q)$ or $S_b(q)$ to relate the dyons in different theories.

$$\mathcal{D}_q(\theta) = \mathcal{D}_0(\theta + q\pi) \tag{2.65}$$

This implies the energies of these states are the same in the two theories.

$$E_q(\theta) = E_0(\theta + q\pi) \tag{2.66}$$

A similar analysis can be performed on the $Sp(2)$ theory. Here, the boundary conditions do not allow the field redefinitions $S_\ell(n)$ and $S_b(n)$ individually, but only the combination $S_+(n)_b(n)S_\ell(n)$.

This means that there is no equivalence between states of different n_ℓ and n_b in this theory and each combination specifies a unique state. Rather than using n_ℓ and n_b to index our states, it will be more useful to index them as $\mathcal{D}_{q,n_{B-L}}$ as this will reflect more clearly the electric and $B-L$ charges of the specific states. Then we can use $S(n)$ to derive an equivalence between states in theories of different θ and thus their energies.

$$\mathcal{D}_{q,n_{B-L}}(\theta) = \mathcal{D}_{q-2n,n_{B-L}}(\theta + 2\pi n) \tag{2.67}$$

This implies the energies of these states are the same in the two theories.

$$E_{q,n_{B-L}}(\theta) = E_{q-2n,n_{B-L}}(\theta + 2n\pi) \tag{2.68}$$

This equivalence of states in different theories is most easily visualized from the diagrams in figure 2.4 where one can see that by shifting θ a certain amount the states match up with states of either higher or lower electric charge.

2.5.1 Dyonic Solutions

Figure 2.5 shows some sample plots of the dyonic solutions in the two theories. Right away, we see some striking contrasts between the two theories and the importance of their respective boundary conditions. As discussed, $Sp(2)$ states have a fixed amount of charge in each field while the $SO(2)$ states are free to give different charges to each field, giving them more freedom to minimize their energy. Once $m_b \gg m_\ell$, the $SO(2)$ states prefer to give very little charge to the baryon field since doing so costs $\mathcal{O}(m_b)$ energy as opposed to giving it to the lepton which

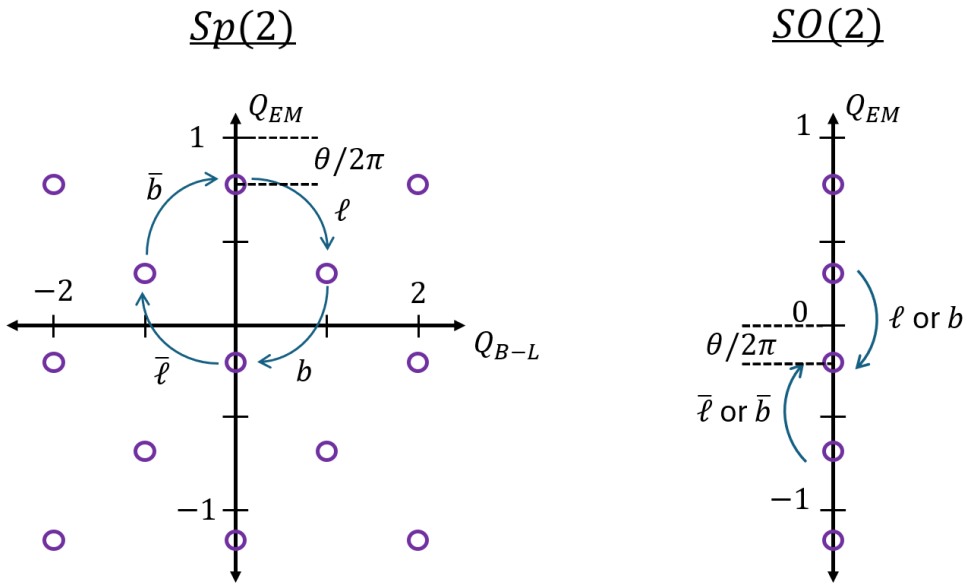

Figure 2.4: A map of the various states in the two theories. The arrows indicate the particles emitted by one state to decay into another. Note in $SO(2)$, the states can decay by either emitting a (anti)lepton or (anti)baryon but if $m_\ell < m_b$, it will energetically prefer to decay into a lepton.

costs $\mathcal{O}(m_\ell)$ energy. The $Sp(2)$ states on the other hand are forced to split the charge according to Eq. 2.63 and thus the state has no choice but to acquire $\mathcal{O}(m_b)$ energies. This can be seen from the energy plots in figure 2.6 where the energy of the $Sp(2)$ states are $\mathcal{O}(m_b)$ and the energies of the $SO(2)$ states are $\mathcal{O}(m_\ell)$.

We see more interesting behavior considering the $m_b \gg m_l$ in the $Sp(2)$ theory. From the bottom left plot in figure 2.5, we see the lepton attempt to screen the baryon's negative charge at $r \approx m_b^{-1}$ by slowly depositing the positive charge. This screening can be quantified by the approximate analytic solution in Eq. 2.47. In this intermediate region $m_b^{-1} < r < m_\ell^{-1}$, we can ignore the mass term and apply the condition that $\phi_\ell(r = m_b^{-1}) = \theta$ to find the approximate solution

$$Q_\ell(r) \approx -Q_b^{tot}(1 - (m_b r)^{-\beta}). \tag{2.69}$$

Physically, the lepton is attempting to screen the charge deposited by the baryon to lower the

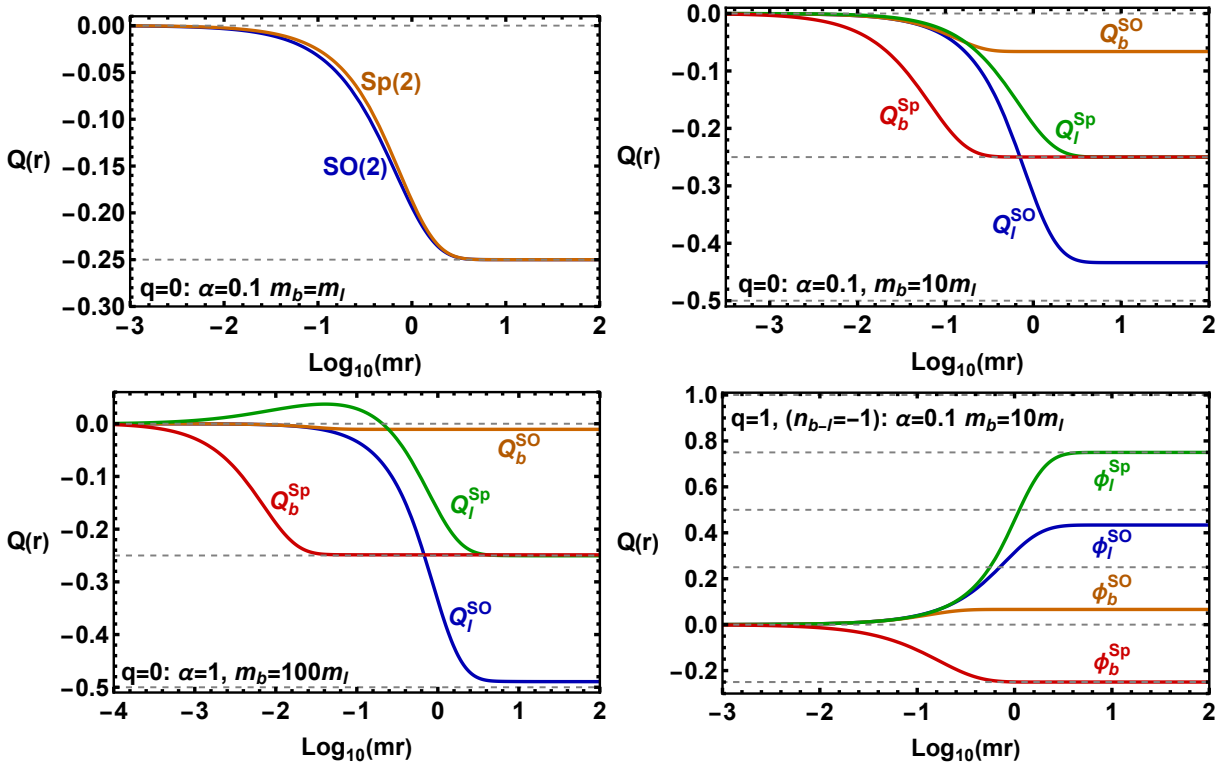

Figure 2.5: A sample of the dyonic solutions for both theories for various masses.

electromagnetic energy. Over this intermediate region, the lepton deposits a charge, Q_{screen}, given by

$$Q_{screen} = Q_b^{tot}((m_b/m_\ell)^{-\beta} - 1) \approx \frac{\alpha Q_b^{tot}}{4\pi} \ln\left(\frac{m_b}{m_\ell}\right) \tag{2.70}$$

where we have taken $\alpha/4\pi \ll 1$ in this last approximation. This screening is extremely weak for small α which can be seen as a consequence of the equations of motion. Since we are ignoring the mass term at these small distances from the core, $\partial_r^2\phi_\ell \sim \mathcal{O}(\alpha m_b^2/4\pi)$ which limits the rate at which the lepton can deposit charge. Comparatively, the baryon can deposit its charge quickly with $\partial_r^2\phi_b \sim \mathcal{O}(m_b^2)$.

Now, let us consider the energy of these states, show in figure 2.6. Although the two dyons in the top left plot in figure 2.5 differ very little, the corresponding energies in figure 2.6 differ by an $\mathcal{O}(1)$ factor. This is because, although the $SO(2)$ theory's radially dependent mass

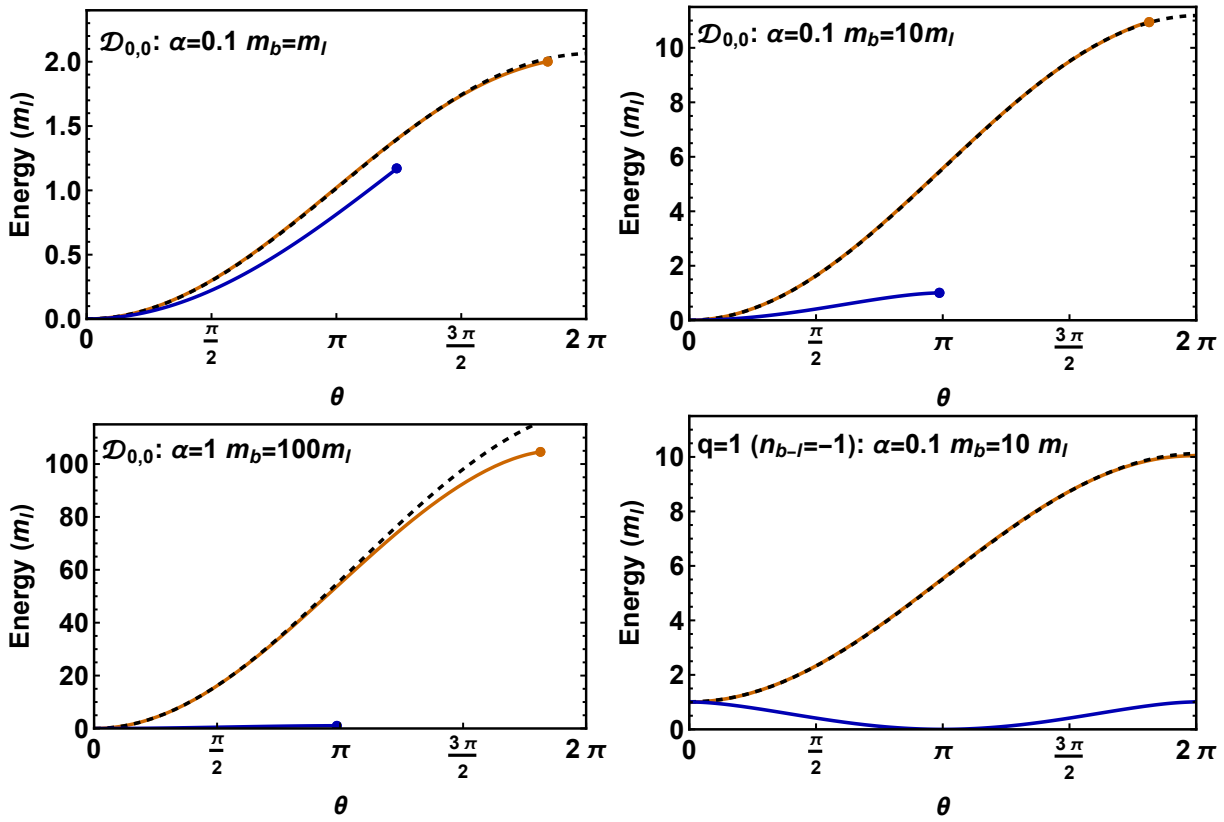

Figure 2.6: A plot of the energies of the states in figure 2.5 as a function of theta. The blue lines are shown for the $SO(2)$ theory, the Orange lines for the $Sp(2)$ theory while the black dashed line represents the analytic approximation for the $Sp(2)$ given in Eq. 2.71.

term does not influence the charge distribution of the state significantly it does significantly change the energy since the energy from the mass term in the Hamiltonian is suppressed at $mr < 1$. Unfortunately, this radial dependence prevents us from using the analytic tricks used in section 2.4 to compute the energy and so we have no way of computing the energy analytically in the $SO(2)$ theory. We do not have this issue for the $Sp(2)$ theories and we can derive an analytic approximation using many of the same techniques as in section 2.4. We can find

$$E_{q,n_{B-L}}(\theta,\alpha,m_b,m_\ell) = m_b \sin^2\left(\frac{\pi}{2}Q_b^{tot}\right) + m_\ell \sin^2\left(\frac{\pi}{2}(Q_\ell^{tot}+Q_{screen})\right) + m_\ell\frac{\alpha}{2}Q_{EM}^2 + E_{mid}(\theta,\alpha,m_b,m_\ell). \tag{2.71}$$

There are two main new considerations. Firstly, due to the aforementioned screening, the lepton must deposit a little extra charge at $r = m_\ell^{-1}$ in addition to its total charge. Secondly, there is some additional energy, both mechanical and electromagnetic, in the intermediate region $m_b^{-1} < r < m_\ell^{-1}$, which was not present in our $N_f = 1$ example, which we have denoted E_{mid}. E_{mid} can be computed in this region using Eq. 2.69. Inserting this solution into the Hamiltonian and ignoring the mass term in the intermediate region, we find

$$\begin{aligned} E_{mid} &= \int_{m_b^{-1}}^{m_\ell^{-1}} dr \frac{\pi Q_\ell'^2(r)}{2} + \frac{\alpha}{8r^2}(Q_\ell(r) + Q_b^{tot})^2 \\ &= \frac{\pi}{2}\frac{\beta^2 + \alpha/4\pi}{1+2\beta}(Q_b^{tot})^2 \left(m_b - m_\ell \left(\frac{m_\ell}{m_b}\right)^{2\beta} \right) \approx \frac{\alpha}{2}\left(\frac{Q_b^{tot}}{2}\right)^2 (m_b - m_\ell) \end{aligned} \tag{2.72}$$

where, in the last line of each, we've taken the $\alpha/4\pi \ll 1$ limit. The analytic approximation given in Eq. 2.71 with Eq. 2.70- 2.72 is plotted alongside the numerical result in figure 2.6 showing good agreement.

2.5.2 Ground State and Stability

We are now in the position to ask about the stability of these dyon states. Firstly we can ask which state is the ground state at a particular point in parameter space by finding the state of lowest energy. For the $SO(2)$ theory it is easy to see from Eq. 2.66 that the ground state is always the state of minimal electric charge as one might have naively expected.

The situation is not so simple for $Sp(2)$ as can be seen in figure 2.7 where we show the ground state as a function of mass difference and coupling using both our numerical and analytic computations for the energy. These plots can be roughly understood by considering the energy

of the $\mathcal{D}_{1,1}$ state and the $\mathcal{D}_{0,0}$ state around $\theta < \pi$. From Eq. 2.71, we can see that in the $\alpha \to 0$ limit, the energy of the two is roughly

$$E_{0,0}(\theta, \alpha = 0, m_b = m_l) = 2m \sin^2(\theta/4) \quad E_{1,0}(\theta, \alpha = 0, m_b = m_l) = m. \tag{2.73}$$

In this limit clearly, the $\mathcal{D}_{0,0}$ would always be the ground state for $\theta < \pi$. Turning on α gives $\mathcal{D}_{0,0}$ some extra electric energy whereas it does not give as much to $\mathcal{D}_{1,1}$ since $\mathcal{D}_{1,1}$ is approximately electronically neutral around $\theta = \pi$. So as we increase α we expect to see more and more area in parameter space where $\mathcal{D}_{1,1}$ is the ground state which is exactly what we see in figure 2.7. Finally, we can ask which of these dyon states are stable. One quick way to eliminate many states from the list of stable candidates is to note that if, $|Q_\ell^{tot}| \geq 1$ or $|Q_b^{tot}| > 1$, then the fermion number in at least in of the fields is ≥ 1. The energy then is minimized by placing fermions at spatial infinity. This limits us to states with electric charge $|Q_{EM}^{tot}| < 1$ and, for $Sp(2)$, $|Q_{B-L}^{tot}| \leq 1$. This immediately limits us to consider at most 3 states in $SO(2)$ and 4 in $Sp(2)$ as can be seen from figure 2.4. If the difference between the energies of any two of these states is greater than the energy of a soliton, then the more energetic dyon can decay into the lower energy dyon through the emission of a soliton as shown in figure 2.4. This decay must conserve electric charge and, for the $Sp(2)$ theory $B-L$ charge. The different charge conservation considerations and the different relations between the energies for the two theories in Eq. 2.66 and 2.68, cause the landscape of stable dyonic states to be very different. Fig 2.8 and 2.9 show these regions of stability for the various relevant states in the two theories. These plots show some very interesting features. One can see that, while in $Sp(2)$ the only stable state at $\theta = 0$ is the monopole state $\mathcal{D}_{0,0}$, in $SO(2)$ there can be potentially 3 stable dyon states, $\mathcal{D}_{\pm 1}$ and $\mathcal{D}_0$,for sufficiently small coupling α and

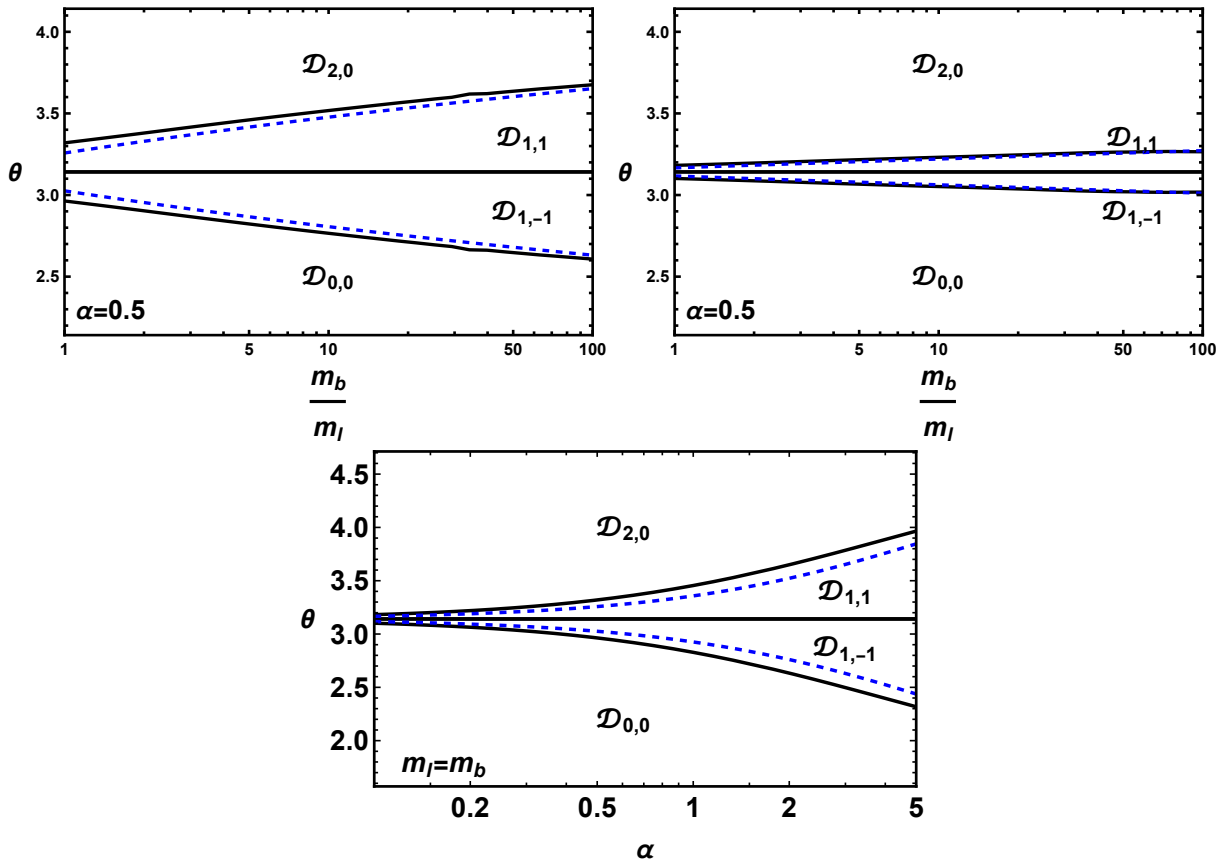

Figure 2.7: A plot of the regions of parameter space where the different dyon states are the ground state. The top two plots show the ground state as a function of θ and m_b/m_ℓ while the bottom plot shows the ground state for equal masses as a function of θ and α. The blue dashed lines represent the analytic approximation while the the solid black lines represent the numerical result.

mass ratio m_b/m_ℓ. This can be understood considering $B - L$ symmetry. As discussed, the boundary conditions in the $Sp(2)$ theory fix the amount of charge that must be held by each field. In particular, for $\mathcal{D}_{1,1}$ at $\theta = 0$, all of the electric charge $e/2$ is carried by the lepton. But a lepton state with charge $e/2$ must be a soliton, and so this state cannot possibly be stable. The same argument cannot be made in the $SO(2)$ theory, where no such symmetry forces the entirety of the charge into one field. There the two fields split the charge between themselves and thus, share the energetic burden.

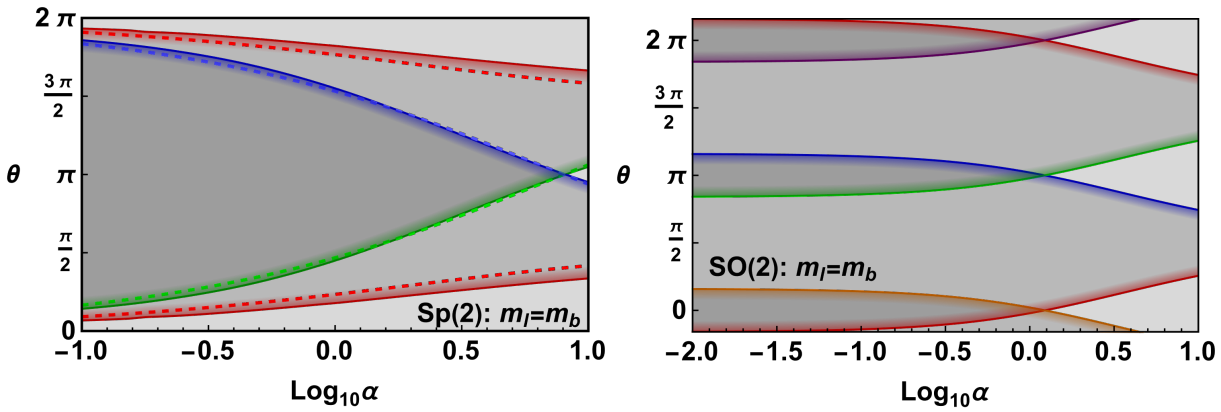

Figure 2.8: A plot of the various stable dyon states as a function of θ and α for the two theories with $m_b = m_\ell$, with the $Sp(2)$ theory on the left and the $SO(2)$ theory on the right. In both plots, the darkness of the gray shading represents the number of stable states with the lightest shading being 1 stable state (the ground state, and the darkest being 4 stable states. The different colors represent the stability regions of different states with blue corresponding to $q = 0$, red corresponding to $q = 1$ (this corresponds to the two degenerate states with $n_{B-L} = \pm 1$ in the right hand plot), green indicating $q = 2$ and for the $SO(2)$ plot the orange and purple correspond to the $q = -1$, and $q = 3$ states respectively. The colored shading around each line indicates the region where the state is stable. The dashed lines on the $Sp(2)$ plot indicate the results from the analytic approximation for the energies.

2.5.3 Observable θ angle for massless fermions

We conclude our discussion of the $N_f = 2$ case with a particularly interesting result of our investigation. It is a well know result in field theory that the θ parameter becomes unphysical if there is at least one massless charged fermion. The proof is very simple: via the chiral anomaly, the θ term in the Lagrangian can be removed through a chiral rotation on that massless fermion. This then leaves the Lagrangian independent of θ and thus, θ must be unphysical in the presence of massless charged fermions.

However, our investigation reveals that not all physical effects of θ vanish, even if one of the fermions is massless. To see this, consider the $\mathcal{D}_{0,0}$ state of the $Sp(2)$ theory in the limit where $m_\ell \to 0$. From the energy plots in Fig. 2.6, one can already see a physical consequence.

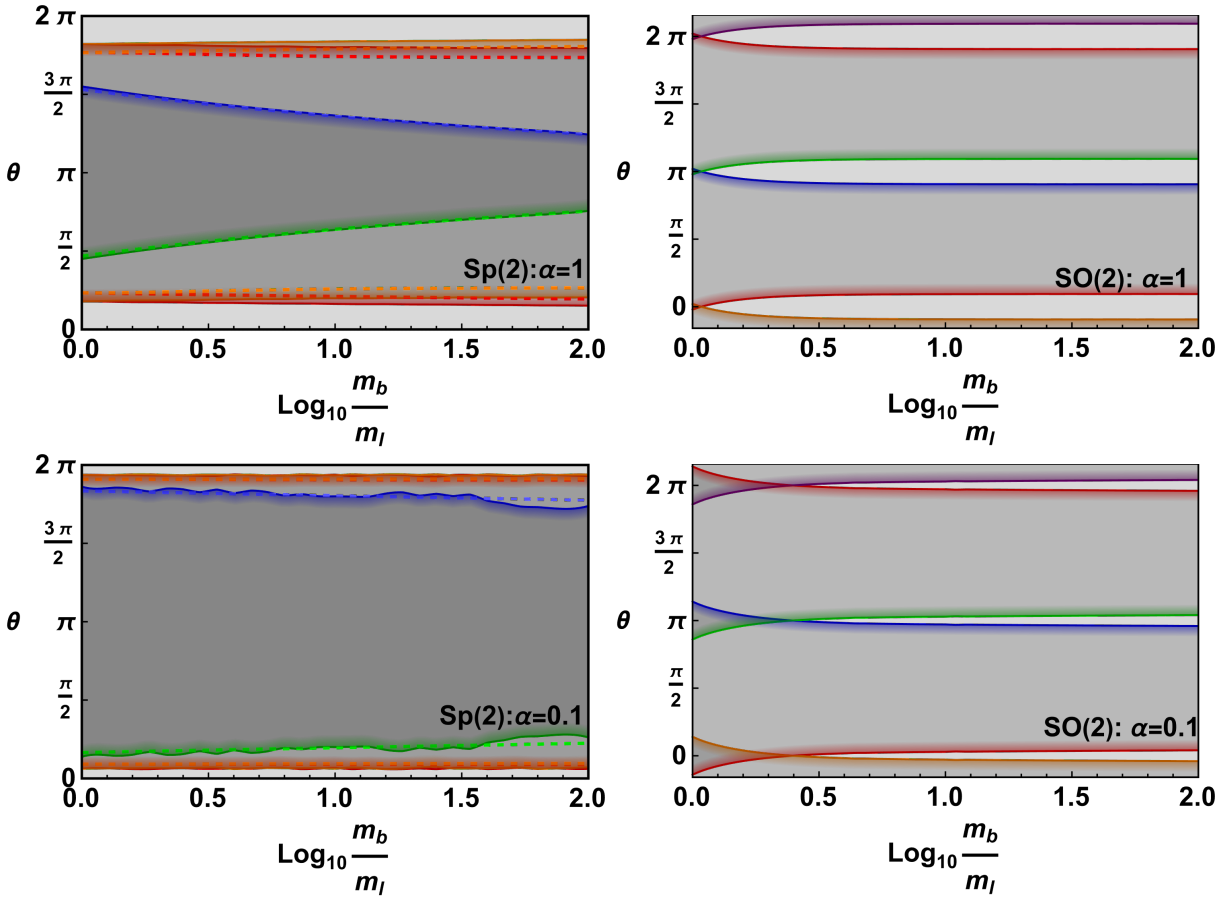

Figure 2.9: A plot of the various stable dyon states as a function of θ and m_b/m_ℓ for $\alpha = 1$ and 0.1, with the $Sp(2)$ theory on the left and the $SO(2)$ theory on the right. The coloring scheme is the same as that in figure 2.8 only now with the red and orange lines differentiating between the stability of the $n_{B-L} = -1$ and $n_{B-L} = 1$ states respectively.

In the $Sp(2)$ theory, the energy of the $\mathcal{D}_{0,0}$ state is of order of m_b. Physically, this looks like a correction to the mass of the monopole which, in the $\alpha \to 0$ limit is given by Eq. 2.54 to be

$$\Delta M_{monopole} \approx m_b \sin^2\left(\frac{\theta}{4}\right) \tag{2.74}$$

which is non-zero and θ dependent as $m_l \to 0$!

Another physical effect comes from considering the charge density of the $\mathcal{D}_{0,0}$ state. The boundary conditions on the $Sp(2)$ theory require that the lepton and baryon in the $\mathcal{D}_{0,0}$ state both

hold equal electric charge, $-\theta/4\pi$. As can be seen from figure 2.10, the baryonic deposits its charge $-\theta/4\pi$ at a radius $r \sim 1/m_B$. The lepton reduces the electromagnetic energy by partially screening the baryon vacuum's charge. In the small α limit, this screening by the lepton is inefficient and the lepton is unable to screen the entire charge. At a radius $r \sim 1/m_L$, the lepton gives the Witten effect by depositing the necessary charge to bring its total charge to $-\theta/4\pi$. From Fig. 2.10, it is clear that vacua's θ dependence does not vanish in the $m_L = 0$ limit. Aside

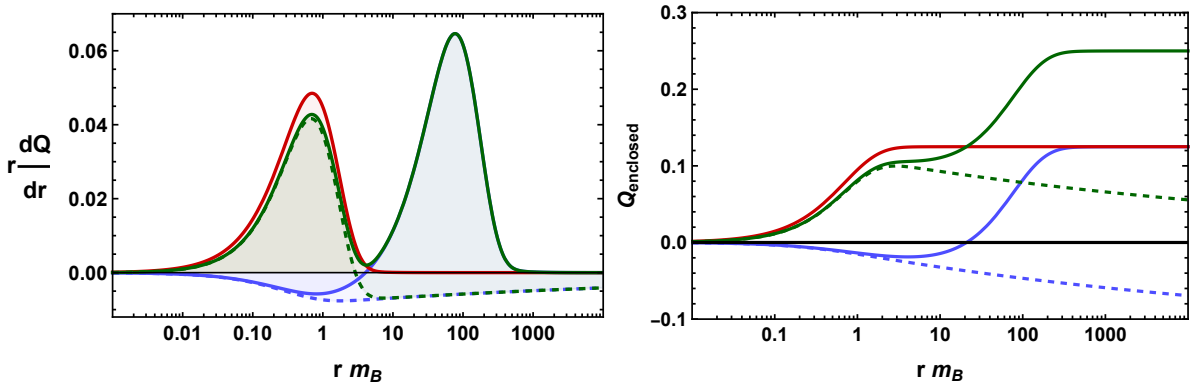

Figure 2.10: The plot on the left shows a picture of the baryon (red), lepton (blue), and total (green) differential charge densities as a function of log radius when $\theta = -\pi/2$ and $\alpha = 1$. In solid (dashed) lines, we have the charge density when $m_L = m_B/100$ ($m_L = 0$). The baryon and lepton vacuums each carry charge equal to $-\theta/4\pi$. The baryonic charge of $-\theta/4\pi$ is located roughly at distances $r \sim 1/m_B$. The lepton proceeds to screen the charge deposited by the baryon by depositing negative charge at distances $r \sim 1/m_B$, albeit in an extremely inefficient manner. At distances $r \sim 1/m_L$ the lepton then deposits a charge to bring its total charge to $-\theta/4\pi$. The plot on the right shows that is the same as the one on the right, but instead plotting the total charge enclosed as a function of radius.

from simply looking at the $m_L = 0$ lines on the plot, one can easily visually imagine the $m_L = 0$ limit by simply sitting at a finite radius and slowly letting the radius at which the extra charge in the leptonic vacuum is deposited approach infinity.

By considering the limit where when $\theta \neq 0$ and $m_L = 0$ one can see that, despite the total charge in the vacuum being zero, the charge density in the vacuum is non-vanishing. This can easily be seen in Fig. 2.10 where, in the $m_L = 0$ limit, the total charge enclosed at radius

r, $Q_{\rm enclosed}(r)$ (the green dashed line), is non-zero even for large r. At a radius $r \sim m_B^{-1}$, $Q_{\rm enclosed}$ is maximized. Afterwards, the enclosed charge falls off as $r^{\frac{1}{2}(1-\sqrt{1+\alpha/\pi})}$, as can be seen from the analytic solution in Eq. 2.47. This power law falloff can be extremely slow, falling as $r^{-\alpha/4\pi}$ for $\alpha \ll 1$ and so this charge can be spread out over extremely large distances on the order $\sim m_b^{-1} e^{4\pi/\alpha}$. The maximum enclosed charge, $Q_{\rm max}$, is proportional to θ and has a more

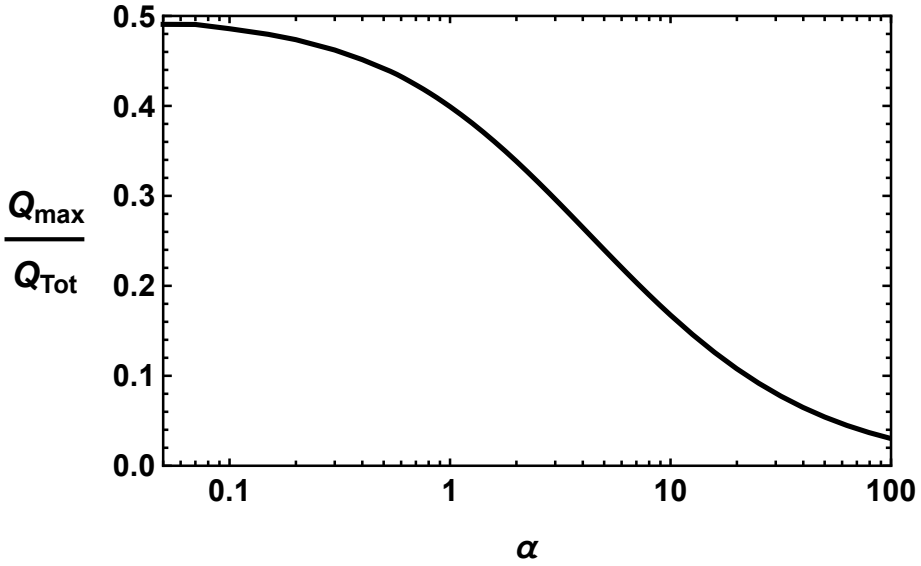

Figure 2.11: We take a monopole with $m_L = 0$ and calculate the largest the charge enclosed by a radius r gets, $Q_{\rm max}$. We plot $Q_{\rm max}$ versus α normalizing $Q_{\rm max}$ by the total charge of the monopole when $m_L \neq 0$, $Q_{\rm tot} = \theta/2\pi$. For large values of α, the enclosed charge is never large. For small values of α, it quickly asymptotes to the charge held by the baryons.

complicated dependence on α. We plot this dependence as a function of α in Fig. 2.11. When α is large, $Q_{\rm max}$ can be highly suppressed, while for $\alpha \sim 1/137$, the screening of the charge by the lepton is very inefficient and the maximal charge is approximately the charge held by the baryons $\theta/4\pi$.

All of these physical effects are possible because the chiral rotation that one would traditionally use to remove θ from the Lagrangian is only possible in the IR. In the UV, this chiral symmetry is broken to the re-emergence of the Yukawa terms in Eq. 2.4. This means that one cannot remove

the θ dependence from the Lagrangian in the UV. Normally this would be a minor caveat to the original argument, requiring the clarification that θ dependence should reemerge at the UV scale. However, from the Callan-Rubikov effect, these UV effects are able to manifest in the IR around a magnetic monopole.

2.6 $N_f \geq 4$

We now move on to consider $SO(N_f)$ and $Sp(N_f)$ theories for $N_f > 2$. Both theories consist of $N_f/2$ copies of the $N_f = 2$ theory and so we label the fields $\phi_{\ell,i}$ and $\phi_{b,i}$ for families $i = 1, 2, ..., N_f/2$. Symmetry considerations like the ones in Eq. 2.64 show that the states in the $SO(N_f)$ theory are indexed only by their charge quantum number and q while the $Sp(N_f)$ dyons are indexed by q, for electric charge, and $n_{B-L,i}$, for the i^{th} $B-L$-type charges of each family. We denote dyons in the $SO(N_f)$ theory as $\mathcal{D}_q$ and in the $Sp(N_f)$ theory as $\mathcal{D}_{q,\boldsymbol{n}_{B-L}}$ where $\boldsymbol{n}_{B-L} \in \mathbb{Z}^{N_f/2}$. The $Q^{tot}_{B-L,i}$ charge and an electric charge in each family $Q^{tot}_{EM,i}$, for any dyon is

$$\begin{aligned} Q^{tot}_{B-L,i} &= Q^{tot}_{b,i} - Q^{tot}_{\ell,i} \\ Q^{tot}_{EM,i} &= \frac{Q^{tot}_{b,i} + Q^{tot}_{\ell,i}}{2}. \end{aligned} \tag{2.75}$$

Note that neither theory has a condition that fixes the individual electric charge, $q^{tot}_{EM,i}$, in each family. The dyons are free to split up the electric charge between the families in any way to minimize the energy. Due to the large number of fields to keep track of, mapping out the entire landscape of stable states like we did for $N_f = 2$ is much more complicated. As such, we will not perform as thorough of analysis of all possible stable states. Instead, we will focus on two particular quantities, θ_c, the critical angle at which the $q = 0 (n_{B-L,i} = 0)$ state becomes unstable,

and N_{st}, the number of stable states at $\theta = 0$. We will do this for both theories in the limits of equal masses and the limit where we have two classes of fermions with either a heavy mass M or a light mass m.

2.6.1 Equal Masses

Let us start by considering the case where all fermions have equal mass. First let us consider finding θ_c, the angle at which the $q = 0$ ($\boldsymbol{n}_{B-L,i} = 0$) state becomes unstable. To start we will need to find the energy of the $q = 0$ state, which we will call E_0 for both theories, and the energy of the most favorable state to decay into, E_{out}. θ_c can then be defined as

$$E_0(\alpha, \theta_c) - E_{out}(\alpha, \theta_c) - m = 0. \tag{2.76}$$

Due to the symmetry between all fields, the total electric charge must be evenly distributed between the N_f fields in the $q = 0$ state, and thus $\phi_1 = \phi_2 = ... = \phi_{N_f}$. Since all the fields are identical, the Hamiltonian reduces to $N_f/2$ copies of the $N_f = 2$, with slightly modified values for θ and α.

$$H = \frac{N_f}{2}\int_0^\infty dr \frac{\phi_b'^2}{2} + \frac{\phi_\ell'^2}{2} + \left(\frac{\pi m(r)}{2}\right)^2 (2 - \cos(\phi_b)) - \cos(\phi_\ell)) + \frac{\alpha N_f/2}{4\pi r^2}\left(\phi_\ell + \phi_b - \frac{4\theta}{N_f}\right)^2 \tag{2.77}$$

The energy of the $q = 0$ state can be directly related to the energy of $q = 0$ in an $N_f = 2$ theory with effective coupling $\alpha_{eff} = \alpha N_f/2$ and effective $\theta_{eff} = 2\theta/N_f$.

$$E_0^{N_f}(\alpha, \theta) = \frac{N_f}{2} E_{0,0}^{N_f=2}(\alpha N_f/2, 2\theta/N_f) \tag{2.78}$$

This is true in both $SO(N_f)$ and $Sp(N_f)$ theories where we have suppressed the $\boldsymbol{n}_{B-L} = 0$ index for $Sp(N_f)$.

Next, we find the most favorable state for the $q = 0$ state to decay into. For the $SO(N_f)$ theory, this will naturally be the $q = 1$ states and we use relation analogous to like those in Eq. 2.65 to relate the energy of the $q = 1$ dyon to that of $q = 0$ in a theory with $\theta \to \theta + \pi$.

$$E_1^{N_f}(\alpha, \theta) = E_0^{N_f}(\alpha, \theta + \pi) = \frac{N_f}{2} E_{0,0}(\alpha N_f/2, 2(\theta + \pi)/N_f) \tag{2.79}$$

This and Eq. 2.78, can be used using the numerical energies we computed for $N_f = 2$ to find θ_c which is shown in Figure 2.12. We also perform a fit to a power law for $N_f \gg 1$, $\alpha N_f/2 \ll 1$ to which we find θ_c appears to scale linearly with N_f.

The situation in the $Sp(N_f)$ theory is a bit more complicated. To see why, consider the $\mathcal{D}_{1,(1,0,\ldots,0)}$ state. This carries electric charge $Q_{EM} = 1/2 - \theta/2\pi$, and $B - L$-type charges $Q_{B-L,1} = 1$, and $Q_{B-L,i>1} = 0$. From the symmetry between the $i > 1$ families, we know that they must share equal electric charge. However, because of the asymmetry between the $i = 1$ family and the other, there is no reason to suppose that the charge in the $i = 1$ is equal to the charge in the other families. The energy for this state can be found by generalizing Eq. 2.71 to

arbitrary N_f.

$$E^{N_f}_{1,1}(\alpha,\theta) = m\sin^2\left(\frac{\pi}{2}(Q^{tot}_{EM,1}+1/2)\right) + m\sin^2\left(\frac{\pi}{2}(Q^{tot}_{EM,1}-1/2)\right) + \\ + (N_f-2)\sin^2\left(\frac{\pi}{2}\frac{Q^{tot}_{EM}-Q^{tot}_{EM,1}}{(N_f-2)}\right) + m\frac{\alpha}{2}\left(\frac{1}{2}-\frac{\theta}{2\pi}\right)^2 \tag{2.80}$$

$Q^{tot}_{EM,1}$ is a free parameter and so we find it by minimizing the energy. We can see that this is minimized by $Q^{tot}_{EM,1} = Q^{tot}_{EM}$. But if $|Q_{EM}| > 1/2$, it is not difficult to show from Eq. 2.75 that either $|Q_{B,1}|$ or $|Q_{L,1}|$ will be greater than 1 and so the state is unstable! Therefore a decay into this state is only possible if $0 < \theta < 2\pi$. If $\mathcal{D}_{1,1}$ is unstable, then the $\mathcal{D}_{0,0}$ state must decay directly into the $\mathcal{D}_{2,0}$ state through the emission of two solitons, the energy of which can be related to the energy of the $\mathcal{D}_{0,0}(\theta+2\pi)$ state.

$$E^{N_f}_{2,0}(\alpha,\theta) = mN_f\sin^2\left(\frac{\pi}{N_f}\left(1-\frac{\theta}{2\pi}\right)\right) + m\frac{\alpha}{2}\left(1-\frac{\theta}{2\pi}\right)^2 \tag{2.81}$$

All of this means that, to find θ_c for the $Sp(N_f)$ theory one must solve

$$E_{0,0}(\alpha,\theta_c) = E_{out}(\alpha,\theta_c) \quad \text{where} \quad E_{out}(\alpha,\theta_c) = \begin{cases} E^{N_f}_{1,1}(\alpha,\theta_c) - m & \text{if} \quad 0 < \theta_c < 2\pi \\ E^{N_f}_{2,0}(\alpha,\theta_c) - 2m & \text{if} \quad \theta_c \geq 2\pi \end{cases}. \tag{2.82}$$

We can also get an analytic expression for the $E_{0,0}$.

$$E_{0,0}(\alpha,\theta) = mN_f\sin^2\left(\frac{\theta}{2N_f}\right) + m\frac{\alpha}{2}\left(\frac{\theta}{2\pi}\right)^2 \tag{2.83}$$

which can be used to solve for θ_c we can solve this analytic expression in the $N_f \gg 1$ $\alpha \ll 1$ limit

to find $\theta_c = N_f \sin^{-1}(2/\pi) \approx 0.69 N_f$. This approximation and the exact solution are shown in figure 2.12. Now we turn to the question of asking how many stable states are there at $\theta = 0$.

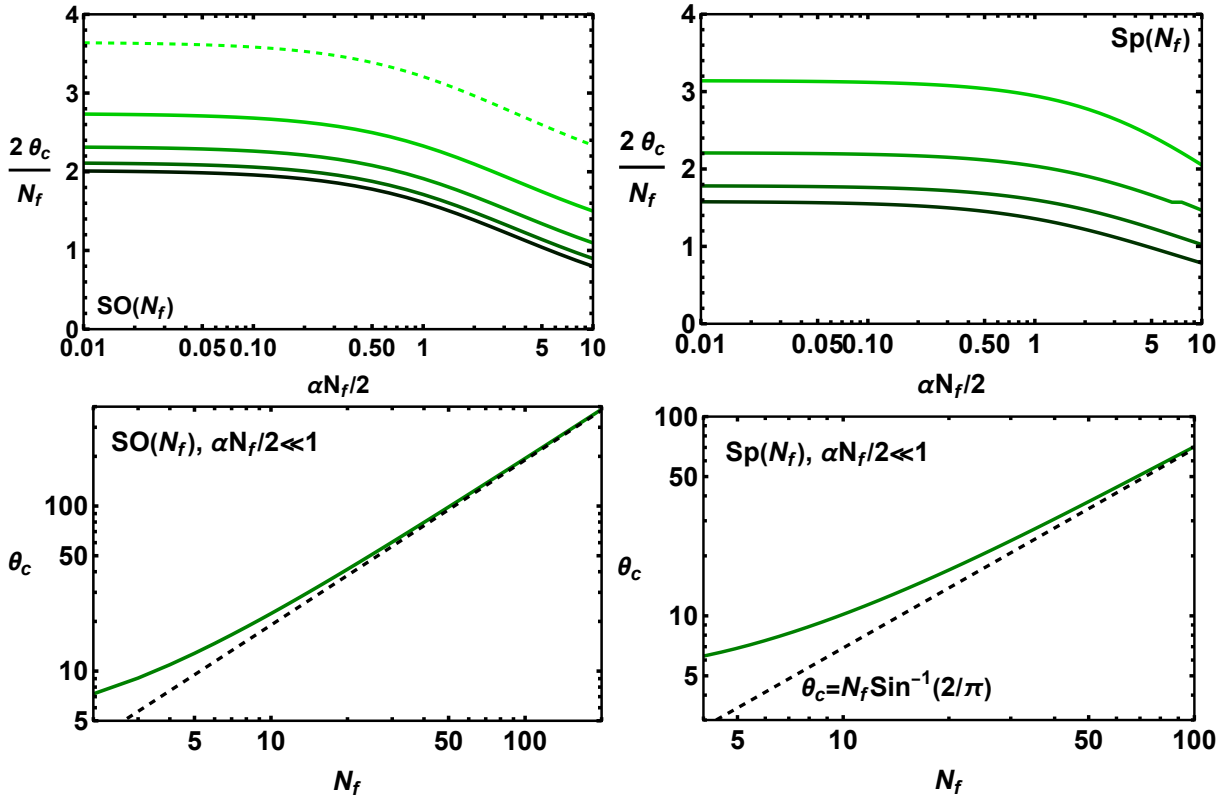

Figure 2.12: The top two plots show a plot of $2\theta_c/N_f$ as a function of $\alpha N_f/2$ for the two theories. We show the results for $N_f = 4, 8, 16$, and 32 with the darkest solid green line indicating $N_f = 32$, the lightest solid green line indicating $N_f = 4$ with darker green indicating larger N_f. The bottom two plots show θ_c as a function of N_f in the limit $\alpha N_f \ll 1$. Notice that for the $SO(N_f)$ theory $\theta_c \approx 1.9 N_f$ while for the $Sp(N_f)$ theory, $\theta_c \approx \sin^{-1}(2/\pi) N_f$ at large N_f.

At first this seems difficult to answer, especially in the $Sp(N_f)$ theory where there are a large number of states due to the $B - L$ charges. However, consider Eq. 2.81, which shows that the energy for the $q = 1$, $|\boldsymbol{n}_{B-L}| = 1$ state has energy $E \geq m$. The $q = 0$ state trivially has energy 0 at $\theta = 0$ so this state can never be stable. This easily extends to any state that is charged under any of the $B - L$ symmetries and we conclude that no stable $B - L$ charged state can exist at $\theta = 0$.

This then reduces the problem to finding stable electrically charged states at $\theta = 0$. But this

information and be easily extracted from θ_c using the field redefinition's in Eq. 2.65 and 2.67. By definition of θ_c and suppressing the $\boldsymbol{n}_{B-L}$ index on the dyon,

$$D_0(\theta) \quad \text{is stable if} \quad |\theta| < \theta_c. \tag{2.84}$$

We can take $\theta = -\pi q$ for some integer q (an even integer for $Sp(N_f)$ and use 2.65 or 2.67 to rewrite this as the statement

$$SO(N_f): \quad D_q(0) \quad \text{is stable if} \quad |q| < \frac{\theta_c}{\pi} \tag{2.85}$$

$$Sp(N_f): \quad D_q(0) \quad \text{is stable if} \quad |q/2| < \frac{\theta_c}{2\pi}. \tag{2.86}$$

By counting the number of states satisfying these conditions, we can conclude

$$SO(N_f): \quad N_{st} = 1 + 2\left\lfloor \frac{\theta_c}{\pi} \right\rfloor \to \frac{3.8 N_f}{\pi} \quad \text{if} \quad N_f \gg 1,\ \alpha N_f/2 \ll 1 \tag{2.87}$$

$$Sp(N_f): \quad N_{st} = 1 + 2\left\lfloor \frac{\theta_c}{2\pi} \right\rfloor \to \frac{N_f}{\pi} \sin^{-1}(2/\pi) \quad \text{if} \quad N_f \gg 1,\ \alpha N_f/2 \ll 1.$$

2.6.2 Mass Heirarchies

Now let us discuss the same scenarios where there is some number n of light fermions with mass m and some number of heavy fields $N_f - n$ with mass M

Based on our intuition from section 2.5, it is quite easy to extend the above analysis to this case for $SO(N_f)$. In the $SO(N_f)$ theories, the boundary conditions do not place any restrictions on the amount of electric charge that needs to be in any particular field (only on the sum of all the charges). As we saw in section 2.5, the system prefers to give charge to lighter fields since

it costs less energy to excite them. Thus, in the limit $M \gg m$, the system will give no charge to the heavy fermions and split it all among the light fermions. This effectively leaves us with a $N_f \to n$ theory of equal mass fermions and so all of the above results are valid for these hierarchical theories with the replacement $N_f \to n$.

Extending to arbitrary numbers of heavy and light fermions for $SP(N_f)$ is not trivial since the physics will depend on exactly how the heavy and light fermions are paired into the $N_f/2$ families. To keep the discussion relatively simple let us only consider the case of either one heavy fermion or one light fermion.

One Heavy Fermion

If we have only one heavy fermion, then it will cost energy to give a charge to this fermion and the system will prefer to not excite it. This essentially removes this fermion pair from the system and so all of the above results translate with $N_f \to N_f - 2$.

One Heavy Light Fermion

If we have only one light fermion, then the system will always prefer to give as much charge as possible to this light fermion and none to the heavy fermions. However, the boundary conditions require that if charge is given to the light fermion then charge must also be given to their heavy partner. However, there is no requirement from the boundary conditions to give charge to the other fermions and so they remain unexcited. This effectively reduces the system to and $Sp(2)$ theory as long as one does not wish to consider monopoles with $B - L$ charge in the heavy families.

2.7 Implications on GUTs and the Standard Model

Now we will briefly comment on the implications these results may have on the minimal $SU(5)$ monopole. The minimal $SU(5)$ monopole can be understood as a monopole resulting from the spontaneous breaking of an $SU(2)$ subgroup of $SU(5)$. The bosonized picture surrounding an $SU(5)$ monopole has been derived several times [8, 83, 84] so we will simply summarize the results below.

The fundamental monopole of $SU(5)$ is a monopole under the $SU(2)$ subgroup

$$\boldsymbol{T} = \frac{1}{2}\begin{pmatrix} 0 & & & & \\ & 0 & & & \\ & & & \boldsymbol{\sigma} & \\ & & & & \\ & & & & 0 \end{pmatrix}, \tag{2.88}$$

where the top left 3x3 matrix is the color subgroup and the bottom right 2x2 matrix is electroweak. As expected $SU(3) \times SU(2) \times U(1)/\mathbb{Z}_6$ are intertwined under this choice of $SU(2)$ subgroup. Under this spontaneously broken $SU(2)$, the 10 and $\overline{5}$ decompose into

$$\begin{pmatrix} e \\ d_3^c \end{pmatrix} \qquad \begin{pmatrix} d_3 \\ e^c \end{pmatrix} \qquad \begin{pmatrix} u_1^c \\ u_2 \end{pmatrix} \qquad \begin{pmatrix} u_2^c \\ u_1 \end{pmatrix} \tag{2.89}$$

where the subscripts are color indices. To proceed, we neglect off diagonal generators and

consider only the diagonal generators corresponding to

$$\lambda_3 = \frac{1}{2}\,\mathrm{diag}(1,-1,0,0,0) \tag{2.90}$$

$$\lambda' = \frac{1}{2\sqrt{2}}\,\mathrm{diag}(-1,-1,1,1,0) = \frac{1}{\sqrt{8}}Q_{EM} - \sqrt{\frac{2}{3}}\lambda_8 \tag{2.91}$$

$$\lambda_Z = \frac{1}{2\sqrt{10}}\,\mathrm{diag}(1,1,1,1,-4). \tag{2.92}$$

These generators were chosen such that they are orthogonal to the $SU(2)$ so that charges of these groups do not undergo the Witten effect. The Z boson obtains a mass and is neglected, though including it will not change anything that we discuss. The remaining diagonal generators can be integrated out. After bosonization, the remaining part of the gauge sector is

$$\mathcal{L}_{\text{gauge}} = -\frac{g^2}{128\pi^3 r^2}\left[(\phi_{u_1}+\phi_{u_2}-\phi_{d_3}-\phi_e-2\theta_5)^2 + (\phi_{u_1}-\phi_{u_2})^2 + \frac{1}{2}(\phi_e-\phi_{d_3})^2\right], \tag{2.93}$$

where θ_5 is the $SU(5)$ θ parameter. Aside from this, there are mass terms and kinetic terms for these sine-Gordon solitons. The boundary conditions at the origin are

$$\partial_r\phi_{u_1} = -\partial_r\phi_{u_2} \qquad \phi_{u_1} = \phi_{u_2} \quad \text{mod} \quad 4\pi \tag{2.94}$$

$$\partial_r\phi_{d_3} = -\partial_r\phi_e \qquad \phi_{d_3} = \phi_e \quad \text{mod} \quad 4\pi. \tag{2.95}$$

We are going to take the field $\phi_{e,d_3,u_1,u_2} \to 0$ as $r \to \infty$. At this level, the $SU(5)$ monopole is simply our $Sp(4)$ theory with some extra gauged $U(1)$s.

In what follows we will mostly limit ourselves to qualitative discussions of the properties of the $SU(5)$ monopole/dyon. Any quantitative discussion is necessarily suspect because of several

issues. When deriving Eq. 2.93, all off diagonal gauge bosons as well as the Z boson were all neglected. Additionally, the $SU(5)$ monopole involves the Higgs boson and thus has additional structure (that was ignored) on scales smaller than the Higgs mass. Finally, confinement is an extremely important low energy feature that cannot be captured by this analysis. Let us now discuss a few interesting results.

Massless down quark solution to the Strong CP problem

If the down quark were massless, it would solve the strong CP problem. However as we found in section 2.5, physical effects θ_5 can persist even if the down quark is massless. Observables such as the charge density and mass of the monopole would have θ_5 dependence. On the other hand, if both the down quark and electron (or just the up quark) were massless, then θ_5 could be completely shifted away and would be unphysical.

Stable electron-proton dyons

We next ask whether or not there is a stable proton-electron monopole dyon state. Of course, due to confinement, we cannot say anything for certain. There is reason to suspect both that this bound state exists and that it does not exist.

If $m_u = m_d = m_e > 1$ GeV, then we could consider the results for the $Sp(4)$ theory in Sec. 2.6 with equal mass. From figure 2.12, we can see that since $\theta_c < 2\pi$ for $N_f = 4$ no bound state exists for $\theta = 0$. We see similar results if m_e is much smaller than the others where our theory reduces to $N_f = 2$, we find there is also no bound state. However, this is only considering $\theta_5 = 0$. If $\theta_5 \neq 0$ there could easily be stable states as can be seen from figure 2.9.

Effects of θ_{EM}

While the QCD θ_{QCD} angle is consistent with zero experimentally, it is possible that θ_{EM} is non-zero and large. A situation such as this can arise, if both the $SU(5)$ θ_5 angle and phases in

the masses were 0, and we added a new vector-like multiplet in the fundamental representation. If the mass term for the charge 1 part (E) had a phase, while the mass term for the colored piece (D) was real, then this would induce a non-zero $\theta_{\rm EM}$ but keep $\theta_{\rm QCD} = 0$ after it were integrated out.

The effects of a non-zero $\theta_{\rm EM}$ are interesting as there is no solution unless D and E are explicitly included in the Lagrangian! To see this, let us rewrite Eq. 2.93 when $\theta_5 = 0$

$$\begin{aligned}\mathcal{L}_{\rm gauge} &= -\frac{g^2}{32\pi^3 r^2}\Big[\frac{3}{8}\left(\frac{2}{3}\phi_{u_1}+\frac{2}{3}\phi_{u_2}-\frac{1}{3}\phi_{d_3}-\phi_e\right)^2+\left(\frac{1}{2}\phi_{u_1}-\frac{1}{2}\phi_{u_2}\right)^2 \\ &+ \left(\frac{1}{2\sqrt{3}}\phi_{u_1}+\frac{1}{2\sqrt{3}}\phi_{u_2}-\frac{1}{\sqrt{3}}\phi_{d_3}\right)^2\Big], \end{aligned} \tag{2.96}$$

where the first term comes from EM, and the remaining terms come from $\lambda_{3,8}$ of QCD. Let us discuss things in terms of the color singlet proton-like state ($\phi_{u_1} = \phi_{u_2} = \phi_{d_3} \equiv \phi_p$) and the electron. This sub-system has nice properties such as the boundary conditions $\partial_r\phi_p = \partial_r\phi_e = 0$ and $\phi_p = \phi_e$, as well as leaving only the electromagnetic piece of Eq. 2.96 non-zero

$$\mathcal{L} = -\frac{3}{256\pi^3 r^2}\left(\phi_p - \phi_e - \theta_{\rm EM}\right)^2, \tag{2.97}$$

where we have now included the θ term for EM. Finite energy forces $\phi_p = \phi_e + \theta_{\rm EM}$ at small radii while the boundary conditions force $\phi_p = \phi_e$. Clearly, finite energy and the boundary conditions are inconsistent.

The resolution to this apparent paradox is to examine what happens at the scale where E is

integrated out. Including this new particle, changes

$$\mathcal{L} = -\frac{3}{256\pi^3 r^2}\left(\phi_p - \phi_e - \phi_E\right)^2 - m_E^2 \cos\left(\phi_E - \theta_{\rm EM}\right). \tag{2.98}$$

At the scale $r \sim 1/m_E$, E deposits a charge $\theta_{\rm EM}$ that is subsequently screened by the proton and electron. In this manner, the boundary condition effectively changes from $\phi_p = \phi_e$ to $\phi_p = \phi_e - \theta_{\rm EM}$. At a scale $r \sim 1/m_p$, the proton deposits charge $\theta_{\rm EM}/2$ while the electron attempts to screen it by depositing charge $-\theta_{\rm EM}/2$. Finally, the electron deposits charge $\sim \theta_{\rm EM}$ at a radius $r \sim 1/m_e$. The resulting system has $B-L$ charge 0 and dynamics happening on the length scales $1/m_E, 1/m_p$ and $1/m_e$ [1]. All of this structure results in the surprising fact that the dependence of the monopole mass on $\theta_{\rm EM}$ will be dominantly be driven by m_E, namely undiscovered UV physics, as opposed to any of the observed lighter particles.

Velocity dependence of the Callan Rubakov effect

Of great phenomenological interest is the rate at which baryons turn into electrons. When thrown in at low energies, chirality violation due to the mass term is the dominant effect and $B-L$ violation is suppressed. At high energies, the boundary conditions are the dominant effect and $B-L$ violation occurs. There is a critical velocity at which $B-L$ violation goes from exponentially unlikely to saturating unitarity. We now briefly estimate this velocity, see Ref. [84] for related work.

In the low energy limit, the monopole is described by protons and electrons with the electromagnetic term shown in Eq. 2.97 and the boundary conditions $\partial_r \phi_p = \partial_r \phi_e = 0$ and $\phi_p = \phi_e$. We will take $\theta_{\rm EM} = 0$ in order to simplify the discussion. We have numerically

[1] Due to the other generations, there will also be effects on length scales of order their inverse mass as well.

solved the e.o.m. with Eq. 2.97 by sending in solitons corresponding to protons and determined the critical velocity at which the outgoing particle is a positron. While we were not able to numerically solve for realistic values of $\alpha = 1/137$, we were able to find the scaling

$$v_c \approx 0.2\sqrt{\alpha}. \tag{2.99}$$

To obtain this numerical result, we took the electron to be massless and varied α between 0.1 and 5. We fit the scaling of v_c and obtained Eq. 2.99. Extrapolated to $\alpha = 1/137$, we find that

$$v_c \approx 2 \times 10^{-2}. \tag{2.100}$$

For velocities faster than this value, we expect proton conversion to electrons by $SU(5)$ monopoles to be unsuppressed, while we expect conversion to be exponentially suppressed for velocities smaller than this.

We can make a rough estimate to understand the α scaling of the critical velocity. Let us imagine that a baryon is incoming on the monopole with velocity v. Eventually at a critical radius R_c, the electromagnetic energy of a spherical charged shell is equal to its original kinetic energy ($\alpha/(8\pi R_c) \sim m_p v^2/2$) and the soliton bounces back. If at this critical radius, the electron and proton are both effectively massless ($R_c < 1/m_p < 1/m_e$), then the reflection of the baryon is similar to the massless limit and $B - L$ is violated. Otherwise, chirality violation from the mass term is more important and no $B - L$ violation occurs. Solving for the critical velocity when this turnover occurs, we find $v_c \sim \sqrt{\alpha/(4\pi)}$, which is closer to the numerical value, Eq. 2.100, than it has any right to be.

Finally, we note that Eq. 2.100 should be taken with a grain of salt. As emphasized in the previous paragraph, conversion finally occurs when $R_c \sim 1/m_p$. Unfortunately, at distances $\sim 1/m_p$ confinement becomes important and our EFT treatment of the proton breaks down. We expect that a proper treatment would only change Eq. 2.100 at the $\mathcal{O}(1)$ level. The lack of conversion at smaller velocities still lies in the realm of validity of our EFT approach.

Chapter 3: CMB Spectral Distortions from an Axion-Dark Photon-Photon Interaction

3.1 CMB Spectral Distortions

Let us begin this chapter by describing how our interaction in Eq. 1.3, gives rise to CMB spectral distortions. The effect of this interaction, in the presence of dark matter, is to convert photons into a dark sector particle, X. For example, if the axion constitutes the dark matter, photons will interact with the axions and convert them into dark photons so that X is the dark photon. Conversely, if the dark photon is dark matter, the photon will convert into axions and, in this case, X is the axion. In order to speak generally about either axion or dark photon dark matter, we will refer to the particle the photon converts to as X. The implications for the CMB spectral distortion are the same in either scenario since the important effect is that the photons convert to an invisible dark sector particle X and are removed from the photon spectrum.

The removal of any photons from the bath can lead to a deviation from the blackbody spectrum. We can quantify that change by a frequency dependent distortion $\delta(\omega)$ defined in Eq. 3.1.

$$f(\omega) = \frac{1}{e^{\omega/T} - 1} \rightarrow \frac{1}{e^{\omega/T} - 1} \left(1 - \delta(\omega)\right) \ . \tag{3.1}$$

The exact frequency dependence of the distortion will depend on when in cosmic history the photons were removed from the photon spectrum.

As shown in figure 3.1, we can define 5 different eras, the T era, the μ era, the $\mu - y$ transition era, the y era, and the free streaming era, in which the injection or removal of photons gives rise to different distortions. In the remaining of this section, we briefly review these different eras and discuss the characteristic effect of photon removal in each. As we will discuss, the final distortion to the blackbody spectrum can be parameterized by the impacts coming from different eras as

$$\delta_{\text{Tot}}(\omega) = (\bar{\mu} + \bar{\mu}_t)M(\omega/T) + (y + y_t)Y(\omega/T) + \delta_{Doppler}(\omega) + \delta_{\text{Free}}(\omega). \tag{3.2}$$

We see there are 4 different types of distortions. The μ and y distortions have distinct shapes and are insensitive to the details of the model generating the distortion, while $\delta_{Doppler}$ and δ_{free} have a model dependent shape. The contribution of all the pre-recombination distortions are computed using the Green's function method described in Ref. [85], using the rate at which photons are converted into particle X, $\Gamma_{\gamma\to X}(\omega)$, as discussed in Sec. 3.3 and appendix B.4.2. In computing this rate, we will need to calculate is the conversion probability $P_{\gamma\to X}(\omega)$. We also show that the distortion due to the post-recombination free streaming era distortion is directly related the the conversation probability $P_{\gamma\to X}(\omega)$. Thus, the central quantity we will need to compute all spectral distortions is the conversion probability.

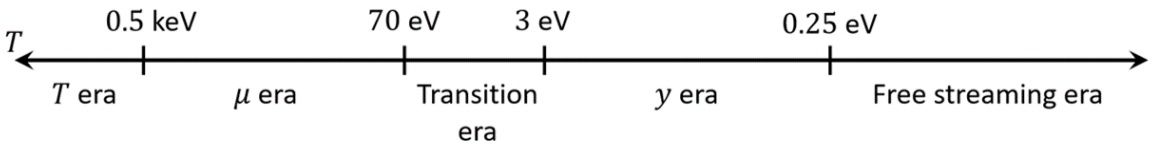

Figure 3.1: A timeline of the types of relevant distortion eras. The timeline is presented with time described by decreasing temperature T.

3.1.1 T Era

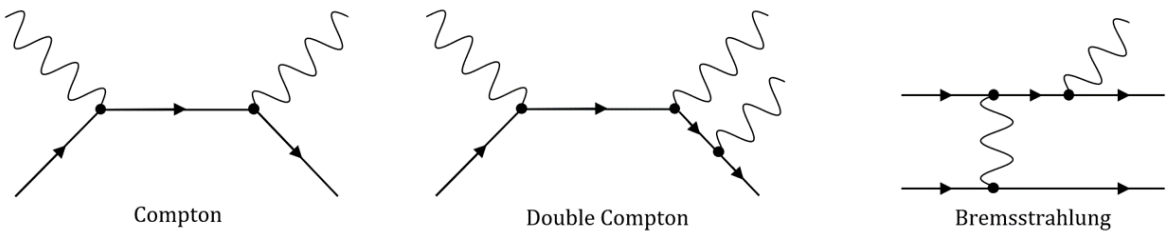

Figure 3.2: A sample diagram for each of the processes holding photons in equilibrium with the electrons.

In the very early universe, at temperatures $T \gtrsim 0.5$ keV (redshifts $z \gtrsim 2 \cdot 10^6$), a number of scattering processes involving photons are very efficient at driving the photon distribution towards an equilibrium distribution with zero chemical potential. The main processes, shown in figure 3.2, are Compton scattering, which can quickly redistribute the photon energy and equilibrate the electron and photon temperatures, as well as number changing processes, such as double Compton and bremsstrahlung. Due to these processes, in this era, even if photons are lost due to conversion into X, the distribution would be quickly driven back to that of a blackbody and the only effect would be a small change in the blackbody temperature. Since we don't know a priori the temperature of the CMB, injections in this era would not lead to a bound from the CMB spectrum (there could be bounds by studying the anisotropies or comparing to Big Bang Nucleosynthesis predictions which we will not explore in this work).

3.1.2 μ Era

Once the universe has cooled past $T \approx 0.5$ keV ($z \approx 2 \cdot 10^6$), the higher order processes like double Compton scattering and bremmstrahlung are no longer efficient at setting the chemical potential to zero (although they can still be efficient for absorbing/emitting very low frequency

photons). In this era, Compton scattering is still efficient at redistributing the energy, which drives the spectrum towards an equilibrium distribution. Because photon number is now conserved, any removal of energy will result in a small effective chemical potential term $\bar{\mu}$

$$f(\omega) = \frac{1}{e^{\omega/T} - 1} \rightarrow \frac{1}{e^{\omega/T + \bar{\mu}} - 1} \approx \frac{1}{e^{\omega/T} - 1} \left(1 - \bar{\mu}\, M(\omega/T)\right). \tag{3.3}$$

This distortion has a fixed shape, $M(\omega/T)$, given in appendix B.4.2. The size of this distortion is captured by the effective chemical potential, $\bar{\mu}$, which can be calculated from $\Gamma_{\gamma \rightarrow X}$, the rate at which photons are being converted to dark sector particles X as shown in appendix B.4.2. COBE-FIRAS placed a bound of $|\bar{\mu}| < 9 \cdot 10^{-5}$ [49].

3.1.3 y Era

At temperatures lower than 3 eV ($z \approx 10^4$), Compton scattering is still efficient enough to trap photons, but is now inefficient at changing photon energy, and transferring energy between photons and electrons. This leads to two effects. Firstly, some small amount of energy can be still exchanged with the electrons, leading to a difference in the photon and electron temperatures. Subsequent scatterings of photons with an electron fluid at a different temperature, lead to a y-distortion via the Sunyaev-Zeldovich (SZ) effect [86]. Secondly, energy injections/removals in a given frequency, can still be smeared due to Doppler broadening via Compton scattering, even if the process is no longer efficient at thermalizing the spectrum. This leads to two separate distortions: a y-distortion and a Doppler smeared distortion,

$$f(\omega) = \frac{1}{e^{\omega/T} - 1} \rightarrow \frac{1}{e^{\omega/T} - 1} \left(1 - yY(\omega/T) - \delta_{Doppler}(\omega)\right). \tag{3.4}$$

The y-distortion has a fixed shape, $Y(\omega/T)$, given in appendix B.4.2 and a size determined by the small parameter y which can be computed from the photon loss rate $\Gamma_{\gamma\to X}$ as described in appendix B.4.1. COBE-FIRAS placed a constraint $|y| < 1.5 \cdot 10^{-5}$ [49]. On the other hand, the shape of the Doppler smeared distortion is model dependent, so we instead place a bound by comparing directly to the COBE-FIRAS data.

3.1.4 $\mu - y$ Transition Era

Once the temperature decreases below $T \approx 70$ eV ($z \approx 3 \cdot 10^5$), Compton scattering, while still efficient at trapping photons, begins to become inefficient at redistributing energy for certain frequency modes of the photon spectrum. This signals the end of the μ era and the start of the $\mu-y$ transition era which lasts until $T \approx 3$ eV ($z \approx 10^4$). In this transition era, higher energy modes still redistribute energy efficiently through Compton scattering, while energy redistribution is inefficient for lower energy modes. At intermediate modes, energy redistribution is not efficient but is non-negligible. In order to exactly treat this frequency dependent behavior, one would need to simulate the distortion numerically [85]. However, as noted in Ref. [85], for the range of photon frequencies we are interested in, the distortion can be modeled to good accuracy as a pure energy injection as described in Ref. [87]. The resulting spectral distortion is a combination of a μ distortion $M(x)$ and a y distortion $Y(x)$ the shapes of which are given in appendix B.4.2.

$$f(\omega) = \frac{1}{e^{\omega/T} - 1} \to \frac{1}{e^{\omega/T} - 1} \left(1 - \bar{\mu}_t \, M(\omega/T) - y_t \, Y(\omega/T)\right). \tag{3.5}$$

The subscripts t on the coefficients $\bar{\mu}_t$ and y_t denote that these coefficients are calculated differently from $\bar{\mu}$ in Eq. 3.3 and y in Eq. 3.4. They still however are calculated from the photon conversion

rate $\Gamma_{\gamma\to X}$ as shown in appendix B.4.2.

3.1.5 Free Streaming Era

Around $T = 0.25$ eV ($z = 1100$), most electrons have been captured to form neutral hydrogen, and the universe becomes transparent to photons. From this point on, the photons become free streaming and can travel unimpeded across the universe, giving rise to the CMB we observe today. However, the presence of our interaction leads to a probability $P_{\gamma\to X}(\omega)$ that a CMB photon with frequency ω will convert to an invisible dark sector particle X before reaching us. Because the photons are free streaming, there is no thermalization, or redistribution of energy. So, the resulting spectrum is the original spectrum multiplied by the survival probability of a photon to reach us without converting to X,

$$f(\omega) = \frac{1}{e^{\omega/T} - 1} \to \frac{1}{e^{\omega/T} - 1} \left(1 - P_{\gamma\to X}(\omega)\right) . \tag{3.6}$$

We can see that the distortion is simply the conversion probability $P_{\gamma\to X}(\omega)$. The frequency dependence of this distortion is model dependent and as such we will have to compute it and then constrain it directly with the COBE-FIRAS data to obtain a bound.

3.2 Transition Probability

As described in the previous section, to compute the distortions we will need to compute the probability, $P(\omega, t, t_0)$, of converting photons of frequency ω produced at time t_0 into dark sector particles X at some later time t. Because our dark matter is made of bosons of mass $m \lesssim$ meV, the number density is large enough to treat dark matter as a classical background field.

Therefore, these probabilities can be computed using Feynman diagrams like the one shown in figure 3.3. In many instances the time interval $t - t_0$ will be of cosmic scale. For example, when

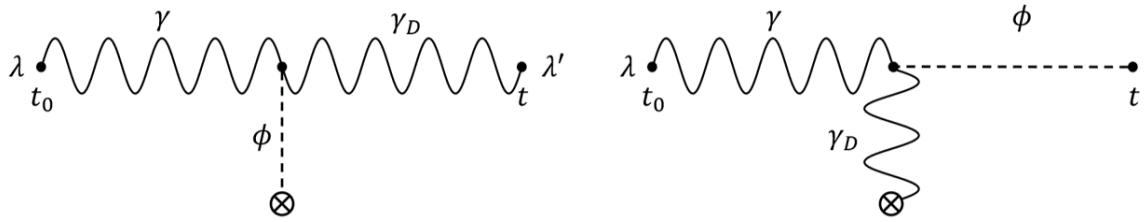

Figure 3.3: Diagrams for the probability of a photon produced at time t_0 to have converted to a dark photon or axion by a time t. The vertex indicates the interaction with the background dark matter field. λ and λ' represent the polarizations of the relevant particles.

applied to the free streaming distortion, $t - t_0$ will be the time between recombination and the present. As a consequence, we will need to compute these Feynman diagrams in a curved FRW background. We will work in conformal coordinates, described by the metric

$$d\tau^2 = a^2(\eta)\left(d\eta^2 - d\boldsymbol{x}^2\right) . \tag{3.7}$$

In a slowly expanding universe ($m_{DM}, T_{CMB} \gg H$), we can easily expand any general scalar field ϕ and vector field A_μ in terms of ladder operators by solving their equations of motion using the WKB approximation. The details of this process are given in appendix B.2.1 and the result is

$$\phi(x) = \int \frac{d^3\boldsymbol{k}}{(2\pi)^3 a(\eta)\sqrt{2\omega^c(\eta)}}\left(a_{\boldsymbol{k}} e^{-i\left(\int^\eta d\tilde{\eta}\omega^c(\eta,\boldsymbol{k}) - \boldsymbol{k}\cdot\boldsymbol{x}\right)} + h.c.\right) \tag{3.8}$$

$$A_\mu(x) = \int \frac{d^3\boldsymbol{k}}{(2\pi)^3\sqrt{2\omega^c(\eta)}} \sum_{\lambda=1,2,L}\left(a^\lambda_{\boldsymbol{k}}\epsilon^\lambda_\mu(\boldsymbol{k}) e^{-i\left(\int^\eta d\tilde{\eta}\omega^c(\eta,\boldsymbol{k}) - \boldsymbol{k}\cdot\boldsymbol{x}\right)} + h.c.\right), \tag{3.9}$$

where $a_{\boldsymbol{k}}$ ($a^\lambda_{\boldsymbol{k}}$) are the ladder operators of the scalar(vector) field, $\omega^c(\eta,\boldsymbol{k}) \equiv \sqrt{|\boldsymbol{k}|^2 + a^2(\eta)m^2}$ is the conformal energy, and the polarizations $\epsilon^\lambda_\mu(\boldsymbol{k})$ are given in Eq. B.13.

We will also need to include plasma effects on the photon due to its impact on photon propagation and mixing. At all times of relevance, electrons are non-relativistic and lead to a plasma frequency, $\omega_p(\eta)$, given by

$$\omega_p^2(\eta) = \frac{4\pi\alpha_e}{m_e} n_e(\eta)\,, \tag{3.10}$$

where α_e is the fine structure constant and $n_e(\eta)$ is the number density of electrons which changes as the universe expands. We are working in the limit where $\omega_p(\eta)$ is much smaller than the frequency of the CMB photons $\omega \sim T_{CMB}$. In this limit, the effects of the plasma can be reduced to the photons acquiring a small mass $m_\gamma(\eta) = \omega_p(\eta) \ll T_{CMB}$. Despite the plasma frequency giving rise to an effective mass for transverse modes, at such large frequencies there are no longitudinal modes of the photon (plasmons) [88]. We use the redshift dependent plasma frequency from [50].

Due to the non-trivial time dependence of the fields given in Eq. 3.8 and Eq. 3.9, we will only Fourier transform the diagrams in space. In this regime, our diagrams are transition amplitudes with a time dependent interaction and so we can expand our amplitudes to leading order using a Dyson series,

$$\langle X, \boldsymbol{k}'|U(\eta,\eta_0)|\gamma,\boldsymbol{k}'\rangle \approx -i\int_{\eta_0}^{\eta} d\eta'\,\langle X,\boldsymbol{k}'|V_I(\eta')|\gamma,\boldsymbol{k}'\rangle\,, \tag{3.11}$$

$V_I(\eta')$ is our interaction potential given by

$$V_I(\eta') = -\int d^3\boldsymbol{x}\,\mathcal{L}_{int} = -\int d^3\boldsymbol{x}\,\frac{\phi}{2f_a}F_{\mu\nu}\tilde{F}_D^{\mu\nu}. \tag{3.12}$$

Note the momentum eigenstates in Eq. 3.11 are normalized such that $\langle \boldsymbol{k}'|\boldsymbol{k}\rangle = (2\pi)^3\delta(\boldsymbol{k}-\boldsymbol{k}')$ which differs from the usual Lorentz invariant normalization by a factor of 2ω.

We can simplify $V_I(\eta')$ by using the fact that our dark matter field is nonrelativistic to ignore gradients in favor of time derivatives which simplifies the interaction to

$$\begin{aligned} \text{Axion DM:} \quad V_I^{\phi}(\eta') &= \int d^3\boldsymbol{x}\, \frac{\partial_\eta \phi}{f_a} \boldsymbol{A}_D \cdot \boldsymbol{B} \\ \text{Dark Photon DM:} \quad V_I^{D}(\eta') &= -\int d^3\boldsymbol{x}\, \frac{\phi}{f_a} \partial_\eta \boldsymbol{A}_D \cdot \boldsymbol{B}. \end{aligned} \tag{3.13}$$

Next we insert the expansion of the fields for the photon's magnetic field $\boldsymbol{B}$ (Eq. 3.9) and the outgoing particle field X (either Eq. 3.9 for an outgoing dark photon or Eq. 3.8 for an outgoing axion) in terms of creation and annihilation operators. As discussed earlier, we will treat the dark matter as a classical background field. These potentials can be inserted in Eq. 3.11 to compute the transition probability. After some simplifications described in appendix B.2.1, this probability takes the form,

$$P(\boldsymbol{k}, t_0, t) = \frac{1}{2}\sum_{\lambda} \left| \mathcal{A}^{\lambda}(\boldsymbol{k}, t, t_0) \right|^2 \quad \text{where} \quad \mathcal{A}^{\lambda}(\boldsymbol{k}, t, t_0) = \int_{t_0}^{t} dt'\, \mathcal{M}^{\lambda}(t', \boldsymbol{k})\,, \tag{3.14}$$

with

$$\mathcal{M}^{\lambda}_{\gamma\to\gamma_D}(t', \boldsymbol{k}) = \frac{\dot{\phi}(t', \tilde{\boldsymbol{x}}(t'))\sqrt{v_D(\boldsymbol{k}, t')}}{2f_a} e^{i\int^{t'} d\tilde{t}\left(\omega_D(\tilde{t}) - \omega_\gamma(\tilde{t})\right)} \tag{3.15}$$

$$\mathcal{M}^{\lambda}_{\gamma\to\phi}(t', \boldsymbol{k}) = \frac{\dot{\boldsymbol{A}}_D(t', \tilde{\boldsymbol{x}}(t')) \cdot \boldsymbol{\epsilon}_\lambda(\boldsymbol{k})\sqrt{v_\phi(\boldsymbol{k}, t')}}{2a(t')f_a} e^{i\int^{t'} d\tilde{t}\left(\omega_\phi(t) - \omega_\gamma(t)\right)}\,, \tag{3.16}$$

where the first (second) equation corresponds to the axion (dark photon) dark matter scenario. In the above equations, $\tilde{\boldsymbol{x}}(t')$ is the position of the photon at time t', the dots represent time derivatives with respect to comoving time t, and $v(\boldsymbol{k}, t)$ represents the velocity of a given particle.

We have approximated $v_\gamma = 1$. The ω's are now the physical energies defined as:

$$\omega(\boldsymbol{k}, t, m) = \sqrt{\frac{|\boldsymbol{k}|^2}{a^2(t)} + m^2} \tag{3.17}$$

Finally, we must determine what form our dark matter background takes. By solving the equations of motion for the dark matter fields (Eq. B.10 and Eq. B.11) in the non-relativistic limit, keeping terms up to $\mathcal{O}(v_{DM})$, and demanding that the energy density is $\rho^0_{DM}/a^3(t)$, where ρ^0_{DM} is the energy density of dark matter of the universe at the present time, we find

$$\dot{\phi}_{DM}(\tilde{\boldsymbol{x}}, t) = \sqrt{\frac{2\rho^0_{DM}}{a^3(t)}} \cos(m_{DM} t + \beta(\tilde{\boldsymbol{x}})) \tag{3.18}$$

$$\dot{\boldsymbol{A}}_{DM}(\tilde{\boldsymbol{x}}, t) = \sqrt{\frac{2\rho^0_{DM}}{a(t)}} \boldsymbol{\epsilon}(\tilde{\boldsymbol{x}}) \cos(m_{DM} t + \beta(\tilde{\boldsymbol{x}})). \tag{3.19}$$

Both fields get a spatially dependent phase, $\beta(\tilde{\boldsymbol{x}})$, while the vector dark matter field gets an additional spatially dependent polarization unit vector $\boldsymbol{\epsilon}(\tilde{\boldsymbol{x}})$. Both of these quantities vary spatially on the scale of the dark matter de Broglie wavelength $(m_{DM} v_{DM})^{-1}$ with $v_{DM} \ll 1$. Additionally, they vary in time, on timescales $(m_{DM} v^2_{DM})^{-1}$. Since the time dependence is suppressed by a factor v_{DM} relative to the spatial dependence it will be ignored. In appendix B.2.3, we show that for all distortions, we average $\tilde{\boldsymbol{x}}$ over many de Broglie wavelengths of the dark matter field, which means that we can average all of these spatially dependent quantities. We will leave the averaging over the phase for later in the computation, but in appendix B.2.3 we show that we can effectively replace

$$\boldsymbol{\epsilon}_\lambda(\boldsymbol{k}) \cdot \boldsymbol{\epsilon}(\tilde{\boldsymbol{x}}) \to \frac{1}{\sqrt{3}}. \tag{3.20}$$

Physically, this factor $\frac{1}{\sqrt{3}}$ reflects the fact that the interaction $\boldsymbol{\epsilon}_\lambda(\boldsymbol{k}) \cdot \dot{\boldsymbol{A}}_D$ in Eq. 3.16 is picking out one particular polarization of the vector dark matter. After averaging over $\tilde{\boldsymbol{x}}$, this particular polarization must make up $1/3$ of the total dark matter by isotropy, effectively sending $\rho^0_{DM} \to \rho^0_{DM}/3$. Using Eqs. 3.18-3.20 to simplify Eqs. 3.14-3.16, we can write the transition probabilities as

$$\begin{aligned} P_{\gamma\to\gamma_D}(\boldsymbol{k}, t_0, t) &= \frac{\rho^0_{DM}}{2f_a^2} L^2(m_\phi, m_D, \boldsymbol{k}, t_0, t) \\ P_{\gamma\to\phi}(\boldsymbol{k}, t_0, t) &= \frac{\rho^0_{DM}}{6f_a^2} L^2(m_D, m_\phi, \boldsymbol{k}, t_0, t), \end{aligned} \tag{3.21}$$

where L is a length scale defined as

$$L^2(m_{DM}, m_X, \boldsymbol{k}, t_0, t) \equiv \left\langle \left| \int_{t_0}^{t} d\tilde{t}' \sqrt{\frac{v_X(t', |\boldsymbol{k}|)}{a^3(t')}} \cos(m_{DM} t' + \beta(t')) \;\; \times e^{i \int^{t'} d\tilde{t} \Delta\omega_{\gamma\to X}(\tilde{t}, \boldsymbol{k})} \right|^2 \right\rangle_\beta ,$$

where $\Delta\omega_{\gamma\to X}$ is the change in energy from a photon converting into particle X at momentum $\boldsymbol{k}$,

$$\Delta\omega_{\gamma\to X}(\tilde{t}, \boldsymbol{k}) = \omega_X(\tilde{t}, \boldsymbol{k}) - \omega_\gamma(\tilde{t}, \boldsymbol{k}) \,. \tag{3.22}$$

The $\langle\rangle_\beta$ indicates the remaining average over the dark matter phase $\beta(t') = \beta(\tilde{\boldsymbol{x}}(t'))$ which is handled for pre-recombination and free streaming distortions separately in appendix B.4.1 and B.3 respectively. From Eq. 3.21, we can see that the only difference between scalar dark matter and vector dark matter is the overall factor of $1/3$ in the conversion probability from the effect described above. This means that the coupling to dark photon matter is effectively $1/\sqrt{3}$ that of the coupling to axion dark matter and so the bounds placed on the coupling in the dark

photon dark matter will be weaker than the bounds for the axion dark matter by a factor $\sqrt{3}$. For simplicity, we will only consider axion dark matter going forward, knowing that we can translate any result to dark photon dark matter by multiplying by $1/\sqrt{3}$.

3.3 Computing the Distortions

In this section, we will use Eq. 3.21 to determine the strength of the distortions arising from the various eras. This will be very different for distortion generated pre-recombination versus in the free streaming regime, so we consider them separately.

3.3.1 Free Streaming Distortion

In Sec. 3.1.5, we showed that the free streaming distortion, δ_{free}, is equal to the probability of converting the photon to dark sector particle X between recombination, t_0 and today, t. Thus, we need to compute

$$\delta_{free}(|\boldsymbol{k}|) = \frac{\rho^0_{DM}}{2f_a^2} L^2(m_{DM}, m_X, \boldsymbol{k}, t_0, t)\,. \tag{3.23}$$

From Eq. 3.22, it is clear that we can write $L^2 = \left\langle \left| \frac{L_+ + L_-}{2} \right|^2 \right\rangle_\beta$, where

$$L_\pm = \int_{t_0}^{t} dt' \sqrt{\frac{v_X(t')}{a^3(t')}} e^{i\int^{t'} d\tilde{t}\,(\Delta\omega(\tilde{t}) \pm (m_{DM} - \dot{\beta}(\tilde{t}))}. \tag{3.24}$$

The remaining integral is an oscillatory integral with frequency

$$\Omega_\pm(t) \equiv \Delta\omega(t) \pm (m_{DM} - \dot{\beta}(t)). \tag{3.25}$$

Notice that all of the time-dependent quantities change on the Hubble scale $H(t)$ due to the expansion of the universe[1]

There are two limits in which this integral can be computed. The first is the fast oscillation limit where the oscillation frequency, $\Omega_{\pm}(t)$, is approximately constant over many oscillations. This is the limit where

$$\Omega_{\pm}(t) \gg H(t). \tag{3.26}$$

In this limit, all of the time-dependent quantities in Eq 3.24 become approximately constant up to corrections of order $H/\Omega_{\pm}$ and the integral can be computed analytically. The second limit is the resonant limit. In this limit, there is a time (or possibly multiple times), t_r, where there is a stationary phase in the exponential ($\Omega_{\pm}(t_r) = 0$). Since $\dot{\beta}(t) \ll m_{DM}$ to a good approximation these resonant times can be found by solving the equation

$$\Delta\omega(t_r) \pm m_{DM} = 0. \tag{3.27}$$

Physically, this corresponds to times in which the dark matter particle being absorbed/emitted by the photon is on shell, leading to an enhancement in the conversion probability. The stationary phase approximation is used to compute the integral in this limit. Appendix B.3 contains the

[1]Strictly speaking, $\dot{\beta}(t)$ changes on the scale $m_{DM} v_{DM} \delta v_{DM} \sim m_{DM} v_{DM}^2$ where δv_{DM} is the size of the dark matter velocity dispersion. However, in the full computation, one can work in Fourier space and treat each mode of the dark matter field independently before summing over all modes at the end, effectively removing effects from the time dependence from $\dot{\beta}(t)$.

details of computing the distortions in both of these limits. In the end, we find,

$$\delta_{free}(|\boldsymbol{k}|) = \frac{\rho^0_{DM}}{4f_a^2}\frac{|L_+|^2+|L_-|^2}{2} \quad \text{where} \quad |L_\pm|^2 = \begin{cases} \frac{v_X(a_*)}{a_*^3|\Delta\omega(a_*)\pm m_{DM}|^2} & \text{no resonances} \\ \sum_{a_\pm} \frac{2\pi v_X(a_\pm)}{a_\pm^3|\partial_t\Delta\omega(a_\pm)|} & \text{resonances.} \end{cases} \tag{3.28}$$

Here, $a_\pm$ are all solutions to Eq. 3.27, and $a_* = (1090)^{-1}$ is the redshift at recombination. Notice that the resonant distortion is enhanced by a factor of $\frac{|\Delta\omega \pm m_{DM}|^2}{\partial_t \Delta\omega} \sim \frac{m_{DM}}{H}$ with respect to the non-resonant distortion. Even for the smallest possible dark matter masses, $m_{DM} \sim 10^{-20}$, this is an enhancement by a factor of $\mathcal{O}(10^8)$. Thus, we expect our bounds on the coupling $1/f_a$ to be enhanced by orders of magnitude in regions of parameter space where these resonances happen.

3.3.2 Pre-Recombination Distortions

The application of Eq. 3.21 to pre-recombination distortions is not as straightforward as for the free streaming distortions. The distortions can be computed via the Green's function method outlined in Ref. [85] where the distortion, $\delta(x)$ is given by

$$\delta(x) = \int dx' \int \frac{da}{aH(a)} G(x, x', a)\Gamma_{\gamma\to X}(x', a), \tag{3.29}$$

where x is the dimensionless frequency $x = \omega/T(a)$ and $\Gamma_{\gamma\to X}(x', a)$ is the rate at which photons of frequency $x'T$ are converted to dark sector particle X. The Green's function $G(x, x', a)$ describes how photons injected into mode x' at time when the scale factor is a are redistributed to mode x. $G(x, x', a)$ is given for the various eras in appendix B.4.2. In this section we will describe how to compute the rate $\Gamma_{\gamma\to X}(x', a)$ appearing in Eq. 3.29.

We can compute $\Gamma(a, \boldsymbol{k})$ from $P(\boldsymbol{k}, t_0, t)$ as follows. Consider a photon that scatters off of an electron at time t_0 and travels some time τ before scattering off of another electron. $P(\boldsymbol{k}, t_0, t_0 + \tau)$ is then the probability of the photon converting to X between these scatterings. For an ensemble of photons scattering with time τ between scatterings, the rate at which those photons are converted to X is then

$$\Gamma(t_0, \tau, \boldsymbol{k}) = \frac{P(\boldsymbol{k}, t_0, t_0 + \tau)}{\tau}. \tag{3.30}$$

Since the photon is traveling through a very dense medium of electrons, it has a certain probability $p(\tau)$ of traveling a distance τ characterized by its mean free path λ_γ, given by

$$p(\tau) = \frac{e^{-\tau/\lambda_\gamma}}{\lambda_\gamma}. \tag{3.31}$$

In order to find the average rate for all photons, we average $\Gamma(t_0, \tau, \boldsymbol{k})$ over this path length distribution

$$\Gamma(a(t_0), \boldsymbol{k}) = \int_0^\infty d\tau \, \frac{e^{-\tau/\lambda_\gamma}}{\lambda_\gamma} \frac{P(\boldsymbol{k}, t_0, t_0 + \tau)}{\tau}. \tag{3.32}$$

Because this era is before recombination, we have $H\lambda_\gamma \ll 1$. In this limit, we can treat space as static and all parameters that change due to the expansion of the universe as constant in the integral, and Eq. 3.32 can be computed analytically. The details are given in appendix B.4.1, and the end result is

$$\Gamma(a, |\boldsymbol{k}|) = \frac{\rho_{DM}^0 v_X(a, |\boldsymbol{k}|)}{4 f_a^2 a^3 \lambda_\gamma(a)} L_{eff}^2(a, |\boldsymbol{k}|), \tag{3.33}$$

where

$$L^2_{eff}(a,|\boldsymbol{k}|) = \frac{1}{2}\left\{\frac{\ln[1+\lambda^2_\gamma(a)(m_{DM}+\Delta\omega(a))^2]}{(m_{DM}+\Delta\omega(a))^2} + \frac{\ln[1+\lambda^2_\gamma(a)(m_{DM}-\Delta\omega(a))^2]}{(m_{DM}-\Delta\omega(a))^2}\right\}.$$

This rate can be plugged into Eq. 3.29 and integrated numerically using the Green's functions given in App B.4.2 find the distortion from the various pre-recombination eras.

3.4 Results

The total distortion for a given set of masses m_X and m_{DM} and coupling $1/f_a$ is given by Eq. 3.2. As described in Sec. 3.1, temperature shift distortions are undetectable by COBE-FIRAS. Therefore we should add an arbitrary temperature shift, $\mathcal{T}(x)$ (defined in App. B.4.2), to the distortion and do a best fit to COBE-FIRAS data [49] with both the coupling, $1/f_a$ and the size of the temperature shift, α, as free parameters.

$$\delta_{\text{Tot}}(\omega) = (\bar{\mu}+\bar{\mu}_t)M(\omega/T) + (y+y_t)Y(\omega/T) + \delta_{Doppler}(\omega) + \delta_{\text{Free}}(\omega) - \alpha\mathcal{T}(\omega/T). \quad (3.34)$$

However we can simplify this by demanding that the number density of CMB photons be the the same as that of a perfect blackbody at the measured temperature $T_{CMB} = 2.35 \cdot 10^{-4}$ eV. This is exactly the procedure that is commonly done for μ and y distortions as described in [89]. This constraint fixes the size of the temperature distortion α. For fixed m_D and m_ϕ, we do a χ^2 fit of our distortion to the COBE-FIRAS data with a single free parameter, $1/f_a$. By demanding that the distorted spectrum matches the measured spectrum to within 2σ, we obtain bounds for the coupling as a function of the dark photon and axion masses m_D and m_ϕ. Figure 3.4 shows a

contour plot of these bounds as a function of the axion and dark photon masses. We show contours for both axion dark matter and dark photon dark matter. These bounds are plotted against the leading best bound on this coupling from red giant cooling constraints. Ref. [24] shows that this coupling leads to a novel cooling mechanism in red giants due to plasmon decay and deduced that the cooling from this coupling is equivalent to the cooling from a neutrino magnetic dipole moment $\mu_\nu = \frac{1}{2f_a}$. Then using the bound placed on neutrino magnetic dipole moments found in [90] from red giant cooling they were able to place a bound $1/f_a < 7.1 \cdot 10^{-10}$ GeV on the axion-photon-dark photon coupling. As seen in figure 3.5, in a large portion of parameter space, roughly $m_X < 10^{-2}$ eV and $m_{DM} < 10^{-8}$ eV, our bounds beat this red giant bound by several orders of magnitude. It is worth noting that while the red giant bound is the most stringent bound in this region of parameter space (aside from the bounds placed in this work), there have been numerous other constraints placed on the coupling in this region of parameter space. The bounds placed on this coupling from stellar evolution [16], Horizontal Branch stars [22], and white dwarfs [23] are all with in an order of magnitude of those from red giants. For simplicity, we only include the red giant bound in our plots. Figure 3.5 shows our bounds as a function of the axion dark matter mass (m_{DM}) for selected values of the dark photon mass (m_X) and shows the contribution to these bounds from each distortion era. While the bounds in figure 3.5 are shown for axion dark matter, the equivalent bounds for dark photon dark matter can be found by scaling the bounds up by a factor of $\sqrt{3}$ as discussed at the end of section 3.2. As can be seen from the colored dashed lines in figure 3.5 each constraint from each distortion has roughly the same behavior: constant for small m_{DM} and increasing linearly in m_{DM} for large m_{DM} with an enhanced region in between. We can understand why the bounds have this behavior. Firstly, the enhanced region is the region of parameter space where photons during that particular era are

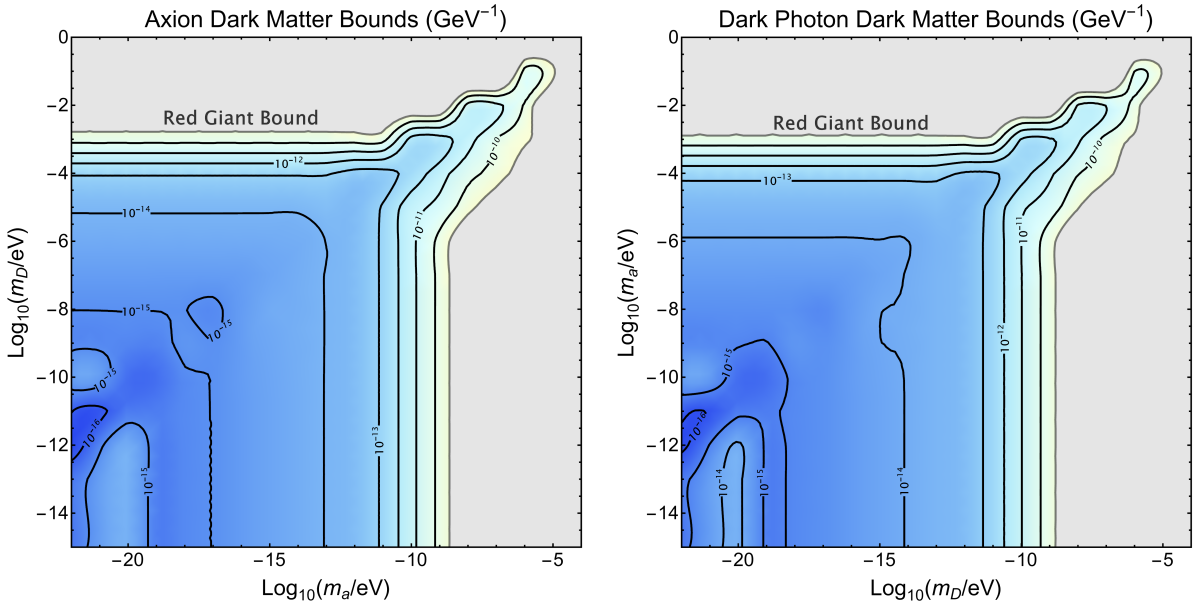

Figure 3.4: Bounds on the coupling $1/f_a$ (GeV^{-1}) plotted as a contour plot as a function of the dark photon mass (m_D) and the axion dark matter mass (m_a). The plot on the left shows the bounds for the axion dark matter case and the plot of the right shows the dark photon dark matter case. The grey region represents the region where the previous best bound on the coupling derived from red giant cooling [24] is stronger.

able to resonantly convert. The other two limits can be understood by considering the integral L^2 defined in Eq. 3.22 in the non-resonant regime. Here L^2, the effective oscillation length, is the square of an oscillatory integral and thus should scale as $L^2 \sim \Omega^{-2}$ where Ω is the fastest oscillation frequency in the integral. For sufficiently small m_{DM}, the coherent oscillation of dark matter is unimportant. As such, the oscillation length is the standard $\Delta\omega_{\gamma\to X}$ present for well known systems such as neutrino oscillations. For larger m_{DM}, the fast oscillation of dark matter dominates and the oscillation frequency is m_{DM}. This combined with Eq. 3.21, shows that the conversion probability $P_{\gamma\to X} \propto \frac{\rho_{DM}}{f_a^2 \Delta\omega^2}$ for small m_{DM} and $P_{\gamma\to X} \propto \frac{\rho_{DM}}{f_a^2 m_{DM}^2}$ for large m_{DM}. Since the distortions all scale with the conversion probability, its clear that the bounds at low m_{DM} are independent of m_{DM} and linearly proportional to m_{DM} for large m_{DM}.

Given that the COBE-FIRAS data was collected over 30 years ago, current technology

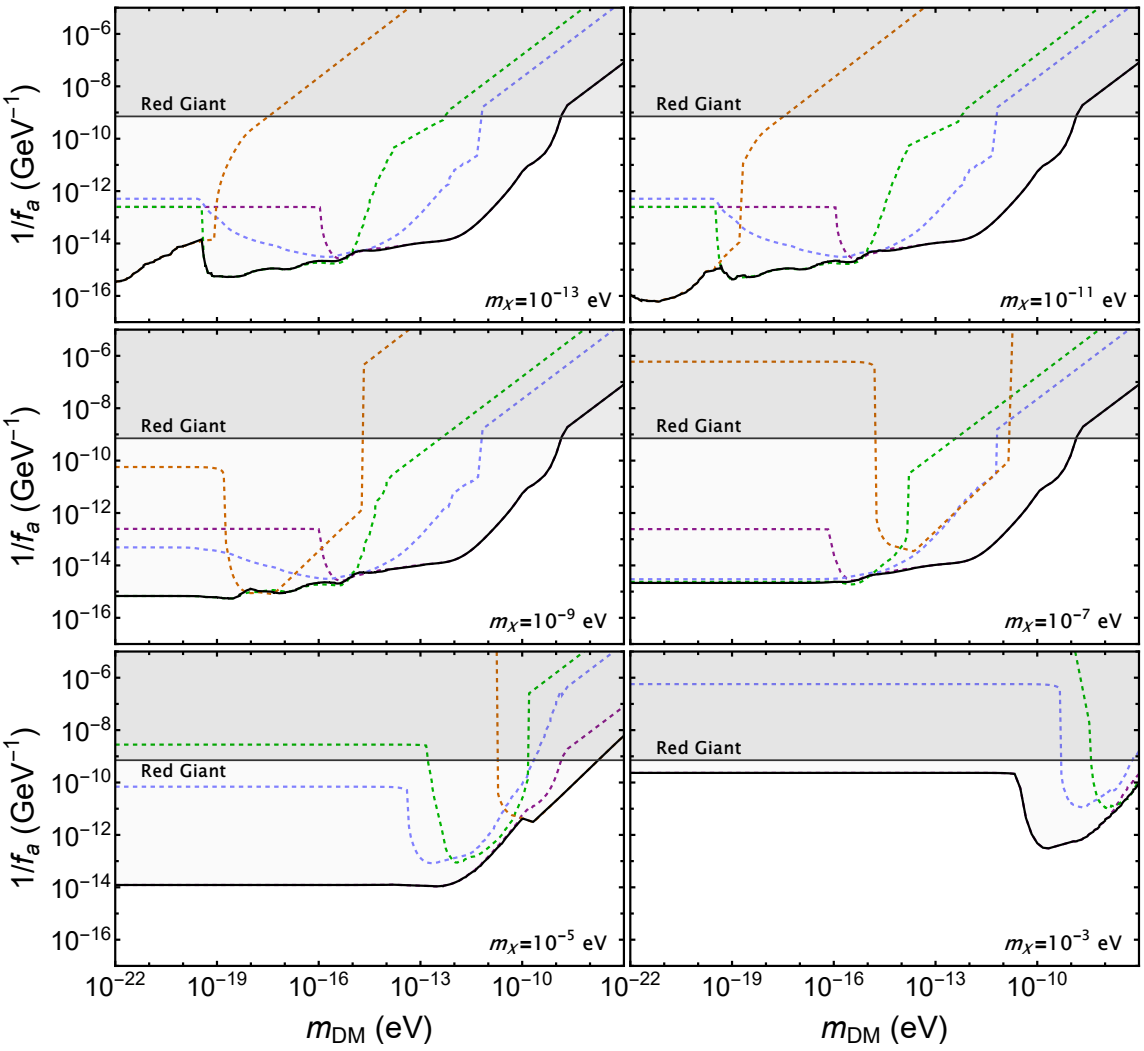

Figure 3.5: Bounds on the coupling $1/f_a$ as a function of the axion dark matter mass m_{DM} plotted for various values of the dark photon mass, m_X. The purple, blue, green and orange dashed lines are the individual μ, y, Doppler and free streaming bounds respectively while the solid black line is the total bound from all distortions. The grey line represents the current best bound on the coupling derived from red giant cooling [24]. The bounds shown here are for the axion dark matter case, but the bounds for the dark photon dark matter case can be obtained by scaling the bounds up by a factor of $\sqrt{3}$. The bounds for $m_X < 10^{-13}$ eV are exactly those given in the upper-left plot.

could measure the CMB spectrum to higher precision. In fact, there are proposals for experiments, like PIXIE [91], that aim to measure the spectrum to within a factor of $10^{-8}-10^{-9}$, an improvement of around a 3 to 4 orders of magnitude from COBE-FIRAS. These future experiments could

potentially measure a distortion in the CMB frequency spectrum and thus it is interesting to ask what such a measured distortion could tell us about our dark matter models.

Specifically, we will discuss qualitatively whether a distortion produced from our dark matter model(s) could potentially be distinguished from other distortion sources. Energy injection or removal into or from the background electron plasma before recombination produces primarily a μ and/or y distortion and thus these types of distortions which are essentially model independent. However, because of their non-thermal origin, the Doppler distortion arising pre-recombination, and free streaming distortion post-recombination have model dependent spectral shapes and do provide a distinctive signature. For simplicity, we can focus on the free streaming distortion to get a sense of the various types of shapes this distortion can take. To start, one can take the large and small m_{DM} limits ($m_{DM} \gg \Delta\omega$ and $m_{DM} \ll \Delta\omega$ respectively) of Eq. 3.28 and see that

$$\text{Small } m_{DM} \text{ limit:} \quad \delta \sim \omega^2 \qquad \text{Large } m_{DM} \text{ limit:} \quad \delta \sim \text{Constant.} \tag{3.35}$$

Figure 3.6 shows these quadratic and constant distortions plotted against the μ and y distortions. The amplitudes of these distortions in figure 3.6 are chosen so that each distortion disagrees with COBE-FIRAS at 2σ. In this sense we can think of these distortions as being of equal strength. We can see that the large m_{DM} matches very well with the μ-distortion and the small m_{DM} distortion, matches well with a y distortion making them difficult to distinguish from the generic μ and y distortions respectively. The shapes of the free streaming distortion get more interesting if we consider the resonant region of parameter space ($m_{DM} \sim \Delta\omega$). Here the distortion depends on the time of the resonance, $a_{\pm}$, which is found by solving Eq. 3.27. Because $\Delta\omega$ depends on the frequency of the photon, so does the resonant time through Eq. 3.27. Thus

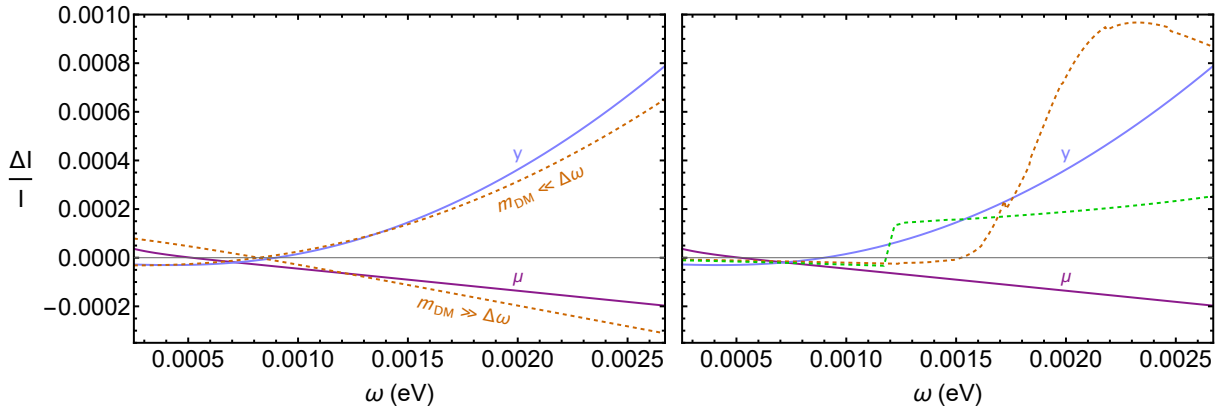

Figure 3.6: Shown here are shapes of the various types distortions $\delta(\omega) = \frac{I(\omega)-I_{Blackbody}(\omega)}{I_{Blackbody}(\omega)}$. Each distortion is plotted with an amplitude such that it disagrees with the COBE-FIRAS data at 2σ. Thus all the distortions are effectively the same strength. The purple and blue lines are μ and y distortions respectively while the dashed green and orange lines depict Doppler and free-streaming distortion shapes for different choices of masses m_{DM} and m_X. On the left, we show the distortions in the non-resonant limits given in Eq. 3.35. On the right, we show two of the many possible shapes the distortions can take when there is a resonance in either the Doppler or free distortions. These resonant distortions have shapes distinct from the μ and y distortions. It is also worth noting that the differences in shape between the Doppler and free distortion in the right-hand plot are due to the difference in choice of parameters, m_{DM} and m_X, rather than a difference in distortion type.

different frequency modes can have different resonance times which can lead to very distinctive frequency dependencies in the distortion easily distinguishable from the standard μ/y-distortion. In particular, it is possible that some frequency modes undergo resonance while other modes don't. This leads to especially unique distortions where some frequency modes are distorted while others, effectively, are not. Such extreme distortions are shown in the orange and green dashed lines in figure 3.6. As can be seen, lower frequency photons never resonate, and thus are effectively undistorted while higher frequencies do experience a distortion due to resonance. Additionally, the frequency dependence of the resonant piece of the distortion is not a simple power law of ω due to the dependence of the resonant time on the frequency and in turn the non-trivial dependence of the distortion on the resonant time. It is also important to note that

these qualitative features can also arise from the Doppler distortion. From Eq. 3.33 and 3.34 one can derive the same small and large m_{DM} behavior and show similar types of resonant behavior are possible. The green dashed line in figure 3.6 shows one such distinctive resonant shape for the Doppler distortion. This makes the prospect of observing these unique distortions even more likely since, as shown in figure 3.5, there are significant regions of parameter space where the Doppler distortion leads to the strongest bound, which shows that in such regions of parameter space it is the most observable effect. It is worth pointing out that the difference in shape and severity of the jumps of the Doppler and free distortions in figure 3.6 is not due to an inherent difference between the free and Doppler distortion, but rather a difference in the parameters m_{DM} and m_X at which these distortions are evaluated. These set of parameters were chosen to highlight the difference in distortion shapes achievable by either the free or Doppler distortions rather than an inherent difference between them.

Chapter 4: Supernova Constraints on an Axion-Photon-Dark Photon Interaction

4.1 The Energy Loss Argument and Emission Constraints

The core collapse supernova SN1987A has provided, and continues to provide, valuable constraints on new physics. Measurements of the energy emitted into neutrinos and the duration of the emission were used to infer the cooling rate of the supernova. This cooling rate was found to be consistent with Standard Model predictions. Any new particle weakly coupled to the Standard Model provides a new channel for energy loss in the supernova. This would increase the cooling rate, pushing it out of agreement with Standard Model predictions, and provides a constraint on the coupling of new light particles to the Standard Model. This constraint can be expressed in a simple form with the Raffelt criterion [63], which states that the luminosity of new particles, L_x, can be no larger than the luminosity of neutrinos, L_ν,

$$L_x \leq L_\nu = 3 \cdot 10^{52}\ \text{erg}\cdot\text{s}^{-1}\,. \tag{4.1}$$

Depending on how strongly the new particles interact, cooling can occur in two different regimes. If the new particles interact very weakly, after being produced they carry away energy without further interactions inside the proto-neutron star. This corresponds to the bulk emission regime and is used to place a lower bound on the coupling, dependent only on the amount of energy

going into the new particles. Once the interactions of the new particles are sufficiently strong, they become trapped in the proto-neutron star and the cooling is only done through emission at their last scattering surface (trapping surface), i.e. as in a blackbody. As the coupling becomes stronger, this trapping surface moves to larger radii and thus to lower temperatures, which results in a smaller luminosity. This leads to an upper bound on the couplings that can be excluded by Raffelt's criterion. In this section, we will examine the constraint arising from bulk emission and discuss the trapping constraint in Sec. 4.2.

In our model the axion and dark photon play the roles of these weakly interacting particles. To find the luminosity of axions and dark photons we must find the emissivity, $\dot{\epsilon}$, or energy emission rate per unit volume. Integrating this over the volume of the supernova gives the luminosity of the bulk emission,

$$L_{Bulk} = \int_{V_{SN}} d^3\boldsymbol{r}\ \dot{\epsilon}(r)\,.$$

Next, we must compute the emissivity for each process that can produce axions and dark photons in the supernova. To find these emissivites, we simply take the interaction rate per unit volume for that process and weigh it by the energy carried away by the axion and dark photon in the final state [72],

$$\dot{\epsilon} = \left(\prod_i \int \frac{d^3\boldsymbol{p}_i}{(2\pi)^3 2E_i} f_i(E_i)\right)\left(\prod_f \int \frac{d^3\boldsymbol{p}_f}{(2\pi)^3 2E_f}\right)\overline{|\mathcal{M}|^2}(E_a+E_D)(2\pi)^4\delta^4\left(\sum p_i - \sum p_f\right)\,. \tag{4.2}$$

Here, momenta indexed with i represent initial state particles while momenta indexed with f represent final state particles. The f_i's represent the thermal weights of the initial state particles.

The matrix element is averaged over initial spins and summed over final spins. E_a and E_D are the energies of the produced axion and dark photon. For computational ease, we neglect Pauli blocking and Bose enhancement of the final states. The latter is never a large effect on the processes under consideration, while the former can significantly reduce the rates for processes involving scattering with electrons at the core. As we will show later, those processes are subdominant even without taking Pauli blocking into account, and thus we will not include them when deriving constraints. When Eq. 4.2 is simplified for processes involving two initial state particles (A and B), the emissivity can be nicely written as the product of initial densities multiplied by a thermally averaged, energy weighted cross section

$$\dot{\epsilon}_{A+B\to\phi+\gamma_D+X} = n_A n_B \left\langle v_{mol}\sigma_E \right\rangle \ , \tag{4.3}$$

where σ_E is the ordinary cross section weighted by the sum of energies of the axion and dark photon. The brackets indicate an averaging over initial thermal states in the supernova and is defined by Eq. C.2 in appendix C.1. The integral over final states, $\int d\Pi_f$ is defined in appendix C.1 in Eq. C.1, while v_{mol} is the frame invariant Moller velocity, $v_{mol} = \sqrt{(\boldsymbol{v}_A - \boldsymbol{v}_B)^2 + (\boldsymbol{v}_A \times \boldsymbol{v}_B)^2}$.

A similar simplification can be done for the emissivity for any process with a single initial state particle (A). The result is a product of the initial densities and the average decay rate weighted by energy is

$$\dot{\epsilon}_{A\to\phi+\gamma_D} = n_A \left\langle \Gamma_{A\to\phi+\gamma_D} E_A \right\rangle , \tag{4.4}$$

where Γ is the usual decay rate.

There are 4 relevant processes for the production of axions and dark photons in supernova.

3 of them are collision processes involving 2 initial state particles: the annihilation of an electron and positron, Compton scattering of an electron and photon, and nuclear bremsstrahlung of a proton and neutron. An example diagram for each of these processes is shown in Fig. 4.1.

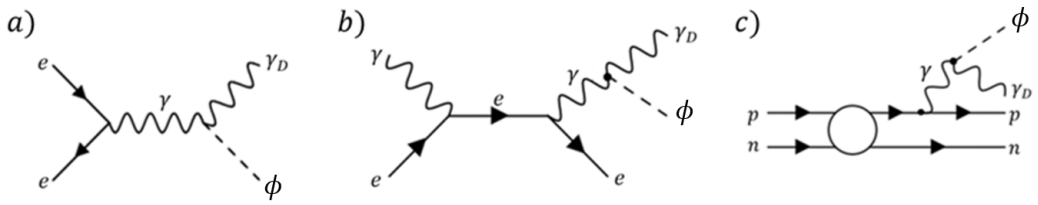

Figure 4.1: Representative figures for the 3 leading collision processes that produce axions and dark photons in a supernova. a) $e^+ + e^- \to \gamma_D + \phi$, the annihilation of an electron and positron. b) $e^+\gamma + \to e^+\gamma_D + \phi$, Compton scattering where the off-shell Standard Model photon decays to an axion and dark photon. c) $p + n \to p + n + \gamma_D + \phi$, nuclear bremsstrahlung where the off-shell photon decays to an axion and dark photon.

The emissivites for these processes are computed in appendix C.1 and the results are given in Eq. 4.5,

$$\begin{aligned}
\dot{\epsilon}_a &= \frac{\alpha_e}{24 f_a^2} n_{e^-} n_{e^+} \langle E_{tot} \rangle \, Q^a(m_a, m_D) \,, \\
\dot{\epsilon}_b &= \frac{\alpha_e T^3}{90\pi^3 f_a^2} n_p n_n \langle \Sigma_{pn} \rangle \, Q^b(m_a, m_D) \,, \\
\dot{\epsilon}_c &= \frac{\alpha_e^2}{48\pi f_a^2} n_{e^-} n_\gamma \langle E_{tot} \rangle \, Q^c(m_a, m_D) \,,
\end{aligned} \tag{4.5}$$

where $\langle E_{tot} \rangle$ is the average of the sum of the initial state particle's energies. The Q factors in each expression, defined in Eqs. C.12, C.26, C.36 in appendix C.1, contain all of the dependence on the masses of the axion and dark photon. They are normalized so that they are $\mathcal{O}(1)$ when $m_a = m_D = 0$ and then decrease as the axion or dark photon gain mass.

The annihilation and Compton emissivities have a simple structure. They include the couplings involved in the process, the initial densities, and the average of the total initial energy. The bremsstrahlung emissivity has a different structure due to how it was computed, which we do

following Ref. [73]. In order to deal with the nuclear scattering, which does not allow for a simple perturbative calculation in the energy regime of interest, we assume that the process is dominated by scatterings where the radiated particles (and hence the virtual photon in the diagram) have energies much smaller than the kinetic energy of the nucleons [1]. This approximation, called the soft radiation approximation, allows us to factorize the emissivity into two factors: one factor accounting for the nuclear scattering and another capturing the decay of a virtual photon into the axion and dark photon. The factor Σ_{pn} is the piece that accounts for the dynamics of the nuclear scattering and is proportional to the momentum transfer cross section of proton-neutron scattering. In detail, it is given by

$$\Sigma_{pn} = \frac{|\boldsymbol{p}_p|^2}{m_N^2} v_{mol} \sigma^{pn}_{\Delta \boldsymbol{p}} \quad \text{where} \quad \sigma^{pn}_{\Delta \boldsymbol{p}} = \int d\Omega (1 - \cos(\theta)) \frac{d\sigma_{pn}}{d\Omega}. \tag{4.6}$$

In order to compute the momentum transfer cross section we use experimental data from Ref. [71] and for more details see appendix C.1.

Now we consider the decay processes that could produce axions and dark photons. To leading order, there is only one such process: the decay of plasmons into dark photons and axions. The diagram of this process is shown in Fig. 4.2.

[1] Cooling is dominated by particles with energies comparable to the temperature at which they are produced, and thus there is a large uncertainty associated with this approximation. In Ref. [71] it is argued that for real photon emissions with energies comparable to the nucleon energies, this approximation is accurate to within a factor of 2.

Figure 4.2: The leading order decay process that can produce a dark photon and axion. A plasmon γ_p decays into an axion and a dark photon.

In order to compute the emissivity, we've used the polarizations and dispersion relations for the plasmon given in Ref. [88]. Again, the details of the computation are given in appendix C.1, but the result is

$$\dot{\epsilon}_p = \frac{\zeta(3)T^3}{3\pi f_a^2}\left(\frac{\omega_p^2}{4\pi}\right)^2 Q^p(m_a, m_D), \tag{4.7}$$

where Q^p defined in Eq. C.50 contains all of the dependence on the mass of the axion and dark photon. It is $\mathcal{O}(1)$ when $m_a = m_D = 0$ and decreases for increasing dark photon and axion masses. ω_p is the plasmon frequency defined in Eq. C.42.

Fig. 4.3 shows a plot of the emissivities for $m_a = m_D = 0$ as a function of supernova radius. These emissivities are computed using the temperature and density profiles given in appendix C.2. Near the center of the core, Compton scattering and plasmon decay dominate the energy emission while at larger radii, annihilation dominates. Note that the Compton emissivity does not take Pauli blocking into account, and thus the true rate would have a large suppression compared to what is shown in Fig. 4.3. We will not include the Compton contribution to the luminosity, which is a conservative approach. Since the Compton contribution to the total luminosity is subdominant, neglecting it only leads to a small effect. Upon integration of each emissivity over the volume of the supernova, we find that the annihilation is the dominant process, with plasmon decay being a significant contribution for lower masses.

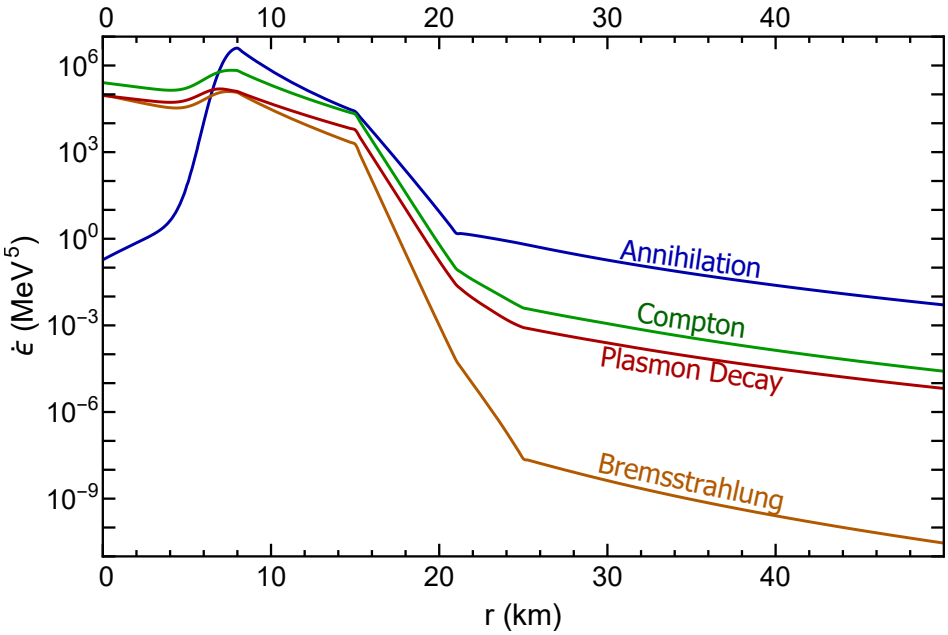

Figure 4.3: A plot of the emissivities of the various processes that produce axions and dark photons as a function of radius of the supernova. These emissivities are taken for both the dark photon and axion massless. The annihilation process is the dominant process everywhere in the supernova except for near the center of the supernova where it is suppressed by the low density of positrons. The coupling has been set to $f_a = 1$ MeV for convenience.

Finally, these emissivities are summed into a total emissivity and integrated over the volume of the supernova to give the total luminosity of axions and dark photons. This total luminosity is then applied to the constraint in Eq. 4.1 for various axion and dark photon masses and is shown in the lower line in Fig. 4.5.

4.2 Trapping Constraints

As discussed in Sec. 4.1, at stronger couplings cooling is done through surface emission due to particles becoming trapped. Using this surface emission, one can derive an upper bound on the couplings from the Raffelt criterion in Eq. 4.1. Once the coupling is large enough, any new particle, x, will be trapped inside the supernova below some radius r_x. This radius, r_x, is

defined as the point where the optical depth τ is equal to $2/3$

$$\frac{2}{3} = \tau(r_x). \tag{4.8}$$

The optical depth is defined as

$$\tau(r_x) = \int_{r_x}^{\infty} \frac{dr}{\lambda_x}, \tag{4.9}$$

where λ_x is the mean free path of the new particle and is related to the scattering process for the new particle x with Standard Model particles. Because of rapid absorption and re-emission, the emitted energy due to this new particle is no longer the bulk emission seen in Sec. 4.1 but can be approximated as blackbody radiation from this radius[2] r_x given by

$$L_{Blackbody}(r_x, m_x, g_{\star,x}) = 4\pi r_x^2 \left(\frac{g_{\star,x}\pi^2}{120}\right) T^4(r_x) h(m_x/T). \tag{4.10}$$

Here m_x is the mass of the particle and $g_{\star,x}$ is its number of degrees of freedom. This resembles the familiar expression for blackbody radiation with $\frac{g_{\star,x}\pi^2}{120}$ being the Stefan-Boltzmann constant in natural units and an additional factor $h(m_x/T)$. This factor is to account for the mass of the radiated particle and is defined by

$$h(z) = \frac{15}{\pi^4} \int_z^{\infty} dx \frac{x(x^2 - z^2)}{e^x - 1}. \tag{4.11}$$

[2]In general, there are separate radii at which number changing processes, energy exchange processes, and trapping freeze-out and this can be taken into account in order to improve the bound as discussed in Refs. [92, 93]. Here we take the simplified approach of considering the trapping radii, which is the largest of the three, as the blackbody since this leads to a smaller flux and hence a more conservative limit.

This integral is such that when the particle is massless, $h(0) = 1$ and we recover the familiar blackbody formula. In the limit $m_x \gg T$, $h \sim e^{-m_x/T}$ meaning that for very massive particles, blackbody radiation is highly suppressed.

The luminosity of this blackbody radiation has a different dependence on the coupling than the bulk emission considered in Sec. 4.1. Since for radii larger than the core radius, ~ 10 km, T falls off faster than $r^{-1/2}$ (see appendix C.2), the total luminosity decreases with increasing r. This means that as the new particle becomes more and more weakly coupled, it can travel through the star easier and so the radius of blackbody emission shrinks. As the blackbody radius shrinks, the emitted luminosity increases (assuming it is outside the proto-neutron star's core) and so in the trapping limit, the Raffelt criterion excludes all couplings *weaker* than a certain value.

Now we will apply this trapping constraint to our model. Both the axion and dark photon have their own mean free paths λ_a and λ_D from their decay and scattering with SM particles. From these mean free paths we define the two radii r_a and r_D via Eq. 4.8. Effectively, these radii can be thought of as the radius below which the corresponding particle is trapped and outside of which it free-streams.

The difference between r_a and r_D introduces extra complications that precludes a simple treatment of the luminosity of both dark photons and axions as arising from a blackbody. This arises from the fact that in the region between the two radii neither of the particles are in thermal equilibrium with the rest of the proto-neutron star, and so the assumptions that go into treating the outer radius as a blackbody fail. To illustrate these complications, let us consider the case where $r_D < r_a$, i.e. the dark photon becomes free-streaming at a smaller radii than the axion. While the dark photon can be treated as a blackbody emitting from r_D, the axion emission is not so simple. In the region between r_D and r_a, the axion scatters or decays before traveling a

large distance, but the dark photon can easily escape the region without subsequent interactions. Because any interaction/decay of the axion converts it into a dark photon, even though from Eq. 4.8 we find that the axion is trapped, after a single interaction a portion of its energy goes into dark photons that can escape the region. Therefore, we can treat the smaller radii as a blackbody for both particles, but we must take into account the transmission probability for the energy that is radiated into axions.

Once produced at the inner trapping radius, the particle associated with the larger trapping radius travels a finite distance before having an interaction (scattering or decay) that converts it into the free-streaming particle. The luminosity associated with the trapped particle depends on the probability that the free-streaming particle created in that interaction travels outward (so that it does not return to the inner radius), P_θ, and the fraction of the initial particle energy carried by the free-streaming particle, ϵ. Calculating those factors precisely is computationally intensive and amounts to small changes in the final result. To simplify, we take P_θ and ϵ to have the same value for all scatterings. So that the total luminosity is

$$L_{tot}(r_{in}) = L_{Blackbody}(r_{in}, m_{in}, g_{\star,in}) + \epsilon P_\theta L_{Blackbody}(r_{in}, m_{out}, g_{\star,out}), \tag{4.12}$$

where $m_{in}, m_{out}, g_{\star,in}$, and $g_{\star,out}$ are the masses and degrees of freedom of the particle corresponding to the inner and outer radius respectively. In reality, P_θ depends on how far the initial particle makes it from the blackbody before scattering since the further it makes it out, the more solid angle it can scatter into without being directed back into the blackbody. Thus we can say that $1/2 \leq P_\theta \leq 1$. To get an estimate for ϵ we can easily see that, depending on the mass of the initial particle and whether the event is a scattering or a decay, in the center of mass, frame the final

particle takes between $1/2$ and all of the initial particle's energy. Thus we have $1/2 \leq \epsilon \leq 1$. To get a conservative estimate on our coupling we note that if we underestimate our total luminosity, we will also underestimate the radius of the blackbody once we solve $L_{tot}(r_{in}) = L_\nu$. This means we will be underestimating the constraint on the coupling thus giving us a conservative upper bound. We therefore take the conservative estimate of $\epsilon = P_\theta = 1/2$. In order to get a sense of the maximum value our constraint could be off by, we look at the other extreme $\epsilon = P_\theta = 1$. This changes the value of the constraint curve by at most around 20%, so we use the value $\epsilon P_\theta = 1/4$ as it provides a good conservative estimate of the constraint.

Now we compute the mean free paths of the axion and dark photons. The mean free path for both particles is determined by their scattering cross section with the three electrically charged fermions in the supernova: electrons, positrons, and protons as well as their decay width (where only the heavier between the axion and dark photon decays). The diagrams for these scatterings and decays are shown in Fig. 4.4 with ψ designating any of the three fermions.

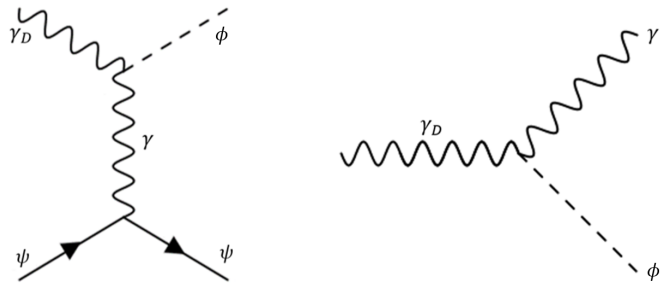

Figure 4.4: The diagrams for the dark photon's scattering off of fermions and its decay into an axion and photon. ψ represents any of the electrically charged fermions in the supernova: electrons, positrons, and protons. The diagrams for axion's scattering from fermions and its decay are identical to this but with the axion and dark photon exchanged. These diagram are used to compute the momentum transfer cross sections for the various scattering processes and the decay width for the axion and dark photon. These cross sections are then used to place a trapping constraint on the coupling $1/f_a$.

In order to compute the mean free path, we must compute the cross sections and decay

widths from these interactions. However, rather than using the ordinary cross sections to determine the mean free paths, we will use the momentum transfer cross section defined as

$$\sigma_{\Delta \boldsymbol{p}} = \frac{1}{4E_A E_B \Delta \boldsymbol{v}} \int d\Pi_f (1 - \cos(\theta)) |\mathcal{M}|^2. \tag{4.13}$$

Using the momentum transfer cross section means that we are favoring scatterings with a more severe angular deflection because they are more effective at trapping particles than those with a small angular deflection. The momentum transfer cross section also helps to regulate the t channel divergence that appears in our diagrams when $m_a = m_D$. The computation of these cross sections is detailed in appendix C.1, where we show the cross sections take the form

$$\sigma_{a\psi \to \gamma_D \psi} = \frac{\alpha_e}{3 f_a^2} \frac{s\beta(s, m_\psi, m_D)}{2E_A E_B |\boldsymbol{v}_A - \boldsymbol{v}_B|} I(s, m_\psi^2, m_a^2, m_D^2) \tag{4.14}$$

$$\sigma_{\gamma_D \psi \to a\psi} = \frac{\alpha_e}{3 g_{\star,D} f_a^2} \frac{s\beta(s, m_\psi, m_a)}{2E_A E_B |\boldsymbol{v}_A - \boldsymbol{v}_B|} I(s, m_\psi^2, m_D^2, m_a^2), \tag{4.15}$$

where m_ψ is the mass of the fermion the axion or dark photon is scattering with. The definition for I is given Eq. C.64 in appendix C.1, and is exactly 1 for $m_a = m_D = 0$. The decay widths are computed in appendix C.1 and are

$$\Gamma_a = \frac{m_a^4}{32\pi f_a^2 E} \left(1 - \frac{m_D^2}{m_a^2}\right)^3, \qquad \Gamma_D = \frac{m_D^4}{96\pi f_a^2 E} \left(1 - \frac{m_a^2}{m_D^2}\right)^3, \tag{4.16}$$

where E is the energy of the initial particle. The mean free path λ for the axion and dark photon

are defined as

$$\frac{1}{\lambda_a} = \Gamma_a + \sum_{\psi} n_{\psi} \left\langle \sigma_{a,\psi} \right\rangle_{\psi} \ , \qquad \frac{1}{\lambda_D} = \Gamma_D + \sum_{\psi} n_{\psi} \left\langle \sigma_{D,\psi} \right\rangle_{\psi} \ , \tag{4.17}$$

where in the sum ψ represents: electrons, positrons and protons. $\sigma_{a,\psi}$ is a short hand notation for the momentum transfer cross section of an axion with fermion ψ and likewise $\sigma_{D,\psi}$ for the dark photon. Additionally, the subscript ψ in the thermal average in Eq. 4.17 is meant to convey that we are taking the average of initial fermion states only. For the initial boson (axion or dark photon) energy we simply input the average energy of a boson at radius r_i.

It is important to highlight why inserting the average energy for the initial boson (call it X), rather than averaging over initial energies is the more physically accurate thing to do. This stems from the fact that particles of different energies decouple at different radii, and thus treating this radiation as a blackbody emission is an approximation. This approximation can become very inaccurate when applied to particles that have inelastic scatterings. Consider the scenario where the final state boson has a very large mass, M. In order to have enough energy to produce the much more massive final state boson, the particle ψ that X scatters off of needs to have very high energy. The lower the energy of X, the higher the energy of ψ needs to be. This implies that X with a lower energy will scatter less frequently than X of higher energy. In the limit that $M \gg T$, most of the initial state bosons are effectively free while only those with very high energy have a chance at scattering. Averaging over initial state X energies fails to capture this behavior effectively because it will assign every X the same mean free path regardless of energy. This would lead us to conclude that the typical thermal bosons in the supernova scatter much more effectively than they actually do which in turn would lead us to overestimate the extent to

which these particles are trapped in the supernova. In order to capture the dynamics, which is dominated by particles with energies close to the average energy, it is more physically accurate to use the mean free path for particles with energy $\langle E_b \rangle$. So, the thermal average used in Eq. 4.17 is defined as

$$\langle \sigma_{a,\psi} \rangle_{\psi} = \int \frac{d^3\boldsymbol{p}_\psi f(E_\psi, T(r), \mu_\psi(r))}{(2\pi)^3 n_\psi(r)} \sigma_{a,\psi}(E_\psi, \langle E_b \rangle_{r_i}), \tag{4.18}$$

where

$$\langle E_b \rangle_{r_i} = \int \frac{d^3\boldsymbol{p}_b f(E_b, T(r_i))}{(2\pi)^3 n_b(r_i)} E_b. \tag{4.19}$$

Now we can use these cross sections and the corresponding mean free paths to place the constraint on the coupling. The radii r_a and r_D, are implicitly defined as functions of the coupling using Eq. 4.8 and using the mean free paths defined in Eq. 4.17. Then we can numerically solve for the value of f_a such that the emitted luminosity given in Eq. 4.12 is equal to L_ν

$$L_{tot}(\min(r_a(f_a), r_D(f_a))) = L_\nu \tag{4.20}$$

Since we expect both radii to decrease with increasing f_a, and that the blackbody luminosity should increase as the radii decrease, we can exclude couplings below $1/f_a$ (but larger than the constraint from bulk emission). The region of parameter space excluded by supernovae is shown in Fig. 4.5. The first plot considers a massive axion and massless dark photon while the second considers a massless axion and massive dark photon. The high mass behavior of these constraints is quite different from the usual supernova constraint behavior. Ordinarily, the trapping constraint curve comes down to intersect the bulk emission curve to form a closed constrained region. However, we see that in our constraints, the region does not close off, but is an exponentially

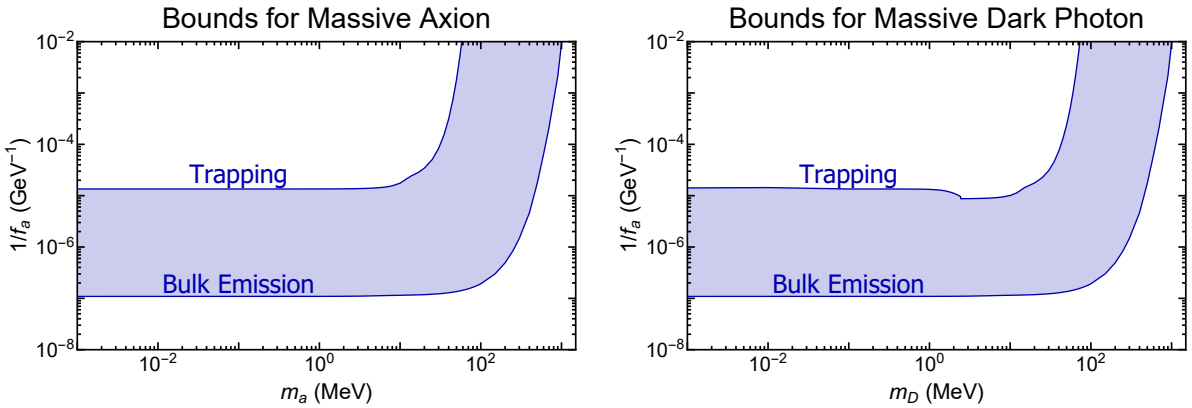

Figure 4.5: These plots show the lower constraint from bulk emission and the upper constraint from trapping as a function of particle mass. The first plot shows these constraints for a massive axion and massless dark photon and the second plot shows them for a massive dark photon and a massless axion. Note that the upper trapping limit only contains the contributions from trapped axions and transverse dark photons since we must treat the longitudinal dark photons separately (See Sec. 4.3).

increasing strip. We will now look into the limiting behavior of the constraints in the high mass limit, $M \gg T$, where M is the mass of the massive final state boson to determine the origin of this unique behavior.

Origin of the high mass scaling

The high mass behavior of the bulk emission curve is straightforward to understand. The initial particles must have enough energy to produce this very massive particle. This leads to the luminosity being Boltzmann suppressed for $M \gg T$. The constraint curve is found by demanding $L_{\text{bulk}}(f) = L_\nu$ so in order to compensate for the exponentially decreasing luminosity, the coupling must increase in exactly the same way. This leads to the exponentially increasing constraint curve for the bulk emission shown in Fig. 4.5. This type of scaling is expected in supernova constraints for any novel massive particle.

The trapping constraint curve is a bit more difficult to understand. To understand the scaling at high mass, first consider a more typical model that contains only one novel particle radiating

like a blackbody. For this type of model, the constraint decreases with mass M for $M \gg T$ due to the fact that the radiation of a blackbody decreases as the particles mass increases. In order to keep $L_{trapping}(r, M) = L_\nu$ the radius of the blackbody must decrease to compensate for this mass suppression. This smaller radius then implies that the constrained coupling is weaker and gives a decreasing coupling constraint in the high mass limit.

Contrast this behavior with a model, like ours, that contains two novel particles. As one of the particles gains mass, M, it is still true that the blackbody emission of that particle gets suppressed. However, the blackbody emission of the massless particle does not get suppressed. So in the high mass limit, the total luminosity is only due to blackbody radiation of this massless particle. Demanding that $L_{tot} = L_\nu$ then fixes the radius of emission to a radius r_0, which is independent of the heavy mass M. Now, the trapping constraint curve is found by demanding that $\tau(r_0) = 2/3$. This optical depth is determined by the strength of the scattering of the massless particle into the massive particle (with mass M). This up-scattering process will be Boltzmann suppressed for $M \gg T$ and so to compensate, the coupling must increase in exactly the same way. This gives the exponentially increasing constraint curve that we observe in Fig. 4.5.

We will now investigate in more detail the source of these two exponentially increasing curves to determine the shape of their fall off. In particular, we will show that the bulk emission constraint scales exponentially in M/T while the trapping constraint scales exponentially in M^2/T^2. To do this we can look at the scaling of each constraint in the limit $M \gg T$ ignoring $\mathcal{O}(1)$ factors. For both curves, we found that this scaling is the inverse of the Boltzmann suppression of the initial particles in each interaction. Let us start with the bulk emission constraint. The dominant process here is the annihilation process. The electrons and positrons are largely

relativistic so we can ignore their mass m_e. A simple computation gives,

$$M^2 > s \sim E_{e^+} E_{e^-} \tag{4.21}$$

This is most easily satisfied if both energies are of order M leading to a Boltzmann suppression $e^{-M/T}$. Thus the bulk emission constraint scales like,

$$1/f_{a,bulk} \sim e^{M/T} \quad \text{for} \quad M \gg T. \tag{4.22}$$

For the trapping constraint, the dominant scattering is the scattering off of electrons. In order for this scattering to be kinematically allowed, $s > (M + m_e)^2$. Again, we ignore m_e to find,

$$M^2 > s \sim E_{e^-} E_b \tag{4.23}$$

Where E_{e^-} is the energy of the initial electron and E_b is the energy of the initial, massless boson. Since E_b is fixed to be the thermal average energy, $E_b \sim T$, we conclude that

$$E_{e^-} \gtrsim M^2/T. \tag{4.24}$$

This leads to a Boltzmann suppression of the scattering that scales as e^{-M^2/T^2}. The scaling of the trapping constraint curve is thus

$$1/f_{a,trap} \sim e^{M^2/T^2} \quad \text{for} \quad M \gg T. \tag{4.25}$$

Since the trapping curve scales as e^{M^2/T^2} and the bulk emission curve scales as $e^{M/T}$ the two curves never meet and diverge from one another. Note that if E_b is not fixed to be the averaged energy, then we are free to let both $E_b \sim M$ and $E_{e^-} \sim M$ so that our Boltzmann suppression will look like $e^{-M/T}$. This will lead to a trapping constraint that scales as $e^{M/T}$ for $M \gg T$. This very different asymptotic scaling of the trapping constraint highlights how important it is to use the averaged initial energy rather than averaging over the initial energies of the boson.

4.3 Longitudinal Dark Photons

A massive vector boson like the dark photon has a longitudinal polarization that behaves quite differently from its transverse counterparts. In particular, as we will show, for small dark photon mass, the coupling of the longitudinal dark photon is highly suppressed. This difference in coupling motivates us to consider the transverse and longitudinal dark photons as two separate particles. This allows us to get two constrained regions by applying the constraints from Sec. 4.1 and Sec. 4.2 to each polarization separately.

Let us now consider longitudinal dark photons in the small m_D limit. We will show that the coupling of the longitudinal dark photons gets suppressed by a factor of its mass, m_D. This is a result of the Goldstone Boson Equivalence Theorem. To see this, consider leaving the unitary gauge of our model through a gauge transformation

$$A_\mu^D \to A_\mu^D + \frac{1}{m_D}\partial_\mu \zeta \,. \tag{4.26}$$

The mass term for the dark photon gives rise to a kinetic term for the Goldstone boson, ζ, and a

2-point interaction/mixing term with the dark photon

$$\frac{1}{2}m_D^2 A_D^\mu A_\mu^D \to \frac{1}{2}m_D^2 A_D^\mu A_\mu^D + \frac{1}{2}\partial_\mu\zeta\partial^\mu\zeta + m_D A_D^\mu \partial_\mu\zeta. \tag{4.27}$$

The Goldstone Boson Equivalence Theorem states that in the low mass/high energy limit, the amplitude for a matrix element containing a longitudinal dark photon is equal to the amplitude for the same process with the longitudinal dark photon replaced with the Goldstone boson. In the low mass/high energy limit the mixing term $m_D A_D^\mu \partial_\mu \zeta$ can be treated as an interaction term with coupling m_D. Since this is the only interaction the Goldstone boson has, we know that any matrix element with an external Goldstone boson must scale as m_D. So for masses with $m_D \ll T$, we should find $\mathcal{M}_L \sim m_D$ where $\mathcal{M}_L$ is any matrix element involving a longitudinal dark photon in the initial or final state. This argument is illustrated pictorially in Fig. 4.6.

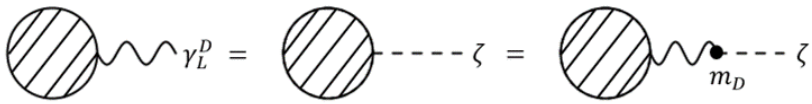

Figure 4.6: A pictorial representation of the suppression of matrix elements containing longitudinal dark photons in the low mass/high energy limit. The first equality is the Goldstone boson equivalence theorem stating that in the low mass/high energy limit, any matrix element with an external longitudinal photon is equal to the same matrix element with the longitudinal dark photon replaced with the Goldstone boson. The second equality makes use of the 2-point Goldstone boson-dark photon interaction term that results from leaving unitarity gauge. This coupling scales as m_D which gives the desired result.

Now let us compute the constraints coming from the longitudinal dark photon. We start with the bulk emission constraint from Sec. 4.1. In order to compute this bulk emission constraint

we need to compute the emissivity of longitudinal dark photons

$$\dot{\epsilon}_L^D = \left(\prod_i \int \frac{d^3\boldsymbol{p}_i}{(2\pi)^3 2E_i} f_i\right)\left(\prod_f \int \frac{d^3\boldsymbol{p}_f}{(2\pi)^3 2E_f}\right) \overline{|\mathcal{M}_L|^2} E_D (2\pi)^4 \delta^4\left(\sum p_i - \sum p_f\right). \quad (4.28)$$

This is the same as Eq. 4.2, but rather than summing over all dark photon spins in the final state, we simply insert the longitudinal polarization for the dark photon (where longitudinal is defined in the frame of the star). We also are only accounting for the energy emitted by the longitudinally polarized dark photons, since we will assume that the axion is trapped in the supernova for the couplings of interest. We will consider two processes that produce longitudinal dark photons. First, we will consider the annihilation process, since it was the dominant process in the full emissivity. Second, we consider the plasmon decay process because the mass suppression has a smaller impact on this process compared to the others. A general computation given in appendix C.1 shows that any production process will have a matrix element that scales as m_D^2/s in accordance with the Goldstone boson equivalence theorem. For the plasmon decay, the center of mass energy in this process is the plasmon mass which is of the same order as the plasmon frequency, ω_p. The plasmon frequency is around a full order of magnitude smaller than the typical center of mass energy for annihilation so the m_D^2/s suppression factor leads to the plasmon decay emissivity being significantly less suppressed by the mass of the dark photon than the other processes. In fact, after computation, we find that plasmon decay is the dominant process in the production of longitudinal dark photons if $m_D < \omega_p$. The emissivities are computed in appendix C.1

$$\begin{aligned}
\dot{\epsilon}_a^L &= \left(\frac{m_D^2}{\langle s\rangle}\right)\frac{\alpha_e}{24 f_a^2} n_{e^-} n_{e^+} \langle E_{tot}\rangle\, Q_L^a(m_a, m_D)\,, \\
\dot{\epsilon}_p^L &= \left(\frac{m_D^2}{\omega_p^2}\right)\frac{\zeta(3) T^3}{3\pi f_a^2}\left(\frac{\omega_p^2}{4\pi}\right)^2 Q_L^p(m_a, m_D)\,.
\end{aligned} \quad (4.29)$$

Just as before Q_L^a and Q_L^p are $\mathcal{O}(1)$ numbers for low m_D and m_a and are defined in appendix C.1. Comparing Eq. 4.29 to the emissivities given in Eq. 4.5 and Eq. 4.7 for the annihilation and plasmon decay emissivities, we can see that they have the same form but with an additional m_D^2/s-type suppression factor in both.

For the longitudinal trapping bounds we will need to compute the cross section for longitudinal dark photons scattering with fermions, as well as their decay width. The decay width for the longitudinal dark photon can be seen to be the same as the decay for the transverse dark photon by considering the decay in the dark photon's rest frame. Thus the decay width is the same as that given in Eq. 4.16.

Next, we turn to the scattering cross section for longitudinal dark photons. The matrix element for this process is the same as the second diagram in Fig. 4.1, with the polarization of the initial dark photon chosen to be longitudinal. The computation is very similar to that of the full scattering cross section and is detailed in appendix C.1. The result is

$$\sigma_{\Delta \boldsymbol{p}}^{\gamma_D^L \to a} = \frac{\alpha_e}{3 f_a^2} \left(\frac{m_D^2}{s} \right) \frac{s\beta'}{2 E_A E_B |\boldsymbol{v}_A - \boldsymbol{v}_B|} \left(\frac{2|\boldsymbol{p}|^2 \sin^2(\theta)}{s\beta^2} \left(I(m_D^2, m_a^2) - \frac{V\beta'}{3\beta} \right) + \frac{V\beta'}{3\beta} \right). \tag{4.30}$$

Fig. 4.7 shows the constraints for transverse dark photons and longitudinal dark photons described above as a function of the dark photon mass. The longitudinal constraints exhibit a number of interesting features. In the low mass regions, the longitudinal constraints on the coupling scale as $\sim m_D^{-1}$ due to the $\mathcal{M} \sim m_D/f_a$ scaling described above. In the high mass region, this scaling changes for the longitudinal trapping as the decay becomes the dominant mode of trapping. The decay matrix element scales as $\mathcal{M} \sim m_D^2$ and thus the scaling of the constraint on the coupling changes to $\sim m_D^{-2}$. The bulk longitudinal bound begins to increase at around 20 MeV is due to

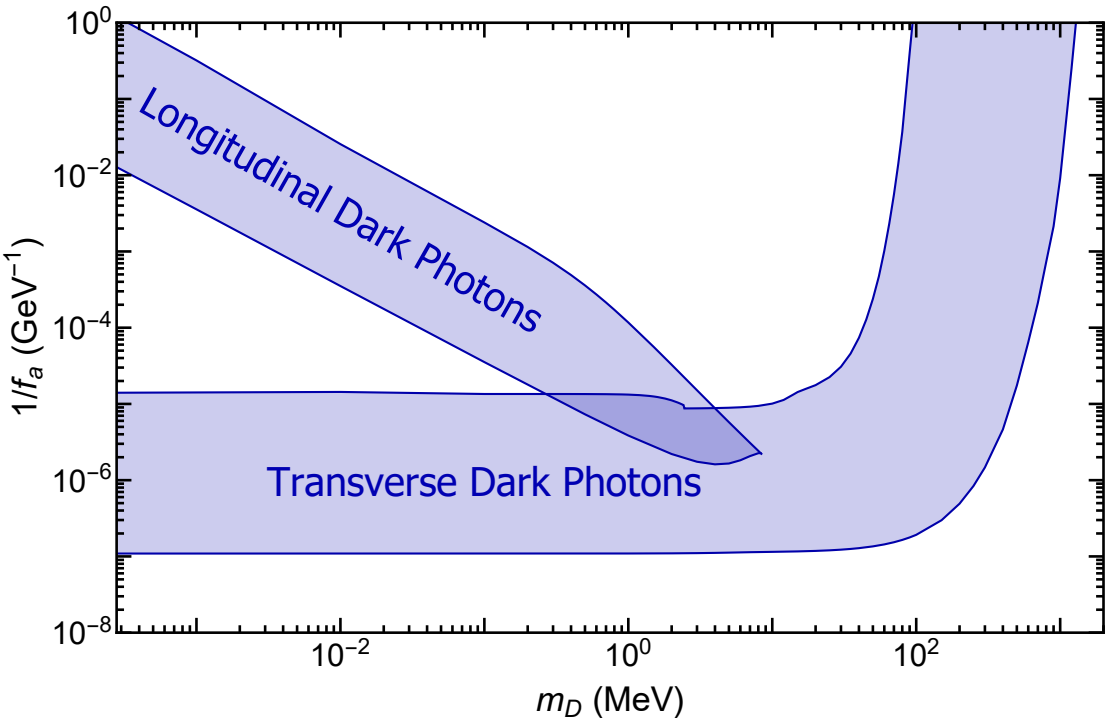

Figure 4.7: A plot of the longitudinal and transverse constraints as a function of dark photon mass. The transverse constraints are analogous to those shown in Fig. 4.5. The longitudinal constraints are found by applying the bulk emission constraint and the trapping constraint to longitudinal dark photons only.

the plasmon decay being kinematically forbidden once $m_D > m_p$, where $m_p \sim \omega_p$ is the mass of the plasmon.

4.4 Other Astrophysical Constraints

As a final exercise, we can improve on our constraints, especially in the low mass regions by using our cross section computations in other astrophysical situations. We will examine white dwarf cooling bounds and BBN N_{eff} bounds.

White Dwarfs

First, we consider white dwarfs. A cooling bound on the coupling, similar to that found for SN1987A, can be derived from white dwarf data. For low temperature white dwarfs, the dominant

source of energy emission is the emission of surface photons via blackbody radiation. This, along with the degeneracy of the white dwarf, allows one to derive a simple power law relationship between the luminosity of a white dwarf and the relative abundance of white dwarfs with that luminosity in the universe known as "Mestel's Law". For higher luminosity white dwarfs, bulk neutrino emission begins to play a significant role in cooling the white dwarfs resulting in a dip in the white dwarf abundance at higher luminosity. Observations of white dwarf abundance agree well with Mestel's Law and the so-called neutrino dip. An additional channel of significant bulk emission would increase this dip spoiling this agreement. It has been found that any additional mode of bulk particle emission must have an emissivity less than that of the neutrinos in order to preserve experimental agreement [94]. Therefore, the cooling constraint for white dwarfs can be summarized as

$$\dot{\epsilon}_x < \dot{\epsilon}_\nu. \tag{4.31}$$

For neutrino emission and our axion/dark photon emission, plasmon decay is the dominant source of particle production in white dwarfs and thus will be the only process considered. Ref. [63] has computed a nice expression for the emissivity of Standard Model neutrinos

$$\epsilon_\nu = \frac{8\zeta(3)T^3}{3\pi}\frac{C_V^2 G_F^2}{\alpha_e}\left(\frac{\omega_p^2}{4\pi}\right)^3 Q_3, \tag{4.32}$$

where

$$Q_3 = Q_3^L + Q_3^T \tag{4.33}$$

$$Q_3^L = \frac{1}{4\zeta_3 T^3}\int_0^{k_1} d|\boldsymbol{k}|\frac{|\boldsymbol{k}|^2}{e^{\omega_\ell/T}-1}\frac{\omega_\ell^2}{\omega_p^2}Z_L\hat{\pi}_\ell^2\,, \qquad Q_3^T = \frac{1}{2\zeta_3 T^3}\int_0^{\infty} d|\boldsymbol{k}|\frac{|\boldsymbol{k}|^2}{e^{\omega_t/T}-1}Z_T\hat{\pi}_t^3. \tag{4.34}$$

This shares a similar form to our expression for the emissivity of axions and dark photons, given

in Eq. 4.7. In our constraints, we take the white dwarf to have a constant temperature ($T = 2\,\text{keV}$) and constant plasmon frequency ($\omega_p = 40$ keV) as is typical for white dwarf constraints [63]. Applying Eq. 4.7 and Eq. 4.32 to the constraint given in Eq. 4.31 we get a constraint on the coupling

$$1/f_a < (2.3 \times 10^{-9}\ \text{GeV}^{-1})\sqrt{\frac{Q_3}{Q^p(m_a, m_D)}}\,, \tag{4.35}$$

in agreement with previous considerations of this bound [15, 22]. At low masses $Q_3 \approx Q^p$, but as the mass of the axion or dark photon increases Q^p decreases. An upper trapping bound on the excluded region from white dwarfs could be obtained but is rendered irrelevant by even the most conservative BBN ΔN_{eff} bound.

BBN Bounds

Now we consider a very simple, conservative BBN ΔN_{eff} bound. In our simple constraint, we demand that axions and dark photons were not in equilibrium at nucleosynthesis as the addition of 3 (or 4 for massive dark photons) bosonic degrees of freedom in the radiation density would induce too large of an increase in the number of effective neutrinos. We take the temperature at nucleosynthesis to be $T_{BBN} = 2$ MeV, both m_a and m_D to be smaller than T_{BBN}, and consider pair production of axions and dark photons through electron-positron annihilation. To implement ΔN_{eff} bounds, we demand that

$$n_e^2 \left\langle v_{mol} \sigma_{e^+e^- \to \phi\gamma_D} \right\rangle < n_{a,\gamma_D} H(T_{BBN}), \tag{4.36}$$

where n_e is the number density of electrons and n_{a,γ_D} is meant to convey the equilibrium density

of whichever particle is massless. Neglecting the electron mass since $T_{BBN} > m_e$, we find

$$\langle v_{mol}\sigma_{e^+e^-\to\phi\gamma_D}\rangle = \frac{\alpha_e}{24 f_a^2}. \tag{4.37}$$

Inserting this with the densities and Hubble at 2 MeV, we get that the allowed couplings must satisfy, $1/f_a < 4.5\times10^{-7}$ GeV^{-1} for massless axions and $1/f_a < 6.5\times10^{-7}$ GeV^{-1} for massless dark photons. This constraint applies until the mass of the axion or dark photon is around 1 MeV at which point they no longer contribute to the radiation density.

These two constraints as well as the supernova and collider constraints taken from Ref. [95] are shown in Fig. 4.8. Note that only the constraints for the massive dark photon show collider constraints since Ref. [95] derive their constraints explicitly in the limit $m_D \gg m_a$. Similar constraints could be derived in the limit $m_a \gg m_D$ although this has not been done. We expect that collider constraints for $m_a \gg m_D$ will exclude a similar region of the parameter space as those for $m_D \gg m_a$, but have refrained from including it in Fig. 4.8.

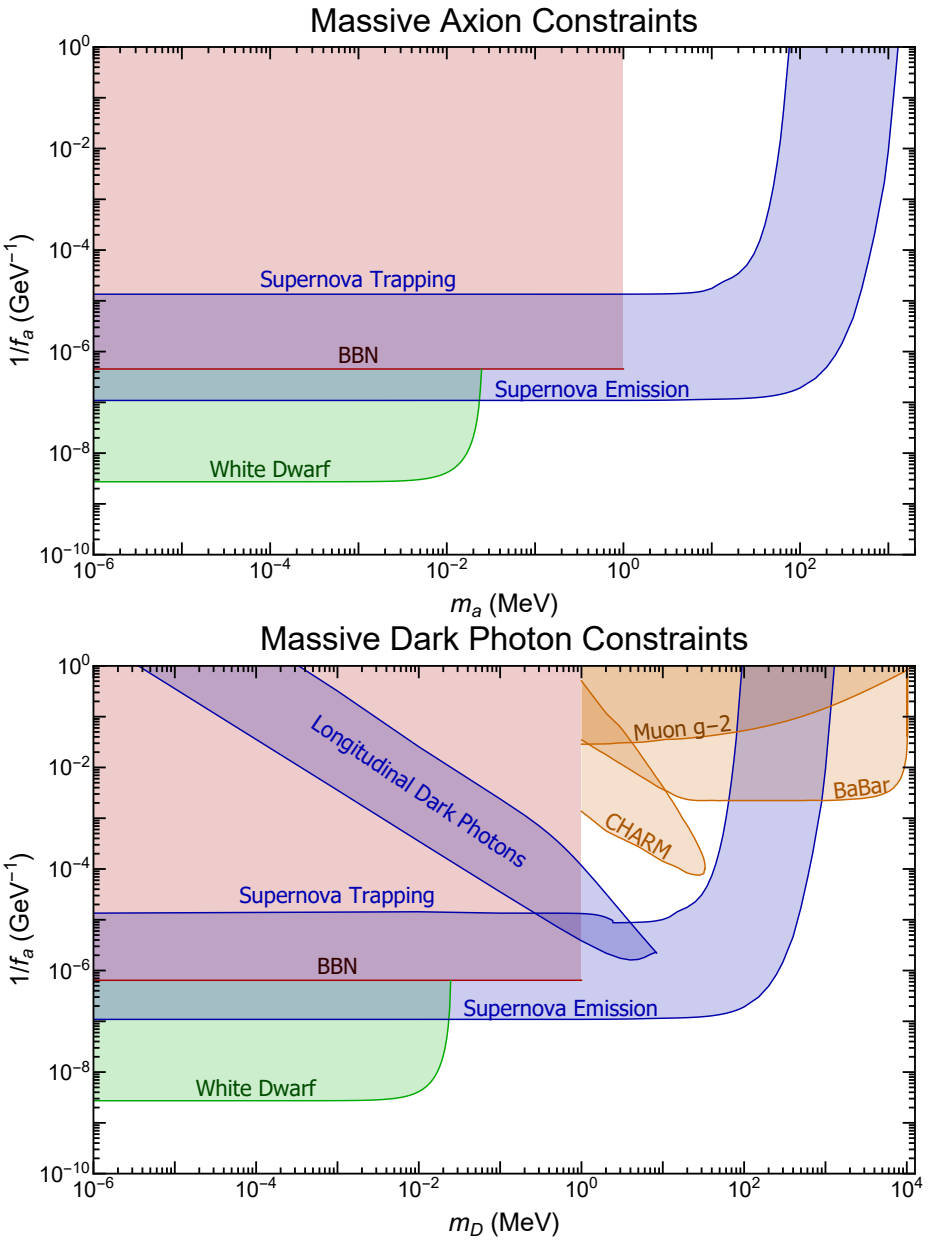

Figure 4.8: The constrained regions on the coupling $1/f_a$ from the various astrophysical and collider sources. The first plot corresponds to a massive axion and a massless dark photon while the second plot corresponds to a massive dark photon and a massless axion. The blue constraints are those due to the supernova constraints examined in Sec. 4.1, Sec. 4.2, and Sec. 4.3. The green constraint is due to white dwarf cooling constraints examined in Sec. 4.4. The red constraint is a very conservative BBN constraint computed in Sec. 4.4. The orange constraints are the various collider constraints taken from Ref. [95]. Note that these constraints are only shown in the massive dark photon plot since Ref. [95] only considers the $m_D \gg m_a$ limit. Similar collider constraints exist for the opposite limit but have not yet been computed. Also note that slightly stronger bounds than the white dwarf cooling bounds can be obtained by using the recent analysis of the tip of the red giant branch [17, 96].

Chapter 5: Conclusion

In this thesis, we presented and detailed a variety of new and exciting results in BSM physics. In Chapter 2 we examined the structure of fermion bound states around magnetic monopoles. In an $SU(2)$ gauge theory with N_f fermions, giving mass to the fermions breaks their $SU(N_f)$ flavor symmetry into either an $Sp(N_f)$ or $SO(N_f)$ flavor symmetry depending on how they are paired by these mass terms. We then considered the $SU(2)$ gauge theory undergoing spontaneous symmetry breaking down to a $U(1)$ electromagnetic theory and found the resultant IR theories are identical for both scenarios.

In section 2.2 we considered these theories in the vicinity of a t'Hooft Polyakov Monopole that was produced in the symmetry-breaking process. The monopole background breaks the combined gauge and rotation groups into a diagonal subgroup effectively giving an extra source of angular momentum for the charged fermions around the monopole. We then found the zero angular momentum mode for the fermions around the monopole, which is the only mode that interacts directly with the monopole core, and showed that by considering only this mode, the theory reduces to a theory of fermions on a half-line in 1+1D. Between the $SO(N_f)$ and $Sp(N_f)$ theories, the only difference in the 1+1D reduced theories were the boundary conditions at the monopole core, reflecting the equivalence of the theories in the IR.

This theory of 1+1D fermions was then taken and bosonized in 2.3 to give an equivalent

theory of 1+1D bosons. Both theories satisfy nearly the same Lagrangian consisting of N_f sine-Gordon scalars coupled via an electromagnetic term. In the $SO(N_f)$ theory, we found the scalars had a radially dependent mass term which goes to zero at the monopole core and is constant at large r. This effect was found through the careful bosonization process in appendix A.3.1, which as far as we know has not been considered before. In section 2.4 we explored solutions to an $N_f = 1$ toy model to familiarize ourselves with aspects of this theory. We were able to derive many useful analytic approximations to the solutions and their energies.

We then moved on to perform an in-depth analysis of the landscape of the fermion bound states in the $N_f = 2$ theory in section 2.5. We found very interesting differences between the theories. We found that, in the limit where one fermion is much heavier than the other, the monopole in the $SO(N)$ receives a mass correction on the order of the lighter mass while in the $Sp(2)$ theory the monopole receives a correction on the order of the heavier mass. We found that in the $SO(2)$ the ground state of the monopole is always the dyon of minimal charge while for the $Sp(2)$ theory, the ground state can be a state of non-minimal charge. Additionally, the landscape of stable excited dyon states was found to differ considerably between the two theories. We concluded by demonstrating perhaps the most surprising result: The $Sp(2)$ monopole received a θ mass correction and charge distribution even if one of the fermion was massless.

We briefly touched on the $N_f \geq 4$ case by analyzing the stability of the monopole and finding the number of stable excited states when $\theta = 0$. We found that states in the $Sp(N_f)$ that carry $B - L$ charge could not possibly be stable concluding that only electric charge can be carried by stable states if $\theta = 0$. In section 2.7, we showed how many of these results can apply to the $SU(5)$ monopole which is approximately equivalent to our $Sp(4)$ model.

The results of this chapter are interesting beyond simply the study of dyons. For example,

the completeness conjecture is the hypothesis that particles with all combinations of electric and magnetic charges are present [97]. Notice that in our charge-lattice plot in figure 2.4, the charge lattice point with $Q_{EM} = 1/2$ and $Q_{B-L} = 0$ is missing and cannot be filled with bound states of leptons and baryons. At first, this seems to violate the completeness conjecture. However, this charge lattice point is filled by a dyon - antimonopole bound state. Our calculations imply that this dyon - antimonopole bound state is stable in our theory. If there are flavorless fermions, the dyon and antimonopole could annihilate and emit a flavorless fermion (this fermion would only need to be light enough to be kinematically accessible). However, if every fermion has flavor symmetries, as they do in our theories, then there is simply no final state with $Q = 1$ and $Q_{\text{flavor}} = 0$ for the dyon and antimonopole to annihilate into. As a result, the bound state is stable! It would be interesting to study how these bound states are stabilized.

Finally, it would be interesting to study the formation of stable dyons by the Kibble-Zurek production mechanism. As monopoles are formed by the relaxation of the scalar vacuum, the accompanying relaxation of the fermionic vacuum may well create dyons as the mass difference between the two is negligible at those high energy scales. Because monopole - antimonopole annihilation is an important aspect of early universe monopole dynamics, the stability of the mixed dyon/monopole bound states may well have interesting phenomenological consequences.

In the subsequent two chapters, we studied the phenomenological consequences of an axion-dark photon-photon coupling. In chapter 3, we studied the effects of an axion-photon-dark-photon coupling on the Cosmic Microwave Background if either the axion or the dark photon is dark matter. This interaction, in a dark matter background, induces mixing of the photon with a new light boson, and can remove photons from the universe either before or after recombination. Removing photons from the baryon-photon plasma before recombination

produces the well-known, model-independent, μ distortion or y distortion, as well as a model-dependent distortion due to Doppler broadening. The size of the distortion is determined by the rate at which photons are removed from the spectrum. Removing photons after recombination naturally changes the frequency spectrum of the CMB and thus produces a distortion with a new spectral shape. We computed these individual distortions and the corresponding total distortion that would be produced by an interaction of this type in the presence of either axion or dark photon dark matter.

The distortion produced in the presence of dark photon dark matter is smaller than that produced by axion dark matter by a factor of $1/3$, but otherwise identical in terms of dependence on the model parameters. This is due to the energy of dark matter being spread over the 3 polarizations of dark photon dark matter, as opposed to the single polarization for axion dark matter. The interaction we study only couples a photon of given polarization to a single polarization of dark photon dark matter. Thus, a given photon effectively only couples to $1/3$ of the total dark matter background. This effectively leads to an interaction strength for dark photon dark matter that is $1/3$ of that for axion dark matter.

By comparing our computed distortions with the COBE-FIRAS data measuring the CMB frequency spectrum, we were able to place very restrictive bounds on our coupling $1/f_a$. These bounds are a significant improvement of several orders of magnitude over the previous best bound on this coupling from red giant cooling constraints [24] as shown in Fig. 3.5. Additionally, one can compare these bounds to those placed on the $\phi F\tilde{F}$ coupling in [98] and see that our bounds are several orders of magnitude stronger.

We also briefly considered the possibility of future measurements of the CMB frequency spectrum to detect distortions produced by this model. While the μ and y distortions are produced

by any mechanism that adds or removes energy from the photon spectrum before recombination, the distortions generated in the free streaming era when the resonance condition is met lead to much more distinctive spectral features. Thus, such resonant distortions offer a promising avenue to single out the axion-photon-dark-photon interaction if next-generation experiments measure distortions on the CMB spectrum.

In chapter 4, we considered the supernova bounds on the well-motivated topological axion-photon-dark photon coupling. This coupling is interesting because it doesn't require or generate kinetic mixing between the vectors, while at the same time, it can be responsible for generating the abundance of dark matter. The supernova bound on this coupling highlighted two generic features that appear in supernova constraints.

The first feature occurs when the interaction being probed at the supernova involves multiple new particles with different masses, an example familiar from similar to the dynamics in dark matter models involving co-annihilation [99] or co-scattering [100]. When this situation occurs, the production and scattering cross section decreases whenever one of the particles obtains a mass so that the bulk emission and trapping bounds never meet and instead both decrease exponentially.

The second feature is a bit more ubiquitous and involves the importance of treating longitudinal and transverse polarizations of particles independently, with their own cooling and trapping constraints. Because the longitudinal mode coupling is m_D/E suppressed in the low mass limit, it acts as its own weakly coupled particle that can cool supernova giving a cooling and trapping bound separate from the transverse modes.

Because these properties are generic, they will appear in all manners of motivated scenarios. The most obvious model where a new feature occurs is in dark photon models with kinetic mixing. If the dark photon is heavier than twice the electron mass, trapping is dictated by

decay rather than scatter. Since decay treats all polarizations the same, the differences between transverse and longitudinal modes don't become relevant until the dark photon mass is less than an MeV, where supernova bounds are superseded by other constraints.

Appendix A: Stable Excited Dyonic States of Magnetic Monopoles

This appendix covers the details of derivations and calculations from Chapter 2

A.1 2D Fermion Identities

Here we prove the correspondences between terms in the 1+3D theory with those in the 1+1D theory given in Eq. 2.15- 2.18. Before looking at each term individually, it is first useful to note that from the definition of the 1+1D spinor, ξ, and $\bar{\gamma}^\mu$ in Eq. 2.19,

$$\begin{aligned}
\bar{\xi}\gamma^0\xi =& \frac{|g-p|^2+|g+p|^2}{2} = g^*g + p^*p \\
\bar{\xi}\gamma^1\xi =& \frac{|g-p|^2-|g+p|^2}{2} = (g^*p + p^*g) \\
\bar{\xi}\gamma^5\xi =& \frac{(g^*-p^*)(g+p)-(g^*+p^*)(g-p)}{2} = g^*p - p^*g.
\end{aligned} \tag{A.1}$$

Also, it is easy to see that the spin-isospin singlet state $|s\rangle \equiv |\boldsymbol{\tau}+\boldsymbol{\sigma}=0\rangle$ obeys the following identities for the spin operator $\boldsymbol{\sigma}$ and the isospin operator $\boldsymbol{\tau}$.

$$\begin{aligned}
\langle s|\hat{\boldsymbol{r}}\cdot\boldsymbol{\sigma}|s\rangle = \langle s|\hat{\boldsymbol{r}}\cdot\boldsymbol{\tau}|s\rangle = 0 \\
\langle s|(\hat{\boldsymbol{r}}\cdot\boldsymbol{\sigma})(\hat{\boldsymbol{r}}\cdot\boldsymbol{\tau})|s\rangle = -1 \\
(\hat{\boldsymbol{r}}\cdot\boldsymbol{\sigma})^2 = (\hat{\boldsymbol{r}}\cdot\boldsymbol{\tau})^2 = 1
\end{aligned} \tag{A.2}$$

With these identities, it is easy to prove Eq. 2.15- 2.18. Starting with Eq 2.15, and inserting 2.14

$$i\chi^\dagger\partial_0\chi = \frac{i}{4\pi r^2}\langle s|(g^* + (\hat{\boldsymbol{r}}\cdot\boldsymbol{\sigma})p^*)(\dot{g} + (\hat{\boldsymbol{r}}\cdot\boldsymbol{\sigma})\dot{p})|s\rangle = i\frac{g^*\dot{g} + p^*\dot{p}}{4\pi r^2} = \frac{i}{4\pi r^2}\bar{\xi}\bar{\gamma}^0\partial_0\xi \tag{A.3}$$

And

$$\begin{aligned}
-i\chi^\dagger\sigma_i\partial_i\chi =& \frac{-i}{\sqrt{4\pi r^2}}\left\langle s|(g^* + p^*(\hat{\boldsymbol{r}}\cdot\boldsymbol{\sigma}))\sigma_i\partial_i\left(\frac{g(r,t) + (\hat{\boldsymbol{r}}\cdot\boldsymbol{\sigma})p(r,t)}{\sqrt{4\pi}r^2}\right)|s\right\rangle \qquad \text{(A.4)}\\
=& \frac{-i}{4\pi r^2}\left\langle s|(g^* + p^*(\hat{\boldsymbol{r}}\cdot\boldsymbol{\sigma}))\left((\hat{\boldsymbol{r}}\cdot\boldsymbol{\sigma})g'(r,t) + p'(r,t) - \frac{1}{r}\left((\hat{\boldsymbol{r}}\cdot\boldsymbol{\sigma})g(r,t) - p(r,t)\right)\right)|s\right\rangle\\
=& \frac{-i}{4\pi r^2}\left((g^*p' + p^*g') + \frac{1}{r}(g^*p - p^*g)\right) = \frac{i}{4\pi r^2}\left(\bar{\xi}\bar{\gamma}^1\partial_1\xi - \frac{1}{r}\bar{\xi}\bar{\gamma}^5\xi\right).
\end{aligned}$$

Which proves Eq. 2.15. Eq. 2.16 and 2.17 can easily be proven from the following identities:

$$\chi^\dagger\chi = \frac{1}{4\pi r^2}\langle s|(g^* + (\hat{\boldsymbol{r}}\cdot\boldsymbol{\sigma})p^*)(g + (\hat{\boldsymbol{r}}\cdot\boldsymbol{\sigma})p)|s\rangle = \frac{g^*g + p^*p}{4\pi r^2} = \frac{1}{4\pi r^2}\bar{\xi}\bar{\gamma}^0\xi \tag{A.5}$$

$$-\chi^\dagger(\hat{\boldsymbol{r}}\cdot\boldsymbol{\sigma})\chi = -\frac{1}{4\pi r^2}\langle s|(g^* + (\hat{\boldsymbol{r}}\cdot\boldsymbol{\sigma})p^*)(\hat{\boldsymbol{r}}\cdot\boldsymbol{\sigma})(g + (\hat{\boldsymbol{r}}\cdot\boldsymbol{\sigma})p)|s\rangle = -\frac{g^*p + p^*g}{4\pi r^2} = \frac{1}{4\pi r^2}\bar{\xi}\bar{\gamma}^1\xi \tag{A.6}$$

$$\chi^\dagger(\hat{\boldsymbol{r}}\cdot\boldsymbol{\tau})\chi = \frac{1}{4\pi r^2}\langle s|(g^* + (\hat{\boldsymbol{r}}\cdot\boldsymbol{\sigma})p^*)(\hat{\boldsymbol{r}}\cdot\boldsymbol{\tau})(g + (\hat{\boldsymbol{r}}\cdot\boldsymbol{\sigma})p)|s\rangle = -\frac{g^*p + p^*g}{4\pi r^2} = \frac{1}{4\pi r^2}\bar{\xi}\bar{\gamma}^1\xi \tag{A.7}$$

$$-\chi^\dagger(\hat{\boldsymbol{r}}\cdot\boldsymbol{\sigma})(\hat{\boldsymbol{r}}\cdot\boldsymbol{\tau})\chi = \chi^\dagger\chi = \frac{1}{4\pi r^2}\bar{\xi}\bar{\gamma}^0\xi. \tag{A.8}$$

Finally, we prove Eq. 2.18. For ease of computation, we adopt a coordinate system where $\boldsymbol{r}$ points in the z-direction. Then one can see

$$\epsilon_{iab}\sigma_i\tau_a\hat{r}_b = \sigma_x\tau_y - \sigma_y\tau_x. \tag{A.9}$$

Using some simple properties of systemsof 2 spin-1/2 particles, it's easy to show that

$$\sigma_x\tau_y|s\rangle = -\sigma_y\tau_x|s\rangle \tag{A.10}$$

$$\langle s|(g+(\hat{\boldsymbol{r}}\cdot\boldsymbol{\sigma})p)(\sigma_x\tau_y)(g+(\hat{\boldsymbol{r}}\cdot\boldsymbol{\sigma})p)|s\rangle = i\frac{(g^*-p^*)(g+p)-(g^*+p^*)(g-p)}{2} = i\bar{\xi}\bar{\gamma}^5\xi.$$

Then, it is easy to see that

$$-g\chi^\dagger\sigma^i\frac{\tau^a}{2}\chi A_i^a = \frac{A(r)}{2r}\chi^\dagger\epsilon_{iab}\sigma_i\tau_a\hat{r}_b\chi = i\frac{A(r)}{(4\pi r^2)r}\bar{\xi}\bar{\gamma}^5\xi. \tag{A.11}$$

A.2 Boundary Conditions

Here we derive the boundary condition $p(r=0)=0$ from the Lagrangian in Eq. 2.20. There we can find the Dirac equation near $r=0$ reads

$$0 = \not{\partial}\xi - \frac{\gamma^5}{r}\xi. \tag{A.12}$$

Note I have neglected the electromagnetic term since we can use the remaining gauge freedom to set $\dot{\lambda}(r=0)=0$ and we can ignore the effects of the mass terms since we are looking at scales of order $r_M^{-1} \gg m$. We have also set $A(r)=0$ as we are inside the monopole's core. We can consider only time-independent solutions since we are interested in fermions with energies much smaller than r_M^{-1}. In terms of g and p, these equations can be greatly simplified to

$$g' = \frac{g}{r} \qquad p' = -\frac{p}{r}. \tag{A.13}$$

These can easily be seen to have power-law solutions $g \propto r$ and $p \propto r^{-1}$. So we see that to have well-behaved finite solutions near the core we must enforce $p(r = 0) = 0$.

A.3 Bosonization

Here we give a detailed derivation of the bosonization process. We start by proving bosonization for a single fermion on the half-plane by assuming that a commutator of the corresponding scalar fields takes a specific form for small space-like separations. Then we will show that if the fermions in our theory obey the boundary conditions given in Eq. 2.28- 2.30, the scalar commutator takes the assumed form for both $SO(N_f)$ or $Sp(N_f)$ type boundary conditions.

A.3.1 Bosonization

Let ξ be a fermion field defined on a half-plane with some boundary conditions at $r = 0$ with a Lagrangian of the form

$$L = \int_0^\infty dr\; i\bar{\xi}\partial\!\!\!/\xi - m_i\bar{\xi}\xi + e\dot{\lambda}\bar{\xi}\bar{\gamma}^0\xi. \tag{A.14}$$

We will take our basis of $\bar{\gamma}^\mu$ that is given in Eq. 2.14. In the 1960's, works by Sugawara [101], Sommerfield [102] and others [103] showed that the stress-energy tensor for a theory of free massless fermions can be written in terms of its current j^μ as

$$T^{\mu\nu} = \frac{\pi}{2}\left(\{j^\mu, j^\nu\} - \eta^{\mu\nu} j^\alpha j_\alpha\right) \quad \text{where} \quad j^\mu(r) \equiv \lim_{r\to r'} \frac{1}{2}\left(\bar{\xi}(r)\bar{\gamma}^\mu\xi(r') + \bar{\xi}(r')\bar{\gamma}^\mu\xi(r)\right). \tag{A.15}$$

This is known as the Sugawara-Sommerfield construction of the stress-energy tensor. We can use this to write the stress-energy tensor of our theory as

$$T^{\mu\nu} = \frac{\pi}{2}\left(\{j^\mu, j^\nu\} - \eta^{\mu\nu} j^\alpha j_\alpha\right) + \eta^{\mu\nu}(m\bar{\xi}\xi - e\dot{\lambda}j^0). \tag{A.16}$$

This stress-energy tensor can be used in conjunction with the commutation identities,

$$[j^\mu(x), \xi(y)] = -\bar{\gamma}^0\bar{\gamma}^\mu\xi(x)\delta(x-y) \quad [\bar{\xi}(x)\xi(x), \xi(y)] = -\bar{\gamma}^0\xi(x)\delta(x-y), \tag{A.17}$$

which can be derived from the canonical equal time anticommutation identities for ξ, to derive the Heisenberg equations of motion for ξ

$$-i\partial_0\xi_i(r) = [H, \xi(r)] \tag{A.18}$$

$$-i\partial_1\xi_i(r) = \int_0^\infty dr' \left[{T^0}_1(r'), \xi(r)\right] = \frac{\pi}{2}\{j_i^1(r) + \bar{\gamma}^5 j_i^0(r), \xi_i(r)\}. \tag{A.19}$$

From this point, bosonization is proved in the following way. We start with an ansatz for our fermion field written in terms of a scalar field ϕ:

$$\tilde{\xi}(r,t) \equiv Z^{1/2}(r)\begin{pmatrix} :e^{-i\sqrt{\pi}\Phi_1(r,t)}: \\ e^{i\alpha}:e^{-i\sqrt{\pi}\Phi_{-1}(r,t)}: \end{pmatrix} \quad \text{where} \quad \Phi_\lambda(r,t) = -\lambda\phi(r,t) + \int_0^r dx\dot{\phi}(x,t) \tag{A.20}$$

where $\lambda = \pm 1$ and the colons indicate the normal ordering of the scalar field operators. It's worth noting that α is an arbitrary phase that is eventually determined by the boundary conditions on ξ. We define Φ_λ^+ and Φ_λ^- to be the portions of Φ_λ that contain the creation and annihilation operator

and likewise for $\phi^{\pm}$. We assume that $C_{\lambda,\lambda'}(r,r')$ defined as the limit

$$C_{\lambda\lambda'}(r,r') \equiv \lim_{r\to r',t\to t'}[\Phi^{-}_{\lambda}(r,t),\Phi^{+}_{\lambda'}(r',t')] \tag{A.21}$$

takes the following form.

$$C_{\lambda\lambda'}(r,r') = W(r,r') + \frac{1}{\pi}\begin{pmatrix} \ln(\epsilon - i(r-r')) & \ln\left(\frac{\mu e^{\gamma}}{2}\right) - F(r) - \frac{i\pi}{2} \\ \ln\left(\frac{\mu e^{\gamma}}{2}\right) - F(r) + \frac{i\pi}{2} & \ln(\epsilon + i(r-r')) \end{pmatrix} \tag{A.22}$$

where λ labels the columns and λ' labels the rows from $+1$ to -1 and μ is the scale at which normal ordering is performed. F and W are, at this point, arbitrary functions with the only assumption being that W is symmetric in its arguments $W(r,r') = W(r',r)$. Later in this appendix, we prove that $C_{\lambda\lambda'}$ takes this form in both the $SO(N_f)$ and $Sp(N_f)$ theories. We show that if we take $Z(r) = e^{-\pi W(r,r)}/2\pi$ the following claims are true:

1. ξ satisfies the current correspondence

$$j^{\mu} = \frac{\epsilon^{\mu\nu}}{\sqrt{\pi}}\partial_{\nu}\phi. \tag{A.23}$$

2. ξ satisfies the spatial Heisenberg equations in Eq. A.19.

3. ξ satisfies the canonical anticommutation relations at equal time

$$\{\xi_{\lambda}(r),\xi_{\lambda}(r')\} = 0 \qquad \{\xi_{\lambda}(r),\xi^{\dagger}_{\lambda}(r')\} = \delta_{\lambda\lambda'}\delta(r-r'). \tag{A.24}$$

4. The operator $\bar{\xi}(r)\xi(r)$ is equal to

$$\bar{\xi}(r)\xi(r) = \frac{\mu e^{\gamma}}{2\pi} e^{-F(r)} : \cos\big(2\sqrt{\pi}\phi - \alpha\big) : . \tag{A.25}$$

With these claims proven, we will have shown that the theory for ξ and the theory for ϕ are equivalent provided ϕ obeys the Hamiltonian

$$H = \int_0^{\infty} dr \frac{1}{2}(\dot{\phi}^2 + \phi'^2) + m\frac{\mu e^{\gamma}}{4\pi} e^{-F(r)}(1 - : \cos\big(2\sqrt{\pi}\phi_i + \alpha_i\big) :) - g\dot{\lambda}\phi'. \tag{A.26}$$

It should be noted that, once we have bosonized the theory, the function $W(r, r')$ is unphysical because it cancels in any operator built out of fermion bilinears when translating to normal ordered scalar operators.

$$\xi^{\dagger}_{\lambda}(r)\xi_{\lambda'}(r) \propto Z(r) e^{\pi[\Phi^{-}_{\lambda}(r), \Phi^{+}_{\lambda'}(r)]} \propto e^{-\pi W} e^{\pi W} = 1 \tag{A.27}$$

We now prove the above four claims thus proving bosonization.

A.3.2 Proving the 4 Claims

Claim 1: Current Correspondence

Here we prove the current correspondence in Eq. A.23. We start by noting from the definition in Eq. A.15

$$j^0(r) = \frac{1}{2} \lim_{r \to r'} (\xi^{\dagger}_1(r)\xi_1(r') + \xi^{\dagger}_1(r')\xi_1(r) + \xi^{\dagger}_{-1}(r)\xi_{-1}(r') + \xi^{\dagger}_{-1}(r')\xi_{-1}(r)) \tag{A.28}$$

$$j^1(r) = \frac{1}{2}\lim_{r\to r'}(\xi_1^\dagger(r)\xi_1(r') + \xi_1^\dagger(r')\xi_1(r) - \xi_{-1}^\dagger(r)\xi_{-1}(r') - \xi_{-1}^\dagger(r')\xi_{-1}(r)). \tag{A.29}$$

So we will be interested in the combinations $\xi_\lambda^\dagger(r)\xi_\lambda(r')$ in the $r \to r'$ limit. We can use Eq. A.20 to write in the $r \to r'$ limit.

$$\xi_\lambda^\dagger(r)\xi_\lambda(r') = Z(r)(: e^{-i\sqrt{\pi}(\Phi_\lambda(r')-\Phi_\lambda(r))} : e^{\pi\left[\Phi_\lambda^-(r),\Phi_\lambda^+(r')\right]} \tag{A.30}$$
$$=: e^{-i\sqrt{\pi}(\Phi_\lambda(r')-\Phi_\lambda(r))} : \frac{e^{-\ln(\epsilon - i\lambda(r-r'))}}{2\pi} = \frac{i\lambda}{2\pi(r-r')}(1 + i\sqrt{\pi}(r-r')(\partial_0\phi - \lambda\partial_1\phi))$$

Now, taking the $r \to r'$ symmetric limit,

$$\frac{\xi_\lambda^\dagger(r)\xi_\lambda(r') + \xi_\lambda^\dagger(r')\xi_\lambda(r)}{2} = \frac{\partial_1\phi - \lambda\partial_0\phi}{2\sqrt{\pi}} \tag{A.31}$$

. At which point we can set $r = r'$. Plugging this into Eq. A.28 and A.29, we can see we get the current correspondence in Eq. A.23.

Claim 2: $\tilde{\xi}$ satisfies Eq. A.19

Now let us prove that $\tilde{\xi}$ satisfies Eq. A.19. From Eq. A.20,

$$-i\partial_r\xi_\lambda = -\sqrt{\pi Z(r)}e^{-i\sqrt{\pi}\Phi_\lambda^+}(\partial_r\Phi_\lambda)e^{-i\sqrt{\pi}\Phi_\lambda^-} - \frac{i}{2}\partial_r\ln(Z(r))\xi_\lambda \tag{A.32}$$
$$= -\frac{\sqrt{\pi Z(r)}}{2}\{\partial_r\Phi_\lambda, : e^{-i\sqrt{\pi}\Phi_\lambda} :\} - \frac{i}{2}\partial_r\ln(Z(r))\xi_\lambda$$
$$-\frac{\sqrt{\pi Z(r)}}{2}\left(\left[e^{-i\sqrt{\pi}\Phi_\lambda^+}, \partial_r\Phi_\lambda\right]e^{-i\sqrt{\pi}\Phi_\lambda^-} + e^{-i\sqrt{\pi}\Phi_\lambda^+}\left[\partial_r\Phi_\lambda, e^{-i\sqrt{\pi}\Phi_\lambda^-}\right]\right).$$

It is easy to show that for any two operators A, B whose commutator is a complex number that

$[A, e^B] = [A, B]e^B$ and so,

$$-i\partial_r\xi_\lambda = -\frac{\sqrt{\pi}}{2}\{\partial_r\Phi_\lambda, \xi_\lambda\} - \frac{i}{2}\partial_r \ln(Z(r))\xi_\lambda - i\frac{\pi}{2}\left(\left[\partial_r\Phi^-_\lambda, \Phi^+_\lambda\right] + \left[\Phi^-_\lambda, \partial_r\Phi^+_\lambda\right]\right)\xi_\lambda. \quad \text{(A.33)}$$

This last term can be rewritten

$$\left[\partial_r\Phi^-_\lambda, \Phi^+_\lambda\right] + \left[\Phi^-_\lambda, \partial_r\Phi^+_\lambda\right] = \lim_{r\to r'}(\partial_r + \partial_{r'})\left[\Phi^-_\lambda(r), \Phi^+_\lambda(r')\right]. \quad \text{(A.34)}$$

Using Eq. A.22, this becomes

$$\begin{aligned}&\left[\partial_r\Phi^-_\lambda, \Phi^+_\lambda\right] + \left[\Phi^-_\lambda, \partial_r\Phi^+_\lambda\right] \quad \text{(A.35)}\\ &= \lim_{r\to r'}(\partial_r + \partial_{r'})\left(W(r, r') + \frac{1}{\pi}\ln(\epsilon - i\lambda(r - r'))\right).\end{aligned}$$

The last term is zero since it depends on the combination $r - r'$ and so we find $[\partial_r\Phi^-_\lambda, \Phi^+_\lambda] + [\Phi^-_\lambda, \partial_r\Phi^+_\lambda] = 2W'(r, r)$ and we arrive at

$$-i\partial_r\xi_\lambda = -\frac{\sqrt{\pi}}{2}\{\partial_r\Phi_\lambda, \xi_\lambda\} - \frac{i}{2}\partial_r(\ln(Z(r)) + 2\pi W'(r, r))\xi_\lambda. \quad \text{(A.36)}$$

Since $Z(r) \propto e^{-\pi W(r,r)}$ and $W(r, r') = W(r', r)$, it is easy to $\partial_r \ln(Z(r)) = -2\pi W'(r, r)$ so this second term is zero. The first term can be simplified using Eq. A.23 and we are left with

$$-i\partial_r\xi_\lambda = \frac{\pi}{2}\{j^1 + \lambda j^0, \xi_\lambda\} \quad \text{(A.37)}$$

which for $\lambda = \pm 1$ gives both components of Eq. A.19

Claim 3: Anticommutation Relations

In order to simplify the proof of the commutation relations, let us first prove the following two identities:

$$e^{-\pi[\Phi^-_\lambda(r),\Phi^+_{\lambda'}(r')]} + e^{-\pi[\Phi^-_{\lambda'}(r'),\Phi^+_\lambda(r)]} = 0 \tag{A.38}$$

$$e^{\pi[\Phi^-_\lambda(r),\Phi^+_{\lambda'}(r')]} + e^{\pi[\Phi^-_{\lambda'}(r'),\Phi^+_\lambda(r)]} = Z^{-1}(r)\delta_{\lambda\lambda'}\delta(r-r'). \tag{A.39}$$

Starting with Eq. A.38, we can note from Eq. A.22

$$\pi[\Phi^-_\lambda(r),\Phi^+_{-\lambda}(r')] = \pi W(r,r') - F(r) + \ln\left(\frac{\mu e^\gamma}{2}\right) + \frac{i\lambda\pi}{2}. \tag{A.40}$$

So,

$$e^{\pm\pi[\Phi^-_\lambda(r),\Phi^+_{-\lambda}(r')]} + e^{\pm\pi[\Phi^-_{-\lambda}(r'),\Phi^+_\lambda(r)]} = e^{\pm(\pi W(r,r')-F(r))}\left((\pm i)^\lambda + (\mp i)^\lambda\right) = 0 \tag{A.41}$$

which proves Eq. A.38 and A.39 for $\lambda = -\lambda'$. To prove them for $\lambda = \lambda'$, we again start with Eq. A.22 to see

$$\pi[\Phi^-_\lambda(r),\Phi^+_\lambda(r')] = \pi W(r,r') - \ln(\epsilon - i\lambda(r-r')). \tag{A.42}$$

From which it is easy to see

$$\begin{aligned} e^{\pi[\Phi^-_\lambda(r),\Phi^+_\lambda(r')]} + e^{\pi[\Phi^-_\lambda(r'),\Phi^+_{-\lambda}(r)]} &= 2\pi e^{\pi W(r,r')}\delta(r-r') \\ e^{-\pi[\Phi^-_\lambda(r),\Phi^+_\lambda(r')]} + e^{-\pi[\Phi^-_\lambda(r'),\Phi^+_{-\lambda}(r)]} &= 2\epsilon e^{-\pi W(r,r')} = 0 \end{aligned} \tag{A.43}$$

which now proves Eq. A.38 and A.39 for all λ, λ'.

Now, from Eq. A.38 and A.39, it is very easy to compute the anticommutation relations. Note, we can suppress all factors of $e^{i\alpha}$ here since the commutators in which they don't cancel with their conjugate $e^{-i\alpha}$ are zero. With this in mind

$$\begin{aligned}\{\xi_\lambda(r), \xi_{\lambda'}(r')\} =& Z(r)\{: e^{-i\sqrt{\pi}\Phi_\lambda(r)} :, : e^{-i\sqrt{\pi}\Phi_{\lambda'}(r')} :\} \\ =& Z(r) : e^{-i\sqrt{\pi}(\Phi_\lambda(r)+\Phi_{\lambda'}(r'))} : \left(e^{-\pi[\Phi^-_\lambda(r),\Phi^+_{\lambda'}(r')]} + e^{-\pi[\Phi^-_{\lambda'}(r'),\Phi^+_\lambda(r)]}\right) = 0\end{aligned} \tag{A.44}$$

and

$$\begin{aligned}\{\xi_\lambda(r), \xi^\dagger_{\lambda'}(r')\} =& Z(r)\{: e^{-i\sqrt{\pi}\Phi_\lambda(r)} :, : e^{i\sqrt{\pi}\Phi_{\lambda'}(r')} :\} \\ =& Z(r) : e^{-i\sqrt{\pi}(\Phi_\lambda(r)-\Phi_{\lambda'}(r'))} : \left(e^{\pi[\Phi^-_\lambda(r),\Phi^+_{\lambda'}(r')]} + e^{\pi[\Phi^-_{\lambda'}(r'),\Phi^+_\lambda(r)]}\right) \\ =& Z(r) : e^{-i\sqrt{\pi}(\Phi_\lambda(r)-\Phi_{\lambda'}(r'))} : \frac{\delta_{\lambda\lambda'}\delta(r-r')}{Z(r)} = \delta_{\lambda\lambda'}\delta(r-r')\end{aligned} \tag{A.45}$$

which proves the commutation relations.

Claim 4: Mass Term Correspondence

Next let us prove the correspondence for the mass term in Eq. A.25,At this point, we simply compute

$$\begin{aligned}\bar{\xi}(r)\xi(r) =& Z(r)\left(ie^{i\alpha} : e^{ie^{-i\alpha}:e^{i\sqrt{\pi}\Phi_{-1}(r)}::e^{-i\sqrt{\pi}\Phi_1(r)}:-i\sqrt{\pi}\Phi_1(r)} :: e^{-i\sqrt{\pi}\Phi_{-1}(r)} :\right) \\ =& Z(r)\left(ie^{-i\alpha} : e^{2i\sqrt{\pi}\phi} : e^{\pi\left[\Phi^-_{-1}(r),\Phi^+_1(r)\right]} - ie^{i\alpha} : e^{-2i\sqrt{\pi}\phi} : e^{\pi\left[\Phi^-_1(r),\Phi^+_{-1}(r)\right]}\right)\end{aligned} \tag{A.46}$$

where we have used $\Phi_{-1} - \Phi_1 = 2\phi$. These commutators have a well-defined limit at $r = r'$.

$$\pi \left[\Phi^-_\lambda(r), \Phi^-_{-\lambda}(r)\right] = \pi W(r,r) - F(r) + \ln\left(\frac{\mu e^\gamma}{2}\right) + \frac{i\lambda\pi}{2} \tag{A.47}$$

So,

$$\bar{\xi}(r)\xi(r) = Z(r)\frac{\mu e^{\pi W(r,r)+\gamma-F(2r)}}{2}\left(:e^{i(2\sqrt{\pi}\phi-\alpha)}: + :e^{-i(2\sqrt{\pi}\phi-\alpha)}:\right) \tag{A.48}$$

$$= \frac{\mu e^{\gamma-F(2r)}}{2\pi} :\cos\left(2\sqrt{\pi}\phi - \alpha\right). \tag{A.49}$$

This proves Eq. A.25.

A.3.3 Commutator Computation

The only remaining task is to show that $C_{\lambda\lambda'}$ takes the supposed form in Eq. A.22 for both $SO(N_f)$ and $SU(N_f)$ theories. From Eq. A.20, we can see that $C_{\lambda\lambda'}$ takes the form

$$C_{\lambda,\lambda'}(r,r') = \lim_{t\to t', r\to r'}\left(\int_0^r dx \int_0^{r'} dx' \partial_t \partial_{t'} D(x,t;,x',t') \right. \tag{A.50}$$
$$\left. - \lambda\int_0^{r'} dx' \partial_{t'} D(r,t;x',t') - \lambda'\int_0^r dx \partial_t D(x,t;r',t') + \lambda\lambda' D(r,t;r',t')\right)$$

where $D(r,t;r',t') \equiv [\phi^-(r,t), \phi^+(r',t')]$. Before diving into a computation $C_{\lambda,\lambda'}$, we first give a brief argument that we can compute $C_{\lambda\lambda'}$ by replacing the full propagator D with the equivalent propagator for a free massless scalar D_0. Let us argue this term by term in Eq. A.50. As we will see, the first term will be entirely absorbed into $W(r,r')$ and so will not concern us. If we assume that our theory is perturbative, the full propagator D can be approximated by the propagator to

arbitrarily high accuracy by the free field propagator D_0 in the $t \to t'$ and $r \to r'$ limit and so we can make the replacement in the last term. We can also replace D with D_0 in the middle two terms provided that $\lim_{t\to t'} \partial_t D(r,t;,r',t') = 0$ if $r \neq r'$ so that this integral receives no contribution at finite $x - r'$ (or $r - x'$). To see this it true, note that from time translation and time reversal symmetry, $D(r,t,r',t')$ can only depend on $(t-t')^2$ and thus its time derivative must be 0 or ill-defined when $t = t'$. Because D is the Green's function of our full theory, it must be continuous and smooth when $t \neq t'$ and $r \neq r'$ so this time derivative can only be ill-defined when $r = r'$ and $t = t'$. So we find that $\lim_{t\to t'} \partial_t D(r,t;,r',t') = 0$ when $r \neq r'$ and thus we can replace D with the free scalar propagator D_0 in the middle two terms as well. With these replacements, $C_{\lambda,\lambda'}$ takes the form

$$\lim_{r\to r'} C_{\lambda,\lambda'}(r,r') = \lim_{t\to t', r\to r'} \Bigg(\lambda\lambda' D_0(r,t;r',t') - \lambda \int_0^{r'} dx' \partial_{t'} D_0(r,t;x',t') - \lambda' \int_0^{r} dx \partial_t D_0(x,t;r',t') + \tilde{W}(r,r') \tag{A.51}$$

where,

$$\tilde{W}(r,r') = \int_0^r dx \int_0^{r'} dx' \partial_t \partial_{t'} D(x,t;,x',t'). \tag{A.52}$$

Now, that we have rewritten $C_{\lambda,\lambda'}$ in terms of the free scalar propagator, D_0, we have computational control and we can compute this for the $SO(N_f)$ and $Sp(N_f)$ theories. Because these two theories have different boundary conditions, D_0 will be different for the two theories. We will compute $C_{\lambda,\lambda'}$ in both theories. Before proceeding it is worth commenting on a technical aspect of free, massless scalar theory in 1+1D. These theories contain IR divergences which fortunately can be regulated entirely through normal ordering. Normal ordering necessitates the introduction

of a scale μ with respect to which normal ordering is performed [81]. Thus a theory of free, massless scalar fields in 1+1D must include the specification of a scale μ if it is to be well-defined. This scale μ appears as a "mass" for the scalar field but it should be noted that it is not meant to represent the mass of any particle.

$SO(N_f)$ Theories

The bosonized theory for $SO(N_f)$ theories consists of N_f scalar fields, ϕ_i, the boundary conditions for which can be found by applying the boundary conditions in Eq. 2.30 to the current correspondence in Eq. A.23

$$\partial_r \phi_i(r=0) = 0. \tag{A.53}$$

One can easily see that the free, massless scalar fields with this boundary condition when quantized take the form

$$\phi(r,t) = \int_{-\infty}^{\infty} \frac{dk}{2\pi\sqrt{\omega}} \cos(kr) e^{-i\omega t} a_k + h.c. \tag{A.54}$$

where $\omega = \sqrt{k^2+\mu^2}$ and $a_k(a_k^\dagger)$ are the creation and annihilation operators. From this, we can easily compute D_0

$$\begin{aligned} D_0(r,t;r't') \equiv [\phi^-(r,t), \phi^+(r',t')] &= \int_{-\infty}^{\infty} \frac{dk}{2\pi\omega} e^{-i\omega(t-t')} \cos(kr)\cos(kr') \\ &= \int_{-\infty}^{\infty} \frac{dk}{4\pi\omega} \left(e^{-i(\omega(t-t')-k(r-r'))} + e^{-i(\omega(t-t')-k(r+r'))} \right) \\ &= G_0(r-r', t-t') + G_0(r+r', t-t') \end{aligned} \tag{A.55}$$

where,

$$G_0(\Delta r, \Delta t) \equiv \int_{-\infty}^{\infty} \frac{dk}{4\pi\omega} e^{-i(\omega\Delta t - k\Delta r)} = \frac{1}{2\pi} K_0(\mu\sqrt{\Delta r^2 - (\Delta t - i\epsilon)^2}). \tag{A.56}$$

It is understood that we take the limit of $\epsilon \to 0$ at the end of any computation. Now, we can plug this into Eq. A.50 and compute. Firstly, it is not difficult to show that

$$\lim_{t\to t'} \partial_t G_0(r \pm r', t - t') = -\frac{i\epsilon}{2\pi(\epsilon^2 + (r \pm r')^2)} \left(\mu\sqrt{(r \pm r')^2 + \epsilon^2} K_1(\mu\sqrt{(r \pm r')^2 + \epsilon^2})\right). \tag{A.57}$$

Clearly, this will vanish in the $\epsilon \to 0$ limit unless $r \pm r' = 0$ so we can expand around this point to find

$$\lim_{\epsilon\to 0, t\to t'} \partial_t G_0(r \pm r', t - t') = -\frac{i\epsilon}{2\pi(\epsilon^2 + (r \pm r')^2)} \tag{A.58}$$

which can be quickly integrated

$$\lim_{\epsilon\to 0, t\to t'} \int_0^r dx \partial_t G_0(x \pm r', t - t') = -\frac{i}{2\pi} \left(\arctan\left(\frac{r \pm r'}{\epsilon}\right) - \arctan\left(\frac{\pm r'}{\epsilon}\right)\right). \tag{A.59}$$

This can be greatly simplified by noting that since $r, r' > 0$, in the $\epsilon \to 0$ many of these $\arctan$ factors reduce to $\pm\pi/2$ depending on the sign of the argument. When the dust settles we find

$$\lim_{\epsilon\to 0, t\to t'} \int_0^r dx \partial_t D_0(x, t; r', t') = -\frac{i}{2\pi} \left(\arctan\left(\frac{r - r'}{\epsilon}\right) + \frac{\pi}{2}\right). \tag{A.60}$$

A nearly identical computation shows that

$$\lim_{\epsilon\to 0, t\to t'} \int_0^{r'} dx' \partial_{t'} D_0(r,t;x',t') = -\frac{i}{2\pi}\left(\arctan\left(\frac{r-r'}{\epsilon}\right) - \frac{\pi}{2}\right). \tag{A.61}$$

This combined with the limits

$$\begin{aligned} \lim_{r-r',t-t',\epsilon\to 0} G_0(r-r',t-t') &= -\frac{1}{2\pi}\ln\left(\frac{\mu e^\gamma}{2}\sqrt{(r-r')^2+\epsilon^2}\right) \\ \lim_{r-r',t-t',\epsilon\to 0} G_0(r+r',t-t') &= \frac{K_0(\mu(r+r'))}{2\pi} \end{aligned} \tag{A.62}$$

allows us to write

$$C_{\lambda\lambda'}(r,t;,r',t') = -\frac{\lambda\lambda'}{2\pi}\left(\ln\left(\frac{\mu e^\gamma}{2}\sqrt{(r-r')^2+\epsilon^2}\right) - K_0(\mu(r+r'))\right) \tag{A.63}$$

$$+\frac{i(\lambda+\lambda')}{2\pi}\arctan\left(\frac{r-r'}{\epsilon}\right) - \frac{i(\lambda-\lambda')}{4} + \tilde{W}(r,r). \tag{A.64}$$

Finally, if we make the definition

$$W(r,r') \equiv \tilde{W}(r,r') + \frac{1}{2\pi}\left(\ln\left(\sqrt{(r-r')^2+\epsilon^2}\right) - \ln\left(\frac{\mu e^\gamma}{2}\right) + K_0(\mu(r+r'))\right) \tag{A.65}$$

and expand the $\arctan$ out in terms of logs, one can show that this takes the form

$$C_{\lambda\lambda'}(r,t;,r',t) = -\frac{(1+\lambda)(1+\lambda')}{4\pi}\ln(\epsilon - i(r-r')) - \frac{(1-\lambda)(1-\lambda')}{4\pi}\ln(\epsilon + i(r-r')) \tag{A.66}$$

$$-\frac{1-\lambda\lambda'}{2\pi}\left(K_0(2\mu r) - \ln\left(\frac{\mu e^\gamma}{2\pi}\right)\right) - \frac{i(\lambda-\lambda')}{4} + W(r,r)$$

which can be seen to be exactly the form given in Eq. A.22 with $F(r) = K_0(2\mu r)$.

$Sp(N_f)$ Theories

The $Sp(N_f)$ theories consist of $N_f/2$ families of 2 scalar fields $\phi_{b,i}$ and $\phi_{\ell,i}$. Since the full theory consists of $N_f/2$ identical families, we can focus on one family and drop the i index. We wish to quantize these free, massless fields. In general, we can write them in terms of creation and annihilation operators $a(a^\dagger)$ and $b(b^\dagger)$ for fields ϕ_ℓ and ϕ_b respectively separating out the left and right moving components.

$$\phi_\ell(r,t) = \int_0^\infty \frac{dk}{2\pi\sqrt{2\omega}} e^{-i\omega t}(a_k e^{ikr} + a_{-k}e^{-ikr}) + h.c. \tag{A.67}$$

$$\phi_b(r,t) = \int_0^\infty \frac{dk}{2\pi\sqrt{2\omega}} e^{-i\omega t}(b_k e^{ikr} + b_{-k}e^{-ikr}) + h.c.. \tag{A.68}$$

Note that each scalar field has its own scale μ. On these, we can impose the boundary conditions.

$$\partial_r(\phi_\ell + \phi_b) = 0 \tag{A.69}$$

$$\partial_t(\phi_\ell - \phi_b) = 0 \tag{A.70}$$

derived from combining Eq. 2.30 and A.20. These boundary conditions can easily be seen to enforce

$$a_{-k} = b_k \quad b_{-k} = a_k \tag{A.71}$$

and so we can write our two fields as

$$\phi_\ell(r,t) = \int_0^\infty \frac{dk}{2\pi\sqrt{2\omega}} e^{-i\omega t}(a_k e^{ikr} + b_k e^{-ikr}) + h.c. \tag{A.72}$$

$$\phi_b(r,t) = \int_0^\infty \frac{dk}{2\pi\sqrt{2\omega}} e^{-i\omega t}(b_k e^{ikr} + a_k e^{-ikr}) + h.c.. \tag{A.73}$$

From this, we can compute the propagator for each field, which, because the labels a and b are arbitrary, are identical.

$$D_0(r,t;r',t') = \int_{-\infty}^\infty \frac{dk}{4\pi\omega} e^{-i(\omega(t-t')-k(r-r'))} = G_0(r-r',t-t') \tag{A.74}$$

This is the same propagator as for $SO(N_f)$ theories but without the $G_0(r+r',t-t')$ piece. The computation of $C_{\lambda,\lambda'}$ is then a simplified version of the computation for the $SO(N_f)$ theories and so we simply state the result.

$$C_{\lambda\lambda'}(r,t;,r',t') = -\frac{\lambda\lambda'}{2\pi}\ln\left(\frac{\mu e^\gamma}{2}\sqrt{(r-r')^2+\epsilon^2}\right) \tag{A.75}$$

$$+\frac{i(\lambda+\lambda')}{2\pi}\arctan\left(\frac{r-r'}{\epsilon}\right) - \frac{i(\lambda-\lambda')}{4} + \tilde{W}(r,r) \tag{A.76}$$

If we define

$$W(r,r') \equiv \tilde{W}(r,r') + \frac{1}{2\pi}\left(\ln\left(\sqrt{(r-r')^2+\epsilon^2}\right) - \ln\left(\frac{\mu^\gamma}{2}\right)\right) \tag{A.77}$$

and expand the $\arctan$ our in terms of logs, one can show that this takes the form

$$C_{\lambda\lambda'}(r,t;,r',t) = -\frac{(1+\lambda)(1+\lambda')}{4\pi}\ln(\epsilon - i(r-r')) - \frac{(1-\lambda)(1-\lambda')}{4\pi}\ln(\epsilon + i(r-r')) \tag{A.78}$$

$$+ \frac{1-\lambda\lambda'}{2\pi}\ln\left(\frac{\mu e^{\gamma}}{2\pi}\right) - \frac{i(\lambda-\lambda')}{4} + W(r,r)$$

which can be seen to be exactly the form given in Eq. A.22 with $F(r) = 0$.

Appendix B: CMB Distortions

B.1 A Model

Here we summarize a simple model containing an axion, photon and dark photon where the leading interaction is that given in Eq. 1.3. This model contains a dark sector with a complex scalar Φ a dark sector $U(1)$ gauge boson A_D and two sets of two left handed Weyl fermions ξ, ξ^c, χ and χ^c. These fermions are charged under both electromagnetism and the dark $U(1)$ gauge group with charges shown in Table B.1. The scalar Φ is uncharged under both electromagnetism and the dark $U(1)$.

	Q_{EM}	Q_D
χ	2	2
χ^c	-2	-2
ξ	2	-2
ξ^c	-2	2

Table B.1: The charges for our dark sector fermions. Q_{EM} is the particles electric charge in units of the fundamental electric charge and similarly, Q_D is the particles charge in units of the fundamental dark charge.

In addition to these charges we demand that our model obey a dark charge conjugation symmetry C_D defined by

$$C_D: \qquad A \to A \qquad A_D \to -A_D \qquad \chi \longleftrightarrow \xi \qquad \chi^c \longleftrightarrow \xi^c \qquad \Phi \to \Phi^* \tag{B.1}$$

and a $\mathbb{Z}_8$ symmetry defined by

$$\mathbb{Z}_8 : \qquad \chi \to e^{-i\pi/4}\chi \qquad \xi \to e^{i\pi/4}\xi \qquad \Phi \to e^{i\pi/4}\Phi. \tag{B.2}$$

This $\mathbb{Z}_8$, which is a subgroup of the would be $U(1)_{PQ}$ associated with the axion, may seem troublesome since it corresponds to a chiral rotation of the χ and ξ by $-\pi/4$ and $\pi/4$ respectively and thus should generate an anomalous term through the chiral anomaly. However, with the charges defined in Table B.1, one can show that this is equivalent to a rotation of a single Weyl fermion with charges $Q_{EM} = Q_D = 1$ by an angle of 2π. Our theory should be consistent with the addition of a Dirac fermion with fundamental electric and dark charge and so a chiral rotation of this fermion by 2π must leave the theory invariant. Thus the $\mathbb{Z}_8$ symmetry is nonanomalous. Additionally, this $\mathbb{Z}_8$ symmetry forbids any operators in the potential $V(\Phi)$ that could give the axion a mass up to dimension 8.

With these symmetries in mind, we write all possible terms in our Lagrangian up to dimension 4,

$$\mathcal{L} = \mathcal{L}_{SM} + \mathcal{L}_{kinetic} - V(\Phi) + y(\Phi\chi\chi^c + \Phi^*\xi\xi^c) + h.c.\ , \tag{B.3}$$

where V is the scalar potential, the last term is a Yukawa coupling for the fermions to the scalar and $\mathcal{L}_{kinetic}$ contains all of the kinetic terms for the fermions, Φ, and A_D with the gauge couplings packaged in covariant derivatives.

Now let us suppose that Φ under goes symmetry breaking and obtains a VEV,

$$\Phi(x) = (v + h(x))e^{i\phi(x)/f}. \tag{B.4}$$

Amongst other changes, the Yukawa piece becomes

$$y(\Phi\chi\chi^c + \Phi^*\xi\xi^c) \to y(v+h)(e^{i\phi/f}\chi\chi^c + e^{-i\phi/f}\xi\xi^c). \tag{B.5}$$

These phases can be eliminated by a chiral rotation,

$$\chi \to \chi e^{-i\phi/f} \qquad \xi \to \xi e^{i\phi/f} \tag{B.6}$$

which naturally generates anomalous terms in the Lagrangian due to the chiral anomaly. It is a simple exercise to show that these terms are

$$\begin{aligned}\mathcal{L} \supset \frac{\phi(x)}{16\pi^2 f}\Bigg(&\left((eQ^\chi_{EM})^2 F_{\mu\nu}\tilde{F}^{\mu\nu} + 2ee_D Q^\chi_{EM} Q^\chi_D F_{\mu\nu}\tilde{F}^{\mu\nu}_D + (e_D Q^\chi_D)^2 F^D_{\mu\nu}\tilde{F}^{\mu\nu}_D\right) \\ &- \left((eQ^\xi_{EM})^2 F_{\mu\nu}\tilde{F}^{\mu\nu} + 2ee_D Q^\xi_{EM} Q^\xi_D F_{\mu\nu}\tilde{F}^{\mu\nu}_D + (e_D Q^\xi_D)^2 F^D_{\mu\nu}\tilde{F}^{\mu\nu}_D\right)\Bigg).\end{aligned} \tag{B.7}$$

We get two terms, one for each rotation. Plugging in the charges given in Table B.1 we can easily see that the $F\tilde{F}$ and $F_D\tilde{F}_D$ terms vanish while the $F\tilde{F}_D$ term remains

$$\mathcal{L} \supset \frac{ee_D}{2\pi^2 f}\phi F_{\mu\nu}\tilde{F}^{\mu\nu}_D. \tag{B.8}$$

A similar cancellation happens in the kinetic mixing term. At one loop, as shown in Fig. B.1,

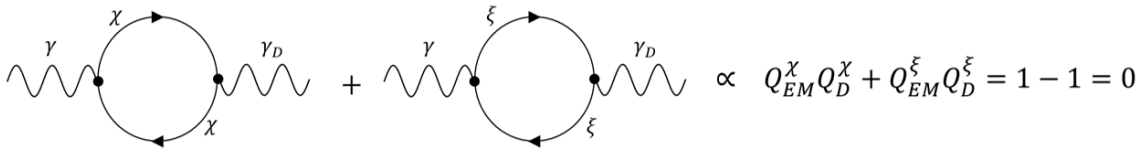

Figure B.1: At 1-loop order, it is easy to see that the diagrams for kinetic mixing exactly cancel due to the χ and ξ particles having opposite charges.

there are two diagrams for the kinetic mixing term which exactly cancel due to the χ and ξ particle's opposite dark charges but identical masses from the Φ VEV. At the heart of this cancellation is the dark charge conjugation symmetry, C_D. This symmetry can easily be seen to forbid the generation of a kinetic mixing terms, which shows the cancellation observed at 1-loop occurs to all orders in perturbation theory.

B.2 Computation of the conversion probability

In this appendix we summarize the details of our conversion probability computation.

B.2.1 Quantized FRW Fields

Here we give a brief description of general massive scalar and vector fields in an expanding FRW background metric $d\tau^2 = a^2(\eta)(d\eta^2 - d\boldsymbol{x}^2)$. We can expand the fields in ladder operators with mode functions $u(\eta, \boldsymbol{k})$ for the scalar and $v^\mu_\lambda(\eta, \boldsymbol{k})$ for the vector where λ is a polarization index.

$$\begin{aligned} \phi(x) &= \int \frac{d^3\boldsymbol{k}}{(2\pi)^3} u(\eta, \boldsymbol{k}) a_{\boldsymbol{k}} e^{i\boldsymbol{k}\cdot\boldsymbol{x}} + h.c. \\ A_\mu(x) &= \int \frac{d^3\boldsymbol{k}}{(2\pi)^3} \sum_\lambda \left(v^\lambda_\mu(\eta, \boldsymbol{k}) a^\lambda_{\boldsymbol{k}} e^{i\boldsymbol{k}\cdot\boldsymbol{x}} + h.c. \right). \end{aligned} \tag{B.9}$$

The mode functions $u(\eta, \boldsymbol{k})e^{i\boldsymbol{k}\cdot\boldsymbol{x}}$ and $v^\lambda_\mu(\boldsymbol{k})e^{i\boldsymbol{k}\cdot\boldsymbol{x}}$ satisfy the equations of motion for scalar and vector fields respectively. The equations of motion are,

$$(\partial_\mu \partial^\mu + 2\mathcal{H}(\eta)\partial_\eta + m^2 a^2(\eta))\phi = 0 \tag{B.10}$$

$$\partial^\mu F_{\mu\nu} + m^2 a^2(\eta) A_\nu = 0. \tag{B.11}$$

To simplify, we make use of the fact that rate at which the universe is expanding ($\mathcal{H} \equiv \partial_\eta \ln(a(\eta))$) is much slower than the rate at which our fields are oscillating, which is roughly the comoving CMB temperature T_{CMB}. In this limit one can show that up to corrections of $\mathcal{O}(\boldsymbol{k}/\mathcal{H})$,

$$u(\boldsymbol{k},\eta) = \frac{e^{-i\int^\eta d\tilde{\eta}\omega^c(\eta,\boldsymbol{k})}}{a(\eta)\sqrt{2\omega^c(\eta)}} \quad \text{and} \quad v_\mu^\lambda(\boldsymbol{k},\eta) = \frac{\epsilon_\mu^\lambda(\boldsymbol{k},\eta) e^{-i\int^\eta d\tilde{\eta}\omega^c(\eta,\boldsymbol{k})}}{\sqrt{2\omega^c(\eta)}}. \tag{B.12}$$

The mode functions are normalized by making sure they reduce to the familiar flat space mode functions in the flat space limit. Here the ϵ_μ^λ represent the 3 different polarizations for the vector

$$\epsilon_L^\mu = \frac{1}{a(\eta)m}\left(|\boldsymbol{k}|, \omega^c(\eta,\boldsymbol{k})\hat{\boldsymbol{k}}\right) \qquad \epsilon_{1,2}^\mu(\boldsymbol{k}) = (0,\boldsymbol{\epsilon}) \quad \text{where} \quad \boldsymbol{k}\cdot\boldsymbol{\epsilon} = 0 \tag{B.13}$$

which are the usual transverse and longitudinal polarizations with $m \to a(\eta)m$. Inserting Eq. B.12 into Eq. B.9 gives Eq. 3.8 and 3.9.

B.2.2 The Interaction Potential

Here we simplify the interaction potentials given in Eq. 3.13. We begin as described, by inserting field operators for the incoming photon and outgoing X particle, and a classical field background for the dark matter field, leading to

$$V_I^\phi(\eta') = -\int \frac{d^3\boldsymbol{x} d^3\boldsymbol{p} d^3\boldsymbol{p}'}{(2\pi)^6 2\sqrt{\omega_\gamma^c(\eta',\boldsymbol{p})\omega_D^c(\eta',\boldsymbol{p}')}} \tag{B.14}$$
$$\frac{\partial_\eta\phi(x)}{f_a}\sum_{\lambda,\lambda'}\left(a_{\boldsymbol{p}',\lambda'}^{\dagger,\gamma_D} a_{\boldsymbol{p},\lambda}^{\gamma} \boldsymbol{\epsilon}_{\lambda'}^*(\boldsymbol{p}')\cdot(i\boldsymbol{p}\times\boldsymbol{\epsilon}_\lambda(\boldsymbol{p}))\, e^{-ix\cdot(p-p')} + ...\right),$$

$$V_I^D(\eta') = \int \frac{d^3\boldsymbol{x} d^3\boldsymbol{p} d^3\boldsymbol{p}'}{(2\pi)^6 2a(\eta')\sqrt{\omega_\gamma^c(\eta',\boldsymbol{p})\omega_\phi^c(\eta',\boldsymbol{p}')}} \tag{B.15}$$
$$\frac{\partial_\eta \boldsymbol{A}_D(x)}{f_a} \cdot \sum_\lambda \left(a^{\dagger,\phi}_{\boldsymbol{p}'} a^\gamma_{\boldsymbol{p},\lambda} \left(i\boldsymbol{p} \times \boldsymbol{\epsilon}_\lambda(\boldsymbol{p})\right) e^{-ix\cdot(p-p')} + ... \right) ,$$

where $x \cdot (p - p')$ is a short hand notation for

$$x \cdot (p - p') \equiv \int^{\eta'} d\tilde{\eta} \left(\omega_\gamma^c(\tilde{\eta}, \boldsymbol{p}) - \omega_X^c(\tilde{\eta}, \boldsymbol{p}') \right) - \boldsymbol{x} \cdot (\boldsymbol{p} - \boldsymbol{p}') , \tag{B.16}$$

and recalling that V^ϕ (V^D) is the interaction potential when the axion (dark photon) is dark matter.

The terms not explicitly written in Eqs. B.14 and B.15 represent different combinations of the ladder operators that will be irrelevant for us since we only wish to consider photons as the initial state and outgoing axions/dark photons in the final state. In the regions of parameter space we will be interested in, the dark matter mass will be smaller than the CMB temperature. Since dark matter is also non-relativistic, this means that the momentum transfer from the dark matter, $\boldsymbol{q} \equiv \boldsymbol{p} - \boldsymbol{p}'$, must be small with respect to the photon momentum,

$$|\boldsymbol{q}| \ll m_{DM} \ll T_{CMB} \sim |\boldsymbol{p}| , \tag{B.17}$$

so we can do an expansion in small $|\boldsymbol{q}|$. To lowest order, this means setting $\boldsymbol{p} = \boldsymbol{p}'$ everywhere. However, we must keep $\boldsymbol{q}$ to linear order in the $x \cdot (p - p')$ order since $\boldsymbol{q} \cdot \boldsymbol{x}$ is not necessarily small since we will be integrating over all $\boldsymbol{x}$.

$$x \cdot (p - p') \approx \int^{\eta'} d\tilde{\eta} \left(\omega_\gamma^c(\tilde{\eta}, \boldsymbol{p}) - \omega_X^c(\tilde{\eta}, \boldsymbol{p}) \right) - \boldsymbol{q} \cdot (\boldsymbol{x} - \hat{\boldsymbol{p}}\eta'). \tag{B.18}$$

Now, the only $\boldsymbol{q}$ dependence is in the exponent and we can shift variables $d^3\boldsymbol{p}' \to d^3\boldsymbol{q}$. After integrating over $d^3\boldsymbol{q}$ we get a delta function $\delta^3(\boldsymbol{x}-\tilde{\boldsymbol{x}})$ where $\tilde{\boldsymbol{x}} = \hat{\boldsymbol{p}}\eta$. [1] This can then be used to eliminate the $d^3\boldsymbol{x}$ integral.

$$V_I^{\phi}(\eta') = -\int \frac{d^3\boldsymbol{p}}{(2\pi)^3} \frac{\partial_\eta \phi(\eta', \tilde{\boldsymbol{x}})}{2f_a\sqrt{\omega_\gamma^c(\eta')\omega_D^c(\eta')}} \sum_{\lambda,\lambda'} \boldsymbol{\epsilon}^*_{\lambda'}(\boldsymbol{p})\cdot(i\boldsymbol{p}\times\boldsymbol{\epsilon}_\lambda(\boldsymbol{p}))\, e^{i\int^{\eta'} d\tilde{\eta}\left(\omega_D^c(\tilde{\eta})-\omega_\gamma^c(\tilde{\eta})\right)} a^{\dagger,\gamma_D}_{\boldsymbol{p},\lambda'} a^{\gamma}_{\boldsymbol{p},\lambda} + ...$$

$$V_I^{D}(\eta') = \int \frac{d^3\boldsymbol{p}}{(2\pi)^3} \frac{\partial_\eta \boldsymbol{A}_D(\eta', \tilde{\boldsymbol{x}})}{2f_a a(\eta')\sqrt{\omega_\gamma^c(\eta')\omega_D^c(\eta')}} \cdot \sum_{\lambda} (i\boldsymbol{p}\times\boldsymbol{\epsilon}_\lambda(\boldsymbol{p}))\, e^{i\int^{\eta'} d\tilde{\eta}\left(\omega_\phi^c(\tilde{\eta})-\omega_\gamma^c(\tilde{\eta})\right)} a^{\dagger,\phi}_{\boldsymbol{p}} a^{\gamma}_{\boldsymbol{p},\lambda} + ... \,.$$

Now, in order to simplify the cross products, we work in the helicity basis for photon polarizations where the following identities hold.

$$i\boldsymbol{p}\times\epsilon_\lambda(\boldsymbol{p}) = \lambda|\boldsymbol{p}|\boldsymbol{\epsilon}_\lambda \qquad \boldsymbol{\epsilon}^*_\lambda\cdot\boldsymbol{\epsilon}_{\lambda'} = \delta_{\lambda\lambda'}, \tag{B.19}$$

where $\lambda = \pm 1$ is the helicity of the photon. This helps simplify the expressions to

$$V_I^{\phi}(\eta') = -\int \frac{d^3\boldsymbol{p}}{(2\pi)^3} \sum_{\lambda} \frac{\lambda|\boldsymbol{p}|\partial_\eta \phi(\eta', \tilde{\boldsymbol{x}})}{2f_a\sqrt{\omega_\gamma^c(\eta')\omega_D^c(\eta')}} e^{i\int^{\eta'} d\tilde{\eta}\left(\omega_D^c(\tilde{\eta})-\omega_\gamma^c(\tilde{\eta})\right)} a^{\dagger,\gamma_D}_{\boldsymbol{p},\lambda} a^{\gamma}_{\boldsymbol{p},\lambda} + ... \tag{B.20}$$

$$V_I^{D}(\eta') = \int \frac{d^3\boldsymbol{p}}{(2\pi)^3} \sum_{\lambda} \frac{\lambda|\boldsymbol{p}|\partial_\eta \boldsymbol{A}_D(\eta', \tilde{\boldsymbol{x}})\cdot\boldsymbol{\epsilon}_\lambda(\boldsymbol{p})}{2f_a a(\eta')\sqrt{\omega_\gamma^c(\eta')\omega_D^c(\eta')}} e^{i\int^{\eta'} d\tilde{\eta}\left(\omega_\phi^c(\tilde{\eta})-\omega_\gamma^c(\tilde{\eta})\right)} a^{\dagger,\phi}_{\boldsymbol{p}} a^{\gamma}_{\boldsymbol{p},\lambda} + ... \,. \tag{B.21}$$

Next, we can look at V_I's matrix elements with momentum eigenstates. After some simplification, it is easy to see these matrix elements take the form,

$$\langle \boldsymbol{k}', (\lambda')|V_I(\eta')|\boldsymbol{k},\lambda\rangle = ia(\eta')\mathcal{M}^{\lambda}(\eta', \boldsymbol{k})(2\pi)^3\delta^3(\boldsymbol{k}-\boldsymbol{k}')(\delta_{\lambda'\lambda}), \tag{B.22}$$

[1] Note that, within the approximations we are using, $\tilde{x}$ is effectively the position of the photon. This is in agreement with the intuition that the transition probability of a photon at a given location depends on the dark matter field at that same location.

where, the (λ') and $(\delta_{\lambda\lambda'})$ are meant to be included if the final state is a dark photon and $\mathcal{M}^{\lambda}(\eta', \boldsymbol{k})$ are given by Eq. 3.15 and 3.16. After dropping the factor $(2\pi)^3\delta^3(\boldsymbol{k} - \boldsymbol{k}')$ due to state normalization, Eq. B.22 can then be inserted into Eq. 3.11 and squared to yield Eq. 3.14-3.16 for the conversion probability.

B.2.3 Spatial Averages

In this section, we argue that in all distortions we are averaging the interaction position $\tilde{\boldsymbol{x}}$ over many de Broglie wavelengths of the dark matter field. This can be easily justified given that we are interested in the monopole spectrum, and thus will average distortions over all directions. This effectively means we will be averaging over many de Broglie wavelengths of the dark matter field. For the pre-recombination distortions, we are interested in the averaged conversion rate as a function of redshift, which depends on the conversion probability between photon scatterings. Thus, we average over all possible photon trajectories, and thus $\tilde{\boldsymbol{x}}$ everywhere in space.

For the free streaming case, one can make a more general argument, which shows that even if one is interested in anisotropies, this averaging is justified. First note that the smallest dark matter mass we consider is 10^{-22} eV, and so the largest de Broglie wavelengths we must consider are $\lesssim 10$ kpc, which is much smaller than the horizon size today. Because the probability conversion depends on the dark matter density, it is dominated at larger redshifts. This means that for photon conversions happening at similar times by directions separated by $\delta\theta \sim 1$, the distance between the transition points is $\sim H_0^{-1} \cdot a_t \gg 10$ kpc, where a_t is the redshift of the transition.

Finally, let us average the dark photon dark matters polarization $\boldsymbol{\epsilon}(\boldsymbol{x})$ over $\boldsymbol{x}$ and derive the replacement given in Eq. 3.20. To start notice that when plugging Eq. 3.16 into Eq. 3.14, There

will be a factor that looks like

$$P \propto \frac{1}{2}\sum_{\lambda} |\boldsymbol{\epsilon}^{\lambda}(\boldsymbol{k}) \cdot \boldsymbol{\epsilon}(\tilde{\boldsymbol{x}})|^2 = \frac{\delta_{ij} - \hat{k}_i \hat{k}_j}{2} \epsilon^i(\tilde{\boldsymbol{x}}) \epsilon^{*j}(\tilde{\boldsymbol{x}}). \tag{B.23}$$

If we call the $\hat{k}$ direction the z direction, then this is simply,

$$\frac{1}{2}\sum_{\lambda} |\boldsymbol{\epsilon}^{\lambda}(\boldsymbol{k}) \cdot \boldsymbol{\epsilon}(\tilde{\boldsymbol{x}})|^2 = \frac{1 - |\epsilon_z(\tilde{\boldsymbol{x}})|^2}{2}. \tag{B.24}$$

Now we average over all possible z-compontents of the dark photons polarization which gives,

$$\frac{1}{2}\sum_{\lambda} |\boldsymbol{\epsilon}^{\lambda}(\boldsymbol{k}) \cdot \boldsymbol{\epsilon}(\tilde{\boldsymbol{x}})|^2 = 1/3. \tag{B.25}$$

Thus the effect of averaging is simply to send $\boldsymbol{\epsilon}^{\lambda}(\boldsymbol{k}) \cdot \boldsymbol{\epsilon}(\tilde{\boldsymbol{x}}) \to 1/\sqrt{3}$ as described in Eq. 3.20.

B.3 Free Distortion Computation

In this section, we will detail the computation of the integral L^2 defined in Eq. 3.22 which we showed can be written as

$$L^2 = \left\langle \left| \frac{L_+ + L_-}{2} \right|^2 \right\rangle_{\beta} \quad \text{where} \quad L_{\pm} = \int_{t_0}^{t} dt' \sqrt{\frac{v_X(t')}{a^3(t')}} e^{i\int^{t'} d\tilde{t}\Omega_{\pm}(t')}. \tag{B.26}$$

The strategy for computing this integral is to break it into intervals in which we can use either the fast oscillation limit or the stationary phase approximation. By choosing the boundaries of these regions appropriately, we can piece these intervals together to get the full result. We first identify any resonant times t_r by solving Eq. 3.27 for t_r. We can then break up the time interval

into sub-intervals as shown in Fig. B.2. We will choose the endpoints of these intervals $t_r \pm \Delta t$

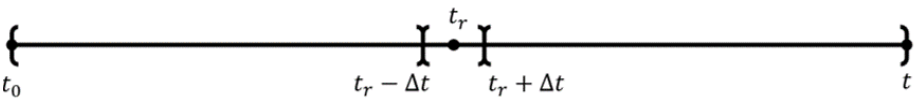

Figure B.2: Breaking the time interval between t and t_0 into sub-intervals that either contain or do not contain a resonance. Note that this is easily extended to the case of multiple resonances. The size of the intermediate integral is greatly exaggerated so that it is visible.

so that the following 3 conditions are true.

1. The stationary phase approximation should be valid everywhere inside the interval $(t_r - \Delta t, t_r + \Delta t)$ such that we can expand the phase of the exponential to second-order

$$\int^{t'} d\tilde{t}\, \Omega_{\pm}(\tilde{t}) \approx \int^{t_r} d\tilde{t}\, \Omega_{\pm}(\tilde{t}) + \dot{\Omega}_{\pm}(t_r)\frac{\Delta t^2}{2}. \tag{B.27}$$

   In order for this approximation to be valid, we must be able to ignore the third-order term. This means we need

$$\Delta t \ll \frac{\dot{\Omega}_{\pm}(t_r)}{\ddot{\Omega}_{\pm}(t_r)} \sim H^{-1}(t_r). \tag{B.28}$$

2. In order to match regions where the stationary phase approximation is valid to regions where the fast oscillation condition is valid, we want both the fast oscillation condition, Eq. 3.26, and the stationary phase approximation to be valid at the endpoints $t_r \pm \Delta t$. Given that the stationary phase approximation is valid, we can write

$$\Omega(t_r \pm \Delta t) \approx \pm\dot{\Omega}(t_r)\Delta t. \tag{B.29}$$

Then since we are near resonance $\dot{\Omega}(t_r) \sim m_{DM}H$ and we find that Eq. 3.26 requires

$$1 \ll m_{DM}\Delta t. \tag{B.30}$$

3. Finally for computational ease, in the stationary phase integrals, we want to be able to take the limit $\Delta t \to \infty$. More precisely this will require that Δt is much larger than the spread of the Gaussian integrand, $\sqrt{\dot{\Omega}_\pm} \sim \sqrt{m_{DM}H}$. We are then able to take the $\Delta t \to \infty$ limit as long as,

$$1 \ll \sqrt{H(t_r)m_{DM}}\Delta t. \tag{B.31}$$

It is easy to see that all 3 conditions are satisfied if

$$1 \gg H(t_r)\Delta t \gg \sqrt{\frac{H(t_r)}{m_{DM}}}. \tag{B.32}$$

Using $m_{DM} \geq 10^{-22}$ eV and $H \leq 10^{-29}$ eV, this translates to $1 \gg H(t_r)\Delta t \gg 10^{-4}$ which is easily satisfied. This shows that we are able to choose endpoints that satisfy all of the 3 conditions. Then from the first and second condition, as shown in Fig. B.2, the total $L_\pm$ can be broken into a series of alternating resonant and fast contributions. However, as we will see, the resonant pieces will always dominate over the fast contributions. We will find that these terms take the form

$$L_\pm = \begin{cases} e^{\mp i\beta(t_0)}L_\pm^{fast}(t_0) & \text{if there are no resonances} \\ \sum_{t_r} e^{\mp i\beta(t_r)}L_\pm^{res}(t_r) & \text{if there are resonances.} \end{cases} \tag{B.33}$$

Where $L_\pm^{fast}(t_0)$ and $L_\pm^{res}(t_r)$ do not depend on the dark matter phase β. This allows us to square and average over the phase which simply eliminates any terms that get a non-trivial phase. This eliminates the cross terms between the L_+ and L_- pieces and any cross terms between different resonances. The end result is

$$L^2 = \frac{|L_+|^2 + |L_-|^2}{4} \quad \text{where} \quad |L_\pm|^2 = \begin{cases} |L_\pm^{fast}(t_0)|^2 & \text{if there are no resonances} \\ \sum_{t_r} |L_\pm^{res}(t_r)|^2 & \text{if there are resonances.} \end{cases} \tag{B.34}$$

Note that L_+ and L_- have different sets of resonant times. Finally, we must compute the fast and resonant integrals to find $|L_\pm^{fast}|$ and $|L_\pm^{res}|$.

B.3.1 Fast limit

In the limit of fast oscillations, we assume $\Omega_\pm \gg H$ for the entire integral. Then we can rewrite Eq. B.26 as

$$L_\pm = \int_{t_0}^{t} dt' \sqrt{\frac{v_X(t')}{a^3(t')}} \frac{1}{i\Omega_\pm(t')} \frac{d}{dt} e^{i\int^{t'} d\tilde{t}\,\Omega_\pm(\tilde{t})}. \tag{B.35}$$

This can then be integrated by parts

$$L_\pm = \sqrt{\frac{v_X(t')}{a^3(t')}} \frac{1}{i\Omega_\pm(t')} e^{i\int^{t'} d\tilde{t}\,\Omega_\pm(\tilde{t})}\Bigg|_{t_0}^{t} - \int_{t_0}^{t} dt' e^{i\int^{t'} d\tilde{t}\,\Omega_\pm(\tilde{t})} \frac{d}{dt}\left(\sqrt{\frac{v_X(t')}{a^3(t')}} \frac{1}{i\Omega_\pm(t')}\right). \tag{B.36}$$

Since the time derivative in the second term is hitting quantities that change on the Hubble scale, this second term represents an $\mathcal{O}(H/\Omega_\pm)$ correction and can be ignored. In the first term, the piece evaluated at t can be ignored due to the scale factor in the denominator. Finally, since

$\dot{\beta} \ll m_{DM}$ we can ignore this term in the denominator, leaving

$$L_{\pm}^{fast} = e^{\mp i\beta(t_0)} \sqrt{\frac{v_X(t_0)}{a^3(t_0)}} \frac{-i}{\Delta\omega(t_0) \pm m_{DM}} e^{i\int^{t_0} d\tilde{t}(\Delta\omega(\tilde{t}) \pm m_{DM})}. \tag{B.37}$$

We see we get the exact β dependence predicted in Eq. B.33. We find then

$$|L_{\pm}^{fast}| = \sqrt{\frac{v_X(t_0)}{a^3(t_0)}} \frac{1}{|\Delta\omega(t_0) \pm m_{DM}|}. \tag{B.38}$$

B.3.2 Resonant Limit

Now we look at the resonant integral.

$$L_{\pm}^{res} = \int_{t_r-\Delta t}^{t_r+\Delta t} dt' \sqrt{\frac{v_X(t')}{a^3(t')}} e^{i\int^{t'} d\tilde{t}\Omega_{\pm}(t')}. \tag{B.39}$$

Expanding the integrand to leading order about the resonance time t_r gives

$$L_{\pm}^{res} = \sqrt{\frac{v_X(t_r)}{a^3(t_r)}} e^{i\int^{t_r} d\tilde{t}\,\Omega_{\pm}(t')} \int_{t_r-\Delta t}^{t_r+\Delta t} dt' e^{i\frac{\dot{\Omega}_{\pm}(t_r)}{2}(t'-t_r)^2}. \tag{B.40}$$

This is simply a Gaussian integral and can be easily computed in the limit $\Delta t \to \pm\infty$.

$$L_{\pm}^{res} = e^{\mp i\beta(t_r)} \sqrt{\frac{2\pi}{i\dot{\Omega}_{\pm}(t_r)} \frac{v_X(t_r)}{a^3(t_r)}} e^{i\int^{t_r} d\tilde{t}\,(\Delta\omega(\tilde{t}) \pm m_{DM})}. \tag{B.41}$$

To leading order, $\dot{\Omega}_{\pm}(t_r) = \dot{\Delta\omega}(t_r)$. The only remaining β dependence is in the phase. We then find

$$|L_{\pm}^{res}| = \sqrt{\frac{2\pi}{|\dot{\Delta\omega}(t_r)|}\frac{v_X(t_r)}{a^3(t_r)}}. \tag{B.42}$$

Combining this result with Eq. B.38 and Eq. B.34 and inserting into Eq. 3.21 yields 3.28.

B.4 Pre-recombination Distortion Computation

Here we give some of the details of the pre-recombination distortion. First, we describe how to use the probabilities given in Eq. 3.21 to compute the rate of photon conversion in Eq. 3.33. Second, we describe the Green's function method for using this rate to compute the distortions in different eras.

B.4.1 Photon Conversion rate

Here we will give the details of computing the conversion rate for photons into particle X given in Eq. 3.32. Because the photons are not free streaming, our integral is over a small time interval, τ, with respect to the expansion rate H. Therefore, quantities which depend on time through the expansion of the universe are approximately constant. We then can write,

$$P(\boldsymbol{k}, t_0, t_0+\tau) = \frac{\rho_{DM}^0 v_X(a(t_0))}{8 f_a^2 a^3(t_0)}\left|\ell_+ + \ell_-\right|^2 \quad \text{where} \quad \ell_{\pm} = \int_0^{\tau} dt e^{i\Omega_{\pm}(a(t_0))(t+t_0)}. \tag{B.43}$$

This can be easily integrated.

$$\ell_{\pm} = 2e^{i\Omega_{\pm}(t_0+\tau/2)}\frac{\sin(\Omega_{\pm}\tau/2)}{\Omega_{\pm}}. \tag{B.44}$$

Now we will square this and average over the dark matter phase β as discussed in Appendix B.2.3. From the $\Omega_\pm$ in the exponential, we get a factor of $e^{\mp i\beta(t_0+\tau/2)}$. Everywhere else we can ignore β because it is sub-leading. Then just as for the free streaming distortion, the phase averaging eliminates the cross terms between ℓ_+ and ℓ_-. This gives,

$$\langle P(\boldsymbol{k}, t_0, t_0+\tau)\rangle_\beta = \frac{\rho^0_{DM} v_X(a)}{2f_a^2 a^3}\left(\frac{\sin^2((\Delta\omega + m_{DM})\tau/2)}{(\Delta\omega + m_{DM})^2} + \frac{\sin^2((\Delta\omega - m_{DM})\tau/2)}{(\Delta\omega - m_{DM})^2}\right).$$

Finally, one can plug this into Eq. 3.32 and evaluate that integral analytically to get Eq. 3.33.

B.4.2 Green's Function Method

Here we present the Green's function for the different eras used in Eq. 3.29 and explain how to compute the parameters $\bar{\mu}$, $\bar{\mu}_t$, y_t and y in Eq 3.2. The Green's functions used are taken from Ref. [85] for the μ and y era and from Ref. [87] for the $\mu - y$ transition era and modified by absorbing and moving a few factors to fit with the definition in Eq 3.29. To start let us define the temperature shift function $\mathcal{T}(x)$, the μ distortion shape $M(x)$, and the y distortion shape $Y(x)$

$$\mathcal{T}(x) = \frac{xe^x}{(e^x-1)} \qquad M(x) = \mathcal{T}(x)\left(\alpha_\mu - \frac{1}{x}\right) \qquad Y(x) = \mathcal{T}(x)\left(x\frac{e^x+1}{e^x-1} - 4\right), \quad \text{(B.45)}$$

where $\alpha_\mu = \zeta(2)/3\zeta(3) \approx 0.456$

μ Era

For the μ era, the Green's function takes the form

$$G_\mu(x, x', a) = 1.4\left(1 - \frac{x_0}{x'}\right)\bar{\rho}(x')J^*(a)M(x) \quad \text{(B.46)}$$

Where $x_0 = \frac{4\zeta(3)}{\zeta(2)} \approx 3.6$, and $\bar{\rho}(x') = \frac{15}{\pi^4}\frac{x^3}{e^x - 1}$ is the unit-normalized blackbody energy spectrum. $J^*(a)$ is called the visibility function and captures how inefficient bremsstrahlung and double Compton scattering are at changing the number density. $J^*(a)$ goes to 0 for $a \ll 10^{-6}$ and quickly goes to zero at early times. Its analytic form can be found in Eq. 13 of Ref. [85]. Note that the $M(x)$ factors out completely and we can write the distortion as

$$\delta(x) = \bar{\mu} M(x) \quad \text{where} \quad \bar{\mu} = 1.4 \int dx' \frac{da}{aH(a)} J^*(a) \left(1 - \frac{x_0}{x'}\right) \bar{\rho}(x') \Gamma_{\gamma \to X}(x', a), \tag{B.47}$$

where the a integral runs from 0 to $a = 3.3 \cdot 10^{-6}$.

μ-y Transition Era

The Green's function for the transition era is similar to that of the μ era with the addition of a y-distortion piece.

$$G_t(x, x', a) = \left(1 - \frac{x_0}{x'}\right) \bar{\rho}(x') \left(1.4 J^*(a) J_\mu(a) M(x) + \frac{1}{4} J_y(a) Y(x)\right). \tag{B.48}$$

The additional factors J_μ and J_y smoothly transition the Green's function from having mostly μ distortion at early times in the era to mostly y- distortions late in the era. Their analytical form can be found in Eq. 5 of Ref. [87]. Much like in the μ era we can write this distortion as

$$\delta(x) = \bar{\mu}_t M(x) + y_t Y(x), \tag{B.49}$$

where

$$\bar{\mu}_t = 1.4 \int dx' \frac{da}{aH(a)} J^*(a) J_\mu(a) \left(1 - \frac{x_0}{x'}\right) \bar{\rho}(x') \Gamma_{\gamma \to X}(x', a) \tag{B.50}$$

$$y_t = \frac{1}{4}\int dx' \frac{da}{aH(a)} J_y(a) \left(1 - \frac{x_0}{x'}\right) \bar{\rho}(x') \Gamma_{\gamma\to X}(x', a) \tag{B.51}$$

and the a integral runs over the whole transition era from $a = 3.3 \cdot 10^{-6}$ to $a = 2 \cdot 10^{-5}$.

y Era

The Green's function for the y era contains two terms. One to describe the Doppler smearing of the removed photons, and another to describe the pure y-distortion.

$$G_y(x, x', a) = \bar{\rho}(x') \left(\left(1 - \frac{e^{(\alpha+\beta)y_\gamma(a)}}{1 + x' y_\gamma(a)}\right) \cdot \frac{Y(x)}{4} + \frac{e^{-(\ln(x(1+x'y_\gamma(a))/x') - \alpha y_\gamma(a))^2/4\beta y_\gamma}}{x'\sqrt{4\pi\beta y_\gamma(a)}} \right),$$

where $y_\gamma(a)$ is the Compton y parameter defined as

$$y_\gamma(a) \equiv \int_a^1 \frac{da'}{a'H(a')} \frac{T(a')}{m_e \lambda_\gamma(a')} \tag{B.52}$$

and α and β are defined as

$$\alpha = \frac{3 - 2f(x')}{\sqrt{1 + x' y_\gamma(a)}} \quad \beta = \frac{1}{1 + x' y_\gamma(a)(1 - f(x'))} \quad \text{where} \quad f(x') = e^{-x'}\left(1 + \frac{x'^2}{2}\right). \tag{B.53}$$

By definition y_γ quantifies the efficiency of Compton scattering to redistribute energy and is thus $\mathcal{O}(1)$ at the start of the y era and quickly falls to be much less than 1. We can write the distortion as

$$\delta(x) = yY(x) + \delta_{Doppler}(x), \tag{B.54}$$

where

$$y = \frac{1}{4}\int dx' \frac{da}{aH(a)} \bar{\rho}(x') \left(1 - \frac{e^{(\alpha+\beta)y_\gamma(a)}}{1 + x' y_\gamma(a)}\right) \Gamma_{\gamma\to X}(x', a) \tag{B.55}$$

$$\delta_{Doppler}(x) = \int dx' \frac{da}{aH(a)} \frac{e^{-(\ln(x(1+x'y_\gamma(a))/x') - \alpha y_\gamma(a))^2/4\beta y_\gamma}}{x'\sqrt{4\pi\beta y_\gamma(a)}} \Gamma_{\gamma\to X}(x', a). \tag{B.56}$$

Here the a integral runs from $a = 2 \cdot 10^{-5}$ to the time of recombination at a_*.

Appendix C: Supernova Constraints

C.1 Computational Details

In this appendix, we provide details on how to calculate the averaged cross-sections used in the constraints. First, we define some notation to simplify the calculations. We will be frequently integrating over final states, for which we will use the shortened notation

$$\int d\Pi_f(p_1, p_2, ...p_n) \equiv \int \prod_{j=1}^{n} \frac{d^3\boldsymbol{p}_j}{(2\pi)^3 2E_j} (2\pi)^4 \delta^4(q - \sum_{j=1}^{n} p_j). \tag{C.1}$$

We use the bracket notation to refer to a thermal average over initial states A and B. For some general function $g(\boldsymbol{p}_A, \boldsymbol{p}_B)$ of these momenta, this average is defined as

$$\langle g(\boldsymbol{p}_A, \boldsymbol{p}_B) \rangle \equiv \int \frac{d^3\boldsymbol{p}_A d^3\boldsymbol{p}_B f_A(E_A, T, \mu_A) f_B(E_B, T, \mu_B)}{(2\pi)^6 n_A n_B} g(\boldsymbol{p}_A, \boldsymbol{p}_B), \tag{C.2}$$

where

$$n_{A,B} = \int \frac{d^3\boldsymbol{p}_{A,B} f_{A,B}(E_{A,B}, T, \mu_{A,B})}{(2\pi)^3} \qquad f(E, T, \mu) = \frac{g}{\exp((E-\mu)/T) \mp 1}. \tag{C.3}$$

In order to capture kinematic features of most of our processes we define two functions α and β as follows,

$$\alpha(s, m_1, m_2) \equiv 1 + \frac{m_1^2 - m_2^2}{s} \qquad \beta(s, m_1, m_2) \equiv \sqrt{1 - \frac{2(m_1^2 + m_2^2)}{s} + \frac{(m_1^2 - m_2^2)^2}{s^2}}. \quad \text{(C.4)}$$

Physically, in the center of mass frame of two particles with center of mass energy $\sqrt{s}$, the energy and momentum of the first particle are $E_1 = \frac{\sqrt{s}}{2}\alpha(s, m_1, m_2)$ and $|\boldsymbol{p}| = \frac{\sqrt{s}}{2}\beta(s, m_1, m_2)$, with similar expressions for the second particle.

C.1.1 Dark Photon and Axion Production Emissivities

In this section we give the details of the three emissivities in Eq. 4.5 and the emissivity in Eq. 4.7. We start with Eq. 4.2. As a convention, in all processes, the initial momenta will be indexed by capital letters while the final momenta will be indexed with a number. p_1 and p_2 represent the axion and dark photon momentum respectively. k will be the momentum of the photon that produces the axion and dark photon and q will be the total momentum. We will see that the matrix element for all processes can be factorized as

$$i\mathcal{M}^X = i\mathcal{M}^X_\mu \mathcal{A}^\mu \quad \text{where} \quad \mathcal{A}^\mu = \frac{\epsilon^{\mu\nu\alpha\beta}}{f_a} k_\nu {p_2}_\alpha \epsilon^D_\beta. \quad \text{(C.5)}$$

The label X on $\mathcal{M}^X_\mu$ will label the process, taking values A for annihilation, B for bremsstrahlung, C for Compton and P for plasmon decay. The factor $\mathcal{A}_\mu$ contains all of the matrix element's dependence on the axion and dark photon final states. Writing our matrix element in this way allows us to factor out our final state phase space integral into two and write Eq. 4.2 as two

separate integrals,

$$\int d\Pi_f(p_1,p_2,p_3,...)|\mathcal{M}^X|^2(E_1+E_2) = \tag{C.6}$$
$$\left(\int d\Pi_f(k,p_3,...)\frac{d(k^2)}{2\pi}k^0\mathcal{M}^X_\mu\mathcal{M}^{X*}_{\ \ \nu}\right)\left(\int d\Pi_f(p_1,p_2)\mathcal{A}^\mu\mathcal{A}^{*\nu}\right).$$

We now have one factor that contains all of the process-dependent information contained in $\mathcal{M}^X_\mu$ and a second piece that contains all of the dependence on the axion and dark photon momentum. This second piece can be computed immediately,

$$\int d\Pi_2(p_1,p_2)\mathcal{A}^\mu\mathcal{A}^{*\nu} = \frac{k^4\beta^3(k^2,m_a,m_D)}{48\pi f_a^2}\left(\frac{k^\mu k^\nu}{k^2}-\eta^{\mu\nu}\right). \tag{C.7}$$

We know that for every process (except plasmon decay) $k^\mu\mathcal{M}^X_\mu = 0$. So the first term doesn't contribute and we get a simple expression for the emissivity of $2\to N$ processes

$$\dot{\epsilon} = n_A n_B\left\langle\frac{1}{2E_A 2E_B}\int d\Pi_f(k,p_3,...)\frac{d(k^2)}{2\pi}k^0(-|\mathcal{M}^X|^2)\frac{k^4\beta^3(k^2,m_a,m_D)}{48\pi f_a^2}\right\rangle. \tag{C.8}$$

In each process, we must identify the correct portion of the matrix element $\mathcal{M}^X_\mu$ and insert it into this equation.

Annihilation

Following the first diagram from Fig. 4.1, the matrix element for the annihilation process is

$$i\mathcal{M} = \bar{v}(p_B)(ie\gamma^\mu)u(p_A)\left(\frac{-ig_{\mu\nu}}{k^2}\right)\left(\frac{i\epsilon^{\alpha\nu\beta\sigma}}{f_a}k_\alpha(p_2)_\beta\epsilon^*_\sigma(p_2)\right). \tag{C.9}$$

Comparing this with Eq. C.5, we can identify,

$$\mathcal{M}^A_\mu = \frac{-e}{q^2}\bar{v}(p_B)\gamma_\mu u(p_A)\,, \tag{C.10}$$

from which we find

$$\dot{\epsilon}_a = \frac{\alpha_e}{24 f_a^2} n_{e^+} n_{e^-} \left\langle (E_A + E_B)\frac{s+2m_e^2}{2E_A E_B}\beta^3(s, m_a, m_D)\right\rangle . \tag{C.11}$$

Finally we define the factor

$$Q^a(m_a, m_D, T, \mu_e) \equiv \left\langle \frac{(E_A+E_B)}{\langle E_A + E_B\rangle}\frac{s+2m_e^2}{2E_A E_B}\beta^3(s, m_a, m_D)\right\rangle \tag{C.12}$$

so that we may simply write

$$\dot{\epsilon}_a = \frac{\alpha_e}{24 f_a^2} n_{e^+} n_{e^-} \langle E_{tot}\rangle\, Q^a\,, \tag{C.13}$$

where $E_{tot} = E_A + E_B$. It is worth nothing that in the limit $m_D = m_a = m_e = 0$, $Q^a = 1$. So, given that electrons and positrons are dominantly relativistic in the supernova, Q^a is $\mathcal{O}(1)$ for small m_a and m_D.

Nuclear Bremsstrahlung

In the soft radiation approximation, there are two diagrams which contribute to the amplitude for bremsstrahlung production:

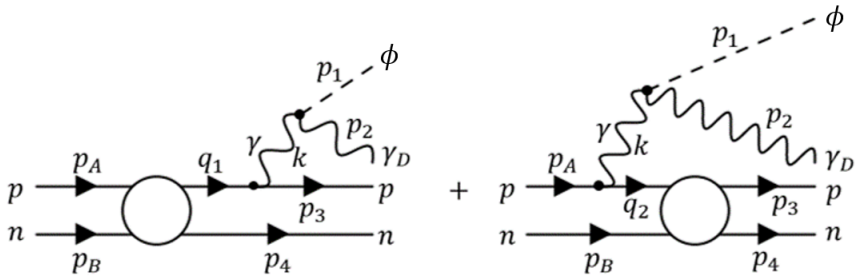

In order to write down the matrix element for this process, we define a Dirac matrix Γ_{pn} by

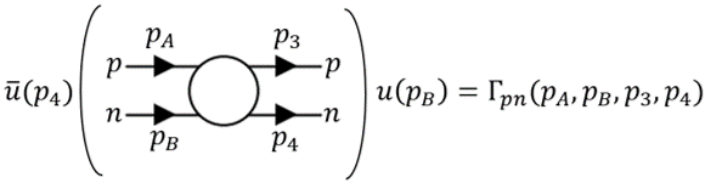

so that the amplitude for proton-neutron scattering can be written as

$$i\mathcal{M}_{pn\to pn} = \overline{u}(p_3)\Gamma_{pn}(p_A, p_B, p_3, p_4)u(p_A). \tag{C.14}$$

We can then write down the matrix element for our bremsstrahlung process

$$i\mathcal{M} = -\frac{ie}{k^2}\overline{u}(p_3)J^\mu u(p_A)\mathcal{A}_\mu(k, p_2), \tag{C.15}$$

where

$$J^\mu = \gamma^\mu\left(\frac{\not{q}_1 + m_N}{q_1^2 - m_N^2}\right)\Gamma_{pn}(p_A, p_3) + \Gamma_{pn}(p_A, p_3)\left(\frac{\not{q}_2 + m_N}{q_2^2 - m_N^2}\right)\gamma^\mu. \tag{C.16}$$

So, we can identify the portion of the matrix element $\mathcal{M}_B^\mu$ as

$$\mathcal{M}_B^\mu = -\frac{e}{k^2}\overline{u}(p_3)J^\mu u(p_A). \tag{C.17}$$

Because we are working in the soft radiation approximation we take $|\boldsymbol{k}| \ll |\boldsymbol{p}|$, where $\boldsymbol{p}$ is any of the nucleon momenta in the process. With that we get a simplified expression for $\mathcal{M}_B^\mu$,

$$\mathcal{M}_B^\mu = -e\mathcal{M}_{pn} j^\mu \quad \text{where} \quad j^\mu = 2\left(\frac{p_3^\mu}{k^2 + 2k\cdot p_3} + \frac{p_A^\mu}{k^2 - 2k\cdot p_A}\right) \tag{C.18}$$

We can then easily square this and sum over the remaining final spins and average over the initial spins. Using the fact that the nuclei are non-relativistic and expanding in their velocities we find

$$\overline{|\mathcal{M}_B|^2} = -\frac{e^2}{k^4}\overline{|\mathcal{M}_{pn}|^2} j^\mu j_\mu \quad \text{where} \quad j^\mu j_\mu = \frac{|\boldsymbol{p}_A - \boldsymbol{p}_3|^2}{(m_N k^0)^2}\left(1 - \left(\frac{|\boldsymbol{k}|}{k^0}\right)^2 \cos^2(\theta)\right) \tag{C.19}$$

Next, we insert this into Eq. C.8,

$$\begin{aligned}\dot{\epsilon}_B = n_n n_p \Bigg\langle \frac{1}{2E_A 2E_B}\int \frac{d(k^2)}{2\pi} d\Pi_3(p_3, p_4, p_k) k_0 e^2 \overline{|\mathcal{M}_{pn}|^2} \\ \times \frac{|\boldsymbol{p}_A - \boldsymbol{p}_3|^2}{(m_N k^0)^2}\left(1 - \left(\frac{|\boldsymbol{k}|}{k^0}\right)^2 \cos^2(\theta)\right)\left(\frac{\beta^3(k^2, m_a, m_D)}{48\pi f_a^2}\right)\Bigg\rangle\end{aligned} \tag{C.20}$$

The remaining phase space integral will contain a delta function $\delta^4(p_A + p_B - p_3 - p_4 - k)$. Once again, we use the soft photon approximation to simplify and we ignore the photon momentum k in the delta function. However, we must ensure that the photon energy is less than the center of mass energy of the nuclei, and so we impose,

$$\delta^4(p_A + p_B - p_3 - p_4 - k) \to \delta^4(p_A + p_B - p_3 - p_4) e^{-k^0/T}. \tag{C.21}$$

This condition could have been achieved with a hard cutoff on the photon energy [71], however the exponential simplifies the computation and leads to similar results (see e.g. [73, 93]). This

substitution also allows us to factor the emissivity into two separate factors,

$$\dot{\epsilon}_B = n_n n_p \left\langle \frac{1}{2E_A 2E_B} \int \Pi_3(p_3, p_4) \frac{|\boldsymbol{p}_A - \boldsymbol{p}_3|^2}{m_N^2} \overline{|\mathcal{M}_{pn}|^2} \right\rangle \tag{C.22}$$
$$\times \left(\int \frac{d(k^2) d^3k}{(2\pi)^4 2k_0} k_0 \frac{e^2 e^{-k^0/T}}{(k^0)^2} \left(1 - \left(\frac{|\boldsymbol{k}|}{k^0} \right)^2 \cos^2(\theta) \right) \left(\frac{\beta^3(k^2, m_a, m_D)}{48\pi f_a^2} \right) \right).$$

The first factor can be seen to be proportional to the momentum transfer cross section for $pn \to pn$ scattering,

$$\frac{1}{2E_A 2E_B} \int \Pi_3(p_3, p_4) \frac{|\boldsymbol{p}_A - \boldsymbol{p}_3|^2}{m_N^2} \overline{|\mathcal{M}_{pn}|^2} = v_{mol} \frac{|\boldsymbol{p}_A|^2}{m_N^2} \sigma_{pn}^t \equiv \Sigma_{pn} \,, \tag{C.23}$$

where,

$$\sigma_{pn}^t = \int d\Omega (1 - \cos(\theta)) \frac{d\sigma_{pn}}{d\Omega} \,. \tag{C.24}$$

The second factor in Eq. C.23 can be simplified significantly by performing the angular integrals and changing integration variables from k^2 and $\boldsymbol{k}$ to k^0 and $v = |\boldsymbol{k}|/k^0$. The result is,

$$\int \frac{d(k^2) d^3k}{(2\pi)^4 2k_0} k_0 \frac{e^2 e^{-k^0/T}}{(k^0)^2} \left(1 - \left(\frac{|\boldsymbol{k}|}{k^0} \right)^2 \cos^2(\theta) \right) \left(\frac{\beta^3(k^2, m_a, m_D)}{48\pi f_a^2} \right) \tag{C.25}$$
$$= \frac{\alpha_e}{12 f_a^2} \int \frac{dk^0 dv}{4\pi^3} k^{0\,2} e^{-k^0/T} v^2 \left(1 - \frac{v^2}{3} \right) \beta^3(k_0^2(1 - v^2), m_a, m_D).$$

This integral can be computed exactly in the massless dark photon and axion limit,

$$\frac{\alpha_e}{12 f_a^2} \int \frac{dk^0 dv}{4\pi^3} k^{0\,2} e^{-k^0/T} v^2 \left(1 - \frac{v^2}{3} \right) = \frac{\alpha_e T^3}{90\pi^3 f_a^2}. \tag{C.26}$$

With this in mind we can write this second factor as $\frac{\alpha_e T^3}{90\pi^3 f_a^2} Q^b$, where

$$Q^b(m_a, m_D, T) = \frac{15}{8T^3} \int dk_0 dv e^{-k_0/T} k_0^2 v^2 \left(1 - \frac{v^2}{3}\right) \beta^3(k_0^2(1-v^2), m_a, m_D). \tag{C.27}$$

Note that once again, $Q^b = 1$ for $m_a = m_D = 0$. The final expression for the emissivity is

$$\dot{\epsilon}_b = \frac{\alpha_e T^3}{90\pi^3 f_a^2} n_p n_n \langle \Sigma_{pn} \rangle \, Q^b(m_a, m_D, T). \tag{C.28}$$

Compton

There are two relevant diagrams for the Compton scattering process,

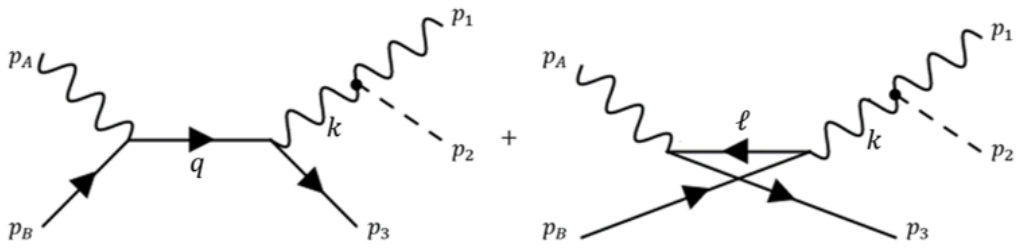

The matrix element is

iM=-ie^2 $\bar{u}(p_3)\left(\frac{\gamma_\mu(\not{q}+m_e)\gamma^\nu}{q^2-m_e^2}+\frac{\gamma^\nu(\not{\ell}+m_e)\gamma_\mu}{\ell^2-m_e^2}\right)u(p_B)\epsilon_\nu(p_A)\mathcal{A}_\nu(k,p_2).$ So we can identify the piece $\mathcal{M}_\mu^C$ as

$$\mathcal{M}_\mu^C = \frac{-ie^2}{k^2} \bar{u}(p_3) \left(\frac{\gamma_\mu(\not{q} + m_e)\gamma^\nu}{q^2 - m_e^2} + \frac{\gamma^\nu(\not{\ell} + m_e)\gamma_\mu}{\ell^2 - m_e^2}\right) u(p_B)\epsilon_\nu(p_A). \tag{C.29}$$

Using this matrix element, and after some algebra we find

$$\dot{\epsilon}_C = \frac{\alpha_e^2}{6 f_a^2} n_{e^-} n_\gamma \left\langle \frac{1}{2E_A E_B} \int d(k^2) \beta^3(k^2, m_a, m_D) \int d\Pi_2(p_3, k) k^0 E(s, t, m_e, k^2) \right\rangle \tag{C.30}$$

where $t = l^2$, and

$$E(s,t,m_e,k^2) = \left((2m_e^2+k^2)\left(m_e^2\left(\frac{1}{s-m_e^2}+\frac{1}{t-m_e^2}\right)^2 + \left(\frac{1}{s-m_e^2}+\frac{1}{t-m_e^2}\right) - \frac{k^2}{(s-m_e^2)(t-m_e^2)}\right) - \frac{1}{2}\left(\frac{t-m_e^2}{s-m_e^2}+\frac{s-m_e^2}{t-m_e^2}\right)\right).$$

After doing the integral over final states $d\Pi_2$, the end result is

$$\dot{\epsilon}_C = \frac{\alpha_e^2}{24\pi f_a^2} n_{e^-} n_\gamma \left\langle \frac{1}{2E_A E_B}\int d(k^2)\beta^3(k^2,m_a,m_D)\left(\left(\frac{s+m_e^2}{s-m_e^2}E_A - E_B\right)R_1 + \left(\frac{k^2-2m_e^2}{s-m_e^2}E_A + E_B\right)R_0\right)\right\rangle , \tag{C.31}$$

where,

$$R_0 = \left(\frac{2s(2m_e^2+k^2)}{(s-m_e^2)^2}\left(\beta(s,m_e,\sqrt{k^2}) - \alpha(s,m_e,\sqrt{k^2})\text{arctanh}\left(\frac{\beta(s,m_e,\sqrt{k^2})}{\alpha(s,m_e,\sqrt{k^2})}\right)\right)\right. \tag{C.32}$$

$$\left. + \frac{\alpha(s,m_e,\sqrt{k^2})\beta(s,m_e,\sqrt{k^2})}{4} + \text{arctanh}\left(\frac{\beta(s,m_e,\sqrt{k^2})}{\alpha(s,m_e,\sqrt{k^2})}\right)\right) \tag{C.33}$$

$$R_1 = \left(\frac{2s(2m_e^2+k^2)}{(s-m_e^2)^2}\left(\frac{m_e^2}{s}\text{arctanh}\left(\frac{\beta(s,m_e,\sqrt{k^2})}{\alpha(s,m_e,\sqrt{k^2})}\right) - \frac{\alpha(s,m_e,\sqrt{k^2})\beta(s,m_e,\sqrt{k^2})}{4}\right)\right. \tag{C.34}$$

$$\left. + \frac{\beta^3(s,m_e,\sqrt{k^2})}{6} + \frac{\beta(s,m_e,\sqrt{k^2})}{2}\left(1+\frac{m_e^2}{s}\right)\right). \tag{C.35}$$

The integral over k^2 runs from $(m_a+m_D)^2$ to $(\sqrt{s}-m_e)^2$. Unlike the other two processes, the

$m_a = m_D = 0$ limit does not lead to a simple expression. However, we may define

$$Q^c = \left\langle \frac{s}{2E_A E_B} \int \frac{d(k^2)}{s} \beta^3 \left(\left(\frac{s + m_e^2}{s - m_e^2} \frac{2E_A}{\langle E_{tot} \rangle} - \frac{2E_B}{\langle E_{tot} \rangle} \right) R_1 + \left(\frac{k^2 - 2m_e^2}{s - m_e^2} \frac{2E_A}{\langle E_{tot} \rangle} + \frac{2E_B}{\langle E_{tot} \rangle} \right) R_0 \right) \right\rangle \tag{C.36}$$

so we get,

$$\dot{\epsilon}_C = \frac{\alpha_e^2}{48\pi f_a^2} n_{e^-} n_\gamma \langle E_{tot} \rangle Q^c(m_a, m_D, T, \mu_e). \tag{C.37}$$

Q^c is still roughly $\mathcal{O}(1)$ in the limit $m_a = m_D = 0$ since $E_A \approx \langle E_{tot} \rangle / 2$.

Plasmon Decay

From the diagram in Fig. 4.2, we can easily write the matrix element for plasmon decay as:

$$i\mathcal{M} = -i\epsilon_\mu^P(k)\mathcal{A}^\mu \tag{C.38}$$

Where ϵ_μ^P is the plasmon polarization. If we square this and sum/average over final/initial spins and integrate over final states using the results of Eq. C.7, we can get

$$\int d\Pi_2(p_1, p_2)|\mathcal{M}|^2 = \left(\frac{k^4 \beta^3(k^2, m_a, m_D)}{48\pi f^2} \right) \left(\sum \epsilon_\mu^P(k) \epsilon^{*P}_\nu(k) \right) \left(\frac{k^\mu k^\nu}{k^2} - \eta^{\mu\nu} \right). \tag{C.39}$$

We will compute the matrix element of longitudinally polarized plasmons and transversely polarized plasmons separately since their dispersion relations and field normalizations are different. The polarizations and dispersion relations are taken from Ref. [88]. The polarizations are

$$\epsilon_\mu^L = \frac{\omega_\ell}{|\boldsymbol{k}|} \sqrt{Z_\ell(k)}(1, \mathbf{0}) \quad \epsilon_\mu^T = \sqrt{Z_t(k)}(0, \boldsymbol{\epsilon}_T). \tag{C.40}$$

Where $\boldsymbol{\epsilon}_T \cdot \boldsymbol{k} = 0$. The dispersion relations are found by numerically solving,

$$\omega_t^2(k) = k^2 + \Pi_t(\omega_t(k), k) \quad \omega_\ell^2(k) = \frac{\omega_\ell^2(k)}{k^2}\Pi_\ell(\omega_\ell(k), k) \tag{C.41}$$

Where,

$$\begin{aligned}
\Pi_t(\omega, k) &= \omega_p^2 \frac{3}{2v_*^2}\left(\frac{\omega^2}{k^2} - \frac{\omega^2 - v_*^2 k^2}{k^2}\frac{\omega}{2v_* k}\ln\left(\frac{\omega + v_* k}{\omega - v_* k}\right)\right), \\
\Pi_\ell(\omega, k) &= \frac{3\omega_p^2}{v_*^2}\left(\frac{\omega}{2v_* k}\ln\left(\frac{\omega + v_* k}{\omega - v_* k}\right) - 1\right).
\end{aligned}$$

These analytic equations for the dispersion relations are derived by assuming that the velocity of the particles in the plasma are dominated by single velocity, v_* given by ${v_*}^2 = \omega_1^2/\omega_p^2$, where

$$\omega_p^2 = \frac{4\alpha}{\pi}\int_0^\infty dp \frac{p^2}{E}\left(1 - \frac{v^2}{3}\right)\left(n_{e^-}(E) + \overline{n}_{e^+}(E)\right) \tag{C.42}$$

$$\omega_1^2 = \frac{4\alpha}{\pi}\int_0^\infty dp \frac{p^2}{E}\left(\frac{5}{3}v^2 - v^4\right)\left(n_{e^-}(E) + \overline{n}_{e^+}(E)\right). \tag{C.43}$$

This also defines the plasma frequency ω_p. Finally, the field renormalizations for the plasmon are given by

$$Z_t = \frac{2\omega_t^2(\omega_t^2 - v_*^2 k^2)}{3\omega_p^2\omega_t^2 + (\omega_t^2 + k^2)(\omega_t^2 - v_*^2 k^2) - 2\omega_t^2(\omega_t^2 - k^2)} \tag{C.44}$$

$$Z_\ell = \frac{2(\omega_\ell^2 - v_*^2 k^2)}{3\omega_p^2 - (\omega_\ell^2 - v_*^2 k^2)}. \tag{C.45}$$

Using all of this, our longitudinal and transverse matrix elements are

$$\int d\Pi_2(p_1, p_2)|\mathcal{M}|_L^2 = \frac{Z_\ell \omega_\ell^2}{k^2}\left(\frac{k^4\beta^3(k^2, m_a, m_D)}{48\pi f_a^2}\right) \tag{C.46}$$

$$\int d\Pi_2(p_1,p_2)|\mathcal{M}|^2_T = Z_t\left(\frac{k^4\beta^3(k^2,m_a,m_D)}{48\pi f_a^2}\right) \tag{C.47}$$

Then for each polarization

$$\omega_{\ell,t}\Gamma_{L,T} = \frac{1}{2}\int d\Pi_2(p_1,p_2)|\mathcal{M}|^2_{L,T}. \tag{C.48}$$

If we define

$$\hat{\pi}_{\ell,t} \equiv \frac{\omega^2_{\ell,t} - |\boldsymbol{k}|^2}{\omega_p^2}, \tag{C.49}$$

We can write the emissivity using Eq. 4.4

$$\epsilon_a = \frac{\zeta_3 T^3}{3\pi f_a^2}\left(\frac{\omega_P^2}{4\pi}\right)^2 Q^P \tag{C.50}$$

With $Q^P = Q^P_L + Q^P_T$ where,

$$Q^P_L = \frac{1}{4\zeta_3 T^3}\int_0^{k_1} d|\boldsymbol{k}|\frac{|\boldsymbol{k}|^2}{e^{\omega_\ell/T}-1}\frac{\omega_\ell^2}{\omega_p^2}Z_L\hat{\pi}_\ell\beta^3(\omega_p^2\hat{\pi}_t, m_a, m_D) \tag{C.51}$$

$$Q^P_T = \frac{1}{2\zeta_3 T^3}\int_0^{\infty} d|\boldsymbol{k}|\frac{|\boldsymbol{k}|^2}{e^{\omega_t/T}-1}Z_T\hat{\pi}_t^2\beta^3(\omega_p^2\hat{\pi}_t, m_a, m_D). \tag{C.52}$$

C.1.2 Scattering Cross Section

The matrix elements for each process are shown in Fig. 4.4 and their amplitudes are simple to write, using notation developed in the previous sections.

$$i\mathcal{M}_{\psi\gamma_D\to\psi\phi} = \frac{iQ_\psi}{q^2}\bar{u}(p')\gamma_\mu u(p)\mathcal{A}^\mu(q,k') \tag{C.53}$$

$$i\mathcal{M}_{\psi\phi\to\psi\gamma_D} = \frac{-iQ_\psi}{q^2}\bar{u}(p')\gamma_\mu u(p)\mathcal{A}^{*\mu}(q,k') \tag{C.54}$$

Q_ψ is the electric charge of the fermion, ψ. We can easily square this matrix element, sum over final spins and average over initial state spins:

$$\overline{|\mathcal{M}|^2} = \frac{2e^2}{g_{\star,k}t^2}\left(2p_\mu p_\nu + \frac{t}{2}\eta_{\mu\nu}\right)\sum_{\gamma_D\ spins}\mathcal{A}^{\mu}(q,k')\mathcal{A}^{*\nu}(q,k') \tag{C.55}$$

$g_{\star,k}$ represents the degrees of freedom in the initial particle that is either the axion or dark photon and t is the Mandelstam variable equal to the square of the transferred momentum. We will also use k to denote the initial particle four momentum and k' to denote the final particles four momentum regardless of if that particle is an axion or dark photon. Framing the computation this way allows us to compute both matrix elements at once. As discussed in Sec. 4.2, we are interested in computing the momentum transfer cross section defined in Eq. 4.13. For computational ease we consider a relativistically invariant generalization of the momentum transfer cross section by replacing the $1-\cos(\theta)$ with $2t/(sA)$. Where

$$t = (k-k')^2 = \frac{s}{2}(A + B\cos(\theta)) \tag{C.56}$$

and

$$A = 2\frac{k^2+k'^2}{s} - \alpha(s,\sqrt{k^2},m_\psi)\alpha(s,\sqrt{k'^2},m_\psi) \quad B = \beta(s,\sqrt{k^2},m_\psi)\beta(s,\sqrt{k'^2},m_\psi). \tag{C.57}$$

It is easy to see that in the limit $m_\psi/s \ll 1$ (valid for electrons and positrons which are relativistic in the supernova) and the limit $m_\psi^2 \gg k^2, k'^2$ (valid for protons)

$$B \to -A \implies t \to \frac{sA}{2}(1-\cos(\theta)) \implies 2t/(sA) \to 1-\cos(\theta). \tag{C.58}$$

This property allows us to compute the momentum transfer cross section without sacrificing relativistic invariance.

$$\sigma_{\Delta \boldsymbol{p}} \approx \frac{1}{4E_A E_B \Delta \boldsymbol{v}} \int d\Pi_f |\mathcal{M}|^2 \left(\frac{2t}{sA}\right) \tag{C.59}$$

We have checked that the final results are insensitive to this particular deviation from standard convention.

In order to compute the cross section will need to compute the final state integral

$$R_1 = \int d\Pi_2(k', p') t |\mathcal{M}|^2 \tag{C.60}$$

This integral can be computed by expanding in terms of Lorentz covariant tensors involving the initial state momenta and metric. We can then compute the necessary coefficients in this expansion by picking specific components for the indices in the center of mass frame or contracting. When all is done, the result is,

$$R_1 = -\frac{2e^2}{g_{\star,k} f_a^2} \frac{s\beta'}{32\pi} \left(k^2 \beta'^2 + k'^2 \beta^2 + \frac{s\beta^2\beta'^2}{3} + s\beta\beta' \left(\frac{1}{V} - \frac{1-V^2}{V^2} \text{arctanh}(V) \right) \right) \tag{C.61}$$

Where

$$V = -B/A \quad \beta = \beta(s, \sqrt{k^2}, m_\psi) \quad \beta' = \beta(s, \sqrt{k'^2}, m_\psi). \tag{C.62}$$

Finally, plugging this into the cross section, we find

$$\sigma_{\Delta \boldsymbol{p}} = \frac{\alpha_e}{3 g_{\star,k} f^2} \frac{s\beta'}{2E_A E_B |\boldsymbol{v}_A - \boldsymbol{v}_B|} I(s, m_\psi^2, k^2, k'^2) \tag{C.63}$$

Where

$$I(s, m_\psi^2, k^2, k'^2) = \frac{3}{4}\left(V\left(\frac{k^2\beta'}{s\beta} + \frac{k'^2\beta}{s\beta'} + \frac{\beta\beta'}{3}\right) + \left(1 - (1-V^2)\frac{\text{arctanh}(V)}{V}\right)\right). \tag{C.64}$$

Inserting m_a and m_D into the appropriate spots for each cross section gives us Eq 4.14.

C.1.3 Longitudinal Scattering Cross Section

In order to compute the longitudinal bounds, we need to compute the cross section for $\gamma_D^L + e^- \to \phi + e^-$. The method described above transfers nicely to this specific case. Starting with Eq. C.55, we replace the sum over dark photon polarizations with just the longitudinal polarizations. Since the dark photon is in the initial state here, these polarization don't interfere with the final state integrals which are expanded and computed just as before. The only remaining difference is the contraction with the epsilon tensors which now must be contracted with the explicit longitudinal polarization rather than the metric. After some simplification, the result is

$$\sigma_{\Delta \boldsymbol{p}}^{\gamma_D^L \to \phi} = \frac{\alpha_e}{3 f_a^2}\left(\frac{m_D^2}{s}\right) \frac{s\beta'}{2E_A E_B |\boldsymbol{v}_A - \boldsymbol{v}_B|} \left(\frac{2|\boldsymbol{p}|^2 \sin^2(\theta)}{s\beta^2}\left(I(s, m_\psi^2, m_D^2, m_a^2) - \frac{V\beta'}{3\beta}\right) + \frac{V\beta'}{3\beta}\right). \tag{C.65}$$

C.1.4 Decay Widths

Let us now compute Eq. 4.16 From the diagram given in Fig. 4.4 it is easy to see that the amplitude for scattering can be written as

$$i\mathcal{M} = i\epsilon_\gamma^\mu \mathcal{A}_\mu(p_1, p_2). \tag{C.66}$$

Here, p_1 will be the photon momentum and p_2 will be the other final state particle, axion, or dark photon. Squaring this, summing over final spins, averaging over initial spins, and integrating over final states is straightforward.

$$\int d\Pi_f \sum \overline{|\mathcal{M}_{\phi\to D}|^2} = \frac{m_a^4}{16\pi f_a^2}\left(1 - \frac{m_D^2}{m_a^2}\right)^3 \tag{C.67}$$

$$\int d\Pi_f \sum \overline{|\mathcal{M}_{D\to\phi}|^2} = \frac{m_D^4}{16\pi f_a^2}\left(1 - \frac{m_a^2}{m_D^2}\right)^3. \tag{C.68}$$

To find the decay width we simply divide by $2E$ where E is the initial energy and we recover Eq. 4.16.

$$\Gamma_a = \frac{m_a^4}{32\pi f_a^2 E}\left(1 - \frac{m_D^2}{m_a^2}\right)^3 \qquad \Gamma_D = \frac{m_D^4}{96\pi f_a^2 E}\left(1 - \frac{m_a^2}{m_D^2}\right)^3 \tag{C.69}$$

C.1.5 Production of Longitudinal Dark Photons

The emissivity for a given process of longitudinal dark photons is given by Eq. 4.28. Just as before, we separate the matrix element as

$$i\mathcal{M}_L = \mathcal{M}_\mu^X \mathcal{A}_L^\mu \quad \text{where} \quad \mathcal{A}_L^\mu = \frac{\epsilon^{\mu\nu\alpha\beta}}{f_a} k_\nu p_{2\alpha} \epsilon^D_{L\,\beta}. \tag{C.70}$$

For the two processes we are considering here, the final state is only the axion and dark photon so we can write

$$\dot{\epsilon}_L^D = \left(\prod_i n_i\right) \left\langle \mathcal{M}_\mu^X \mathcal{M}_\nu^X \int d\Pi_2(p_1, p_2) \mathcal{A}_L^\mu \mathcal{A}_L^\nu p_2^0 \right\rangle \tag{C.71}$$

Where $\prod_i n_i$ is the product of the densities of the initial state(s). The final state integral can be computed by considering the Lorentz covariant tensor

$$L^{\mu\nu\alpha} \equiv \int d\Pi_2(p_1, p_2) \mathcal{A}_L^\mu \mathcal{A}_L^\nu p_2^\alpha \tag{C.72}$$

of which we wish to take the $\alpha = 0$ component. This integral can be computed by contracting the μ and ν indices, computing in the supernova frame where the longitudinal polarization takes the simple form $\epsilon_L = \frac{1}{m_D}\left(|\boldsymbol{k}|, \hat{\boldsymbol{k}} k^0\right)$, and then properly relating the supernova frame momenta to the center of mass frame momenta so that we may do the final state integral in the center of mass frame. The result is that,

$$L^{\mu\nu\alpha} = L\left(\frac{k^\mu k^\nu}{k^2} - \eta^{\mu\nu}\right) k^\alpha \tag{C.73}$$

Where,

$$L = \frac{\beta_D^3 k^4}{48\pi f_a^2} k^0 \frac{v^2 m_D^2}{k^2} \left(\alpha_D I_0 + v \beta_D I_1\right) \tag{C.74}$$

And

$$I_n \equiv \int_{-1}^{1} \frac{x^n dx}{\frac{(\beta_D + v\alpha_D x)^2}{1-x^2} + \frac{4v^2 m_D^2}{k^2}} \quad \beta_D = \beta(k^2, m_D, m_a) \tag{C.75}$$

$$\alpha_D = \alpha(k^2, m_D, m_a) \quad v = \frac{|\boldsymbol{k}|}{k^0}. \tag{C.76}$$

The rest of the computations follow just as before. The end result is,

$$\dot{\epsilon}_a^L = \frac{m_D^2}{\langle s\rangle}\frac{\alpha_e}{24f^2} n_{e^-} n_{e^+} \langle E_{tot}\rangle \, Q_L^a(m_a, m_D) \quad \dot{\epsilon}_p^L = \frac{\zeta(3) T^3}{3\pi f_a^2}\left(\frac{\omega_p^2}{4\pi}\right)^2 \left(\frac{m_D^2}{\omega_p^2}\right) Q_L^P(m_a, m_D) \tag{C.77}$$

Where,

$$Q_L^a(m_a, m_D) = \left\langle \frac{\langle s\rangle \, v^2}{s}\left(\alpha_D I_0 + v\beta_D I_1\right)\frac{(E_A + E_B)}{\langle E_A + E_B\rangle}\frac{s + 2m_e^2}{2E_A E_B}\beta^3(s, m_a, m_D)\right\rangle \tag{C.78}$$

$$Q_L^P(m_a, m_D) = Q_{L,T}^p(m_a, m_D) + Q_{L,L}^p(m_a, m_D) \tag{C.79}$$

$$Q_{L,L}^P \equiv \frac{1}{4\zeta_3 T^3}\int_0^{k_1} d|\boldsymbol{k}| \frac{|\boldsymbol{k}|^2}{e^{\omega_\ell/T} - 1}\frac{\omega_\ell^2}{\omega_p^2}\frac{Z_L}{\hat{\pi}_\ell}\frac{|\boldsymbol{k}|^2}{\omega_\ell^2}\beta^3(\omega_p^2\hat{\pi}_t, m_a, m_D)\left(\alpha_D I_0 + v\beta_D I_1\right) \tag{C.80}$$

$$Q_{L,T}^P \equiv \frac{1}{2\zeta_3 T^3}\int_0^{\infty} d|\boldsymbol{k}| \frac{|\boldsymbol{k}|^2}{e^{\omega_t/T} - 1}\frac{|\boldsymbol{k}|^2}{\omega_t^2} Z_T \beta^3(\omega_p^2\hat{\pi}_t, m_a, m_D)\left(\alpha_D I_0 + v\beta_D I_1\right). \tag{C.81}$$

C.2 Supernova Profiles

In this section we discuss the profile used in placing our constraints and the variation in the constraints placed that arise when using a different profile. The temperature (T), mass density (ρ), and electron fraction (Y_e) profiles used in our computations use analytical fits to simulation used in Ref. [93]. These profiles are shown in Fig. C.1.

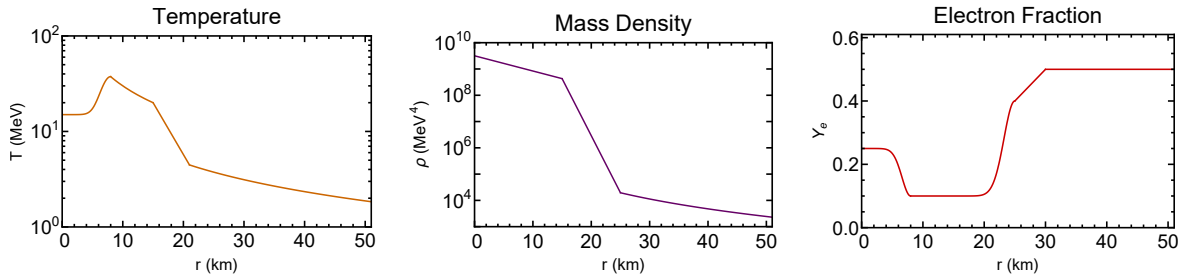

Figure C.1: The temperature, mass density, and electron fraction as a function of radius of the supernova.

Our expressions for the emissivities and scattering cross sections involve number densities and chemical potentials. From these profiles we can calculate the number densities for the electron, proton, neutron, photon and positron. From the number densities, we can compute the chemical potentials of the electron, proton and neutron (μ_e, μ_p and μ_n respectively).

In order to access the dependence of our results on the profile used, we redid our calculations using the $18\,M_\odot$ profile found in Ref. [104]. To compare the results visually, we show the total luminosity as a function of axion mass for the two different profiles in Fig. C.2. In both profiles, annihilation is the dominant source of cooling. The difference between the bulk cooling bound placed on f_a when using the two different profiles is about a factor of 1.5, which is within the expected uncertainty of cooling bounds from supernovae.

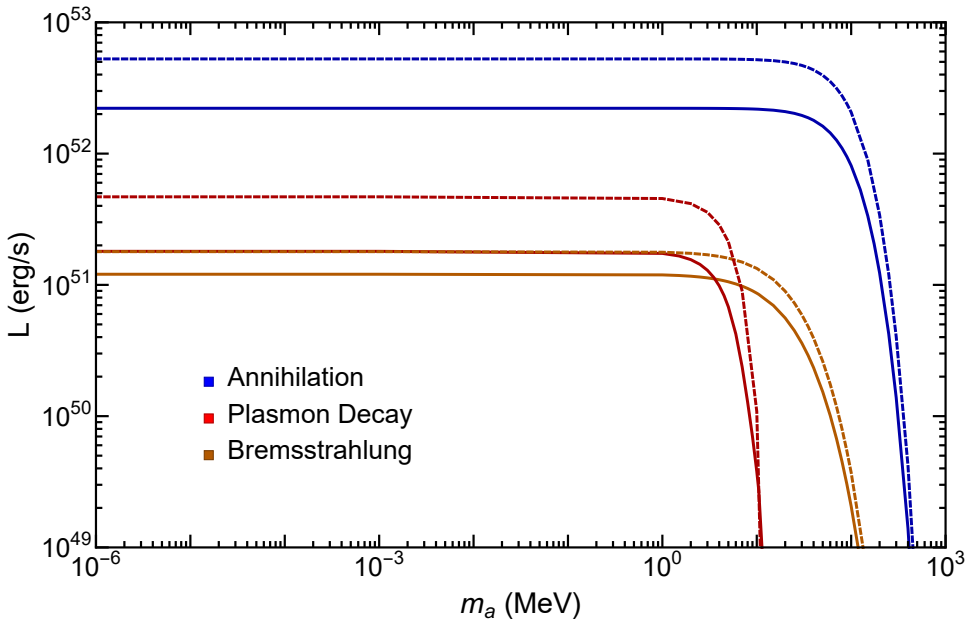

Figure C.2: The total luminosity of various channels as a function of axion mass. The solid lines show the profile in Ref. [93] while the dashed lines show the profile in Ref. [104]. The difference in the bounds on f_a is about a factor of 1.5.

Bibliography

[1] Paul Adrien Maurice Dirac. Quantised singularities in the electromagnetic field,. *Proc. Roy. Soc. Lond. A*, 133(821):60–72, 1931.

[2] Gerard 't Hooft. Magnetic Monopoles in Unified Gauge Theories. *Nucl. Phys. B*, 79:276–284, 1974.

[3] Alexander M. Polyakov. Particle Spectrum in Quantum Field Theory. *JETP Lett.*, 20:194–195, 1974.

[4] Edward Witten. Dyons of Charge e theta/2 pi. *Phys. Lett. B*, 86:283–287, 1979.

[5] Curtis G. Callan, Jr. Disappearing Dyons. *Phys. Rev. D*, 25:2141, 1982.

[6] John Preskill. MAGNETIC MONOPOLES. *Ann. Rev. Nucl. Part. Sci.*, 34:461–530, 1984.

[7] Curtis G. Callan, Jr. Monopole Catalysis of Baryon Decay. *Nucl. Phys. B*, 212:391–400, 1983.

[8] Curtis G. Callan, Jr. Dyon-Fermion Dynamics. *Phys. Rev. D*, 26:2058–2068, 1982.

[9] V. A. Rubakov. Superheavy Magnetic Monopoles and Proton Decay. *JETP Lett.*, 33:644–646, 1981.

[10] V. a. Rubakov and M. s. Serebryakov. ANOMALOUS BARYON NUMBER NONCONSERVATION IN THE PRESENCE OF SU(5) MONOPOLES. *Nucl. Phys. B*, 218:240–268, 1983.

[11] T. Daniel Brennan. Callan-Rubakov effect and higher charge monopoles. *JHEP*, 02:159, 2023.

[12] T. Daniel Brennan. A New Solution to the Callan Rubakov Effect. 9 2023.

[13] Kunio Kaneta, Hye-Sung Lee, and Seokhoon Yun. Portal Connecting Dark Photons and Axions. *Phys. Rev. Lett.*, 118(10):101802, 2017.

[14] Kunio Kaneta, Hye-Sung Lee, and Seokhoon Yun. Dark photon relic dark matter production through the dark axion portal. *Phys. Rev. D*, 95(11):115032, 2017.

[15] Maxim Pospelov, Josef Pradler, Joshua T. Ruderman, and Alfredo Urbano. Room for New Physics in the Rayleigh-Jeans Tail of the Cosmic Microwave Background. *Phys. Rev. Lett.*, 121(3):031103, 2018.

[16] Kiwoon Choi, Sangjun Lee, Hyeonseok Seong, and Seokhoon Yun. Gamma-ray spectral modulations induced by photon-ALP-dark photon oscillations. *Phys. Rev. D*, 101(4):043007, 2020.

[17] Oleg E. Kalashev, Alexander Kusenko, and Edoardo Vitagliano. Cosmic infrared background excess from axionlike particles and implications for multimessenger observations of blazars. *Phys. Rev. D*, 99(2):023002, 2019.

[18] Sanjoy Biswas, Anirban Chatterjee, Emidio Gabrielli, and Barbara Mele. Probing dark-axionlike particle portals at future e^+e^- colliders. *Phys. Rev. D*, 100(11):115040, 2019.

[19] Kiwoon Choi, Hyeonseok Seong, and Seokhoon Yun. Axion-photon-dark photon oscillation and its implication for 21 cm observation. *Phys. Rev. D*, 102(7):075024, 2020.

[20] Anson Hook, Gustavo Marques-Tavares, and Yuhsin Tsai. Scalars Gliding through an Expanding Universe. *Phys. Rev. Lett.*, 124(21):211801, 2020.

[21] Patrick deNiverville, Hye-Sung Lee, and Young-Min Lee. New searches at the reactor experiments based on the dark axion portal. 11 2020.

[22] Paola Arias, Ariel Arza, Joerg Jaeckel, and Diego Vargas-Arancibia. Hidden Photon Dark Matter Interacting via Axion-like Particles. 7 2020.

[23] Anson Hook, Gustavo Marques-Tavares, and Clayton Ristow. Supernova constraints on an axion-photon-dark photon interaction. *JHEP*, 06:167, 2021.

[24] Pierluca Carenza, Giuseppe Lucente, and Edoardo Vitagliano. Probing the blue axion with cosmic optical background anisotropies. *Phys. Rev. D*, 107(8):083032, 2023.

[25] Peter W. Graham, Jeremy Mardon, and Surjeet Rajendran. Vector Dark Matter from Inflationary Fluctuations. *Phys. Rev. D*, 93(10):103520, 2016.

[26] Prateek Agrawal, Naoya Kitajima, Matthew Reece, Toyokazu Sekiguchi, and Fuminobu Takahashi. Relic Abundance of Dark Photon Dark Matter. *Phys. Lett. B*, 801:135136, 2020.

[27] Mar Bastero-Gil, Jose Santiago, Lorenzo Ubaldi, and Roberto Vega-Morales. Vector dark matter production at the end of inflation. *JCAP*, 04:015, 2019.

[28] Raymond T. Co, Aaron Pierce, Zhengkang Zhang, and Yue Zhao. Dark Photon Dark Matter Produced by Axion Oscillations. *Phys. Rev. D*, 99(7):075002, 2019.

[29] Jeff A. Dror, Keisuke Harigaya, and Vijay Narayan. Parametric Resonance Production of Ultralight Vector Dark Matter. *Phys. Rev. D*, 99(3):035036, 2019.

[30] Andrew J. Long and Lian-Tao Wang. Dark Photon Dark Matter from a Network of Cosmic Strings. *Phys. Rev. D*, 99(6):063529, 2019.

[31] Edward Broadberry, Saurav Das, Anson Hook, and Gustavo Marques-Tavares. in preparation.

[32] Peter Svrcek and Edward Witten. Axions In String Theory. *JHEP*, 06:051, 2006.

[33] Asimina Arvanitaki, Savas Dimopoulos, Sergei Dubovsky, Nemanja Kaloper, and John March-Russell. String Axiverse. *Phys. Rev. D*, 81:123530, 2010.

[34] Mark Goodsell, Joerg Jaeckel, Javier Redondo, and Andreas Ringwald. Naturally Light Hidden Photons in LARGE Volume String Compactifications. *JHEP*, 11:027, 2009.

[35] Mehmet Demirtas, Naomi Gendler, Cody Long, Liam McAllister, and Jakob Moritz. PQ Axiverse. 12 2021.

[36] Th. Kaluza. Zum Unitätsproblem der Physik. *Sitzungsber. Preuss. Akad. Wiss. Berlin (Math. Phys.)*, 1921:966–972, 1921.

[37] Oskar Klein. Quantum Theory and Five-Dimensional Theory of Relativity. (In German and English). *Z. Phys.*, 37:895–906, 1926.

[38] L. F. Abbott and P. Sikivie. A Cosmological Bound on the Invisible Axion. *Phys. Lett. B*, 120:133–136, 1983.

[39] Michael Dine and Willy Fischler. The Not So Harmless Axion. *Phys. Lett. B*, 120:137–141, 1983.

[40] John Preskill, Mark B. Wise, and Frank Wilczek. Cosmology of the Invisible Axion. *Phys. Lett. B*, 120:127–132, 1983.

[41] Ann E. Nelson and Jakub Scholtz. Dark Light, Dark Matter and the Misalignment Mechanism. *Phys. Rev. D*, 84:103501, 2011.

[42] Paola Arias, Davide Cadamuro, Mark Goodsell, Joerg Jaeckel, Javier Redondo, and Andreas Ringwald. WISPy Cold Dark Matter. *JCAP*, 06:013, 2012.

[43] Marco Battaglieri et al. US Cosmic Visions: New Ideas in Dark Matter 2017: Community Report. In *U.S. Cosmic Visions: New Ideas in Dark Matter*, 7 2017.

[44] R. D. Peccei and Helen R. Quinn. Some Aspects of Instantons. *Nuovo Cim. A*, 41:309, 1977.

[45] R. D. Peccei and Helen R. Quinn. CP Conservation in the Presence of Instantons. *Phys. Rev. Lett.*, 38:1440–1443, 1977.

[46] Steven Weinberg. A New Light Boson? *Phys. Rev. Lett.*, 40:223–226, 1978.

[47] Frank Wilczek. Problem of Strong P and T Invariance in the Presence of Instantons. *Phys. Rev. Lett.*, 40:279–282, 1978.

[48] John C. Mather et al. Measurement of the Cosmic Microwave Background spectrum by the COBE FIRAS instrument. *Astrophys. J.*, 420:439–444, 1994.

[49] D. J. Fixsen, E. S. Cheng, J. M. Gales, John C. Mather, R. A. Shafer, and E. L. Wright. The Cosmic Microwave Background spectrum from the full COBE FIRAS data set. *Astrophys. J.*, 473:576, 1996.

[50] Andrea Caputo, Hongwan Liu, Siddharth Mishra-Sharma, and Joshua T. Ruderman. Dark Photon Oscillations in Our Inhomogeneous Universe. *Phys. Rev. Lett.*, 125(22):221303, 2020.

[51] Tracy R. Slatyer and Chih-Liang Wu. Early-Universe constraints on dark matter-baryon scattering and their implications for a global 21 cm signal. *Phys. Rev. D*, 98(2):023013, 2018.

[52] Jesus Zavala, Mark Vogelsberger, and Simon D. M. White. Relic density and CMB constraints on dark matter annihilation with Sommerfeld enhancement. *Phys. Rev. D*, 81:083502, 2010.

[53] Yacine Ali-Haïmoud. Testing dark matter interactions with CMB spectral distortions. *Phys. Rev. D*, 103(4):043541, 2021.

[54] Ki-Young Choi, Kenji Kadota, and Inwoo Park. Constraining dark photon model with dark matter from CMB spectral distortions. *Phys. Lett. B*, 771:162–167, 2017.

[55] Kerstin E. Kunze and Miguel Á. Vázquez-Mozo. Constraints on hidden photons from current and future observations of CMB spectral distortions. *JCAP*, 12:028, 2015.

[56] Asher Berlin, Jeff A. Dror, Xucheng Gan, and Joshua T. Ruderman. Millicharged Relics Reveal Massless Dark Photons. 11 2022.

[57] Dalila Pîrvu, Junwu Huang, and Matthew C. Johnson. Patchy Screening of the CMB from Dark Photons. 7 2023.

[58] K. Hirata et al. Observation of a Neutrino Burst from the Supernova SN 1987a. *Phys. Rev. Lett.*, 58:1490–1493, 1987.

[59] R. M. Bionta et al. Observation of a Neutrino Burst in Coincidence with Supernova SN 1987a in the Large Magellanic Cloud. *Phys. Rev. Lett.*, 58:1494, 1987.

[60] E. N. Alekseev, L. N. Alekseeva, V. I. Volchenko, and I. V. Krivosheina. Possible Detection of a Neutrino Signal on 23 February 1987 at the Baksan Underground Scintillation Telescope of the Institute of Nuclear Research. *JETP Lett.*, 45:589–592, 1987.

[61] Adam Burrows and James M. Lattimer. The birth of neutron stars. *Astrophys. J.*, 307:178–196, 1986.

[62] Adam Burrows and James M. Lattimer. Neutrinos from SN 1987A. *Astrophys. J. Lett.*, 318:L63–L68, 1987.

[63] G. G. Raffelt. *Stars as laboratories for fundamental physics: The astrophysics of neutrinos, axions, and other weakly interacting particles*. 5 1996.

[64] Michael S. Turner. Axions from SN 1987a. *Phys. Rev. Lett.*, 60:1797, 1988.

[65] Georg Raffelt and David Seckel. Bounds on Exotic Particle Interactions from SN 1987a. *Phys. Rev. Lett.*, 60:1793, 1988.

[66] Georg G. Raffelt. SUPERNOVA SN1987A AND SOME PROPERTIES OF LIGHT, EXOTIC PARTICLES. In *24th International Conference on High-energy Physics*, 8 1988.

[67] Giuseppe Lucente, Pierluca Carenza, Tobias Fischer, Maurizio Giannotti, and Alessandro Mirizzi. Heavy axion-like particles and core-collapse supernovae: constraints and impact on the explosion mechanism. *JCAP*, 12:008, 2020.

[68] N. Ishizuka and M. Yoshimura. Axion and Dilaton Emissivity From Nascent Neutron Stars. *Prog. Theor. Phys.*, 84:233–250, 1990.

[69] James D. Bjorken, Rouven Essig, Philip Schuster, and Natalia Toro. New Fixed-Target Experiments to Search for Dark Gauge Forces. *Phys. Rev. D*, 80:075018, 2009.

[70] James B. Dent, Francesc Ferrer, and Lawrence M. Krauss. Constraints on Light Hidden Sector Gauge Bosons from Supernova Cooling. 1 2012.

[71] Ermal Rrapaj and Sanjay Reddy. Nucleon-nucleon bremsstrahlung of dark gauge bosons and revised supernova constraints. *Phys. Rev. C*, 94(4):045805, 2016.

[72] Herbert K. Dreiner, Jean-François Fortin, Christoph Hanhart, and Lorenzo Ubaldi. Supernova constraints on MeV dark sectors from e^+e^- annihilations. *Phys. Rev. D*, 89(10):105015, 2014.

[73] Jae Hyeok Chang, Rouven Essig, and Samuel D. McDermott. Supernova 1987A Constraints on Sub-GeV Dark Sectors, Millicharged Particles, the QCD Axion, and an Axion-like Particle. *JHEP*, 09:051, 2018.

[74] Jorge Martin Camalich, Jorge Terol-Calvo, Laura Tolos, and Robert Ziegler. Supernova Constraints on Dark Flavored Sectors. 12 2020.

[75] K. Kainulainen, J. Maalampi, and J. T. Peltoniemi. Inert neutrinos in supernovae. *Nucl. Phys. B*, 358:435–446, 1991.

[76] Christoph Hanhart, Daniel R. Phillips, Sanjay Reddy, and Martin J. Savage. Extra dimensions, SN1987a, and nucleon-nucleon scattering data. *Nucl. Phys. B*, 595:335–359, 2001.

[77] Christoph Hanhart, Jose A. Pons, Daniel R. Phillips, and Sanjay Reddy. The Likelihood of GODs' existence: Improving the SN1987a constraint on the size of large compact dimensions. *Phys. Lett. B*, 509:1–9, 2001.

[78] Jae Hyeok Chang, Rouven Essig, and Samuel D. McDermott. Revisiting Supernova 1987A Constraints on Dark Photons. *JHEP*, 01:107, 2017.

[79] Edward Hardy and Robert Lasenby. Stellar cooling bounds on new light particles: plasma mixing effects. *JHEP*, 02:033, 2017.

[80] Edward Witten. An SU(2) Anomaly. *Phys. Lett. B*, 117:324–328, 1982.

[81] Sidney R. Coleman. The Quantum Sine-Gordon Equation as the Massive Thirring Model. *Phys. Rev. D*, 11:2088, 1975.

[82] S. Mandelstam. Soliton Operators for the Quantized Sine-Gordon Equation. *Phys. Rev. D*, 11:3026, 1975.

[83] Curtis g. Callan, Jr. THE MONOPOLE CATALYSIS S MATRIX. In *Workshop on Problems in Unification and Supergravity*, pages 45–53, 1983.

[84] S. Dawson and A. N. Schellekens. Monopole - Fermion Interactions: The Soliton Picture. *Phys. Rev. D*, 28:3125, 1983.

[85] Jens Chluba. Green's function of the cosmological thermalization problem – II. Effect of photon injection and constraints. *Mon. Not. Roy. Astron. Soc.*, 454(4):4182–4196, 2015.

[86] Ya. B. Zeldovich and R. A. Sunyaev. The Interaction of Matter and Radiation in a Hot-Model Universe. *Astrophys. Space Sci.*, 4:301–316, 1969.

[87] Jens Chluba. Green's function of the cosmological thermalization problem. *Mon. Not. Roy. Astron. Soc.*, 434:352, 2013.

[88] Eric Braaten and Daniel Segel. Neutrino energy loss from the plasma process at all temperatures and densities. *Phys. Rev. D*, 48:1478–1491, 1993.

[89] Matteo Lucca, Nils Schöneberg, Deanna C. Hooper, Julien Lesgourgues, and Jens Chluba. The synergy between CMB spectral distortions and anisotropies. *JCAP*, 02:026, 2020.

[90] Francesco Capozzi and Georg Raffelt. Axion and neutrino bounds improved with new calibrations of the tip of the red-giant branch using geometric distance determinations. *Phys. Rev. D*, 102:083007, Oct 2020.

[91] A Kogut, D.J Fixsen, D.T Chuss, J Dotson, E Dwek, M Halpern, G.F Hinshaw, S.M Meyer, S.H Moseley, M.D Seiffert, D.N Spergel, and E.J Wollack. The primordial inflation explorer (PIXIE): a nulling polarimeter for cosmic microwave background observations. *Journal of Cosmology and Astroparticle Physics*, 2011(07):025–025, jul 2011.

[92] Georg G. Raffelt. Muon-neutrino and tau-neutrino spectra formation in supernovae. *Astrophys. J.*, 561:890–914, 2001.

[93] William DeRocco, Peter W. Graham, Daniel Kasen, Gustavo Marques-Tavares, and Surjeet Rajendran. Supernova signals of light dark matter. *Phys. Rev. D*, 100(7):075018, 2019.

[94] Herbert K. Dreiner, Jean-François Fortin, Jordi Isern, and Lorenzo Ubaldi. White Dwarfs constrain Dark Forces. *Phys. Rev. D*, 88:043517, 2013.

[95] Patrick deNiverville, Hye-Sung Lee, and Min-Seok Seo. Implications of the dark axion portal for the muon g-2, B-factories, fixed target neutrino experiments and beam dumps. *Phys. Rev. D*, 98(11):115011, 2018.

[96] Francesco Capozzi and Georg Raffelt. Axion and neutrino bounds improved with new calibrations of the tip of the red-giant branch using geometric distance determinations. *Phys. Rev. D*, 102(8):083007, 2020.

[97] Joseph Polchinski. Monopoles, duality, and string theory. *Int. J. Mod. Phys. A*, 19S1:145–156, 2004.

[98] Michael A. Fedderke, Peter W. Graham, and Surjeet Rajendran. Axion Dark Matter Detection with CMB Polarization. *Phys. Rev. D*, 100(1):015040, 2019.

[99] Kim Griest and David Seckel. Three exceptions in the calculation of relic abundances. *Phys. Rev. D*, 43:3191–3203, 1991.

[100] Raffaele Tito D'Agnolo, Duccio Pappadopulo, and Joshua T. Ruderman. Fourth Exception in the Calculation of Relic Abundances. *Phys. Rev. Lett.*, 119(6):061102, 2017.

[101] Hirotaka Sugawara. A field theory of currents. *Phys. Rev.*, 170:1659–1662, Jun 1968.

[102] Charles M. Sommerfield. Currents as dynamical variables. *Phys. Rev.*, 176:2019–2025, Dec 1968.

[103] C. G. Callan, R. F. Dashen, and D. H. Sharp. Solvable two-dimensional field theory based on currents. *Phys. Rev.*, 165:1883–1886, Jan 1968.

[104] Tobias Fischer, Sovan Chakraborty, Maurizio Giannotti, Alessandro Mirizzi, Alexandre Payez, and Andreas Ringwald. Probing axions with the neutrino signal from the next galactic supernova. *Phys. Rev. D*, 94(8):085012, 2016.